JSC-12976

SVDS PLUME IMPINGEMENT MODELING DEVELOPMENT

Sensitivity Analysis Supporting Level B Requirements

Mission Planning and Analysis Division

July 1977

AUG 1977
RECEIVED
NASA STI FACILITY
INPUT BRANCH

NASA

National Aeronautics and
Space Administration

Lyndon B. Johnson Space Center
Houston, Texas

SHUTTLE PROGRAM

SVDS PLUME IMPINGEMENT MODELING DEVELOPMENT

SENSITIVITY ANALYSIS SUPPORTING LEVEL B REQUIREMENTS

By P. B. Chiu, D. J. Pearson, P. M. Muhm, and P. B. Schoonmaker,
McDonnell Douglas Technical Services Co., Houston, Tx.; and
R. J. Radar, MDAC, Huntington Beach, Calif.

JSC Technical Monitor: J. A. Bell
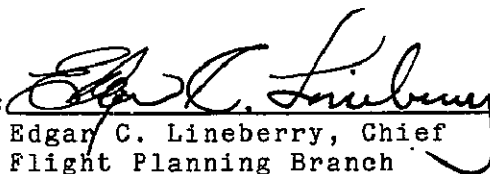
Approved:_____
          Edgar C. Lineberry, Chief
          Flight Planning Branch
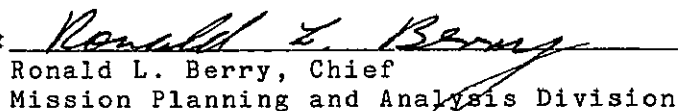
Approved:_____
          Ronald L. Berry, Chief
          Mission Planning and Analysis Division

National Aeronautics and Space Administration

Lyndon B. Johnson Space Center

Mission Planning and Analysis Division

Houston, Texas

July 1977

CONTENTS

TABLES

FIGURES

SVDS PLUME IMPINGEMENT MODELING DEVELOPMENT

SENSITIVITY ANALYSIS SUPPORTING LEVEL B REQUIREMENTS

By P. B. Chiu, D. J. Pearson, P. M. Muhm, and P. B. Schoonmaker,
McDonnell Douglas Technical Services Co., Houston, Tx.; and R. J. Radar,
MDAC, Huntington Beach, Calif.

1. SUMMARY

This report describes a series of sensitivity analyses (trade studies) performed to select features and capabilities to be implemented in the new Plume Impingement Model being developed under Task Order D0717 of Contract NAS9-14960.

The objective of these studies was to ensure that this model will provide the performance required by the user community, but not be "loaded down" with features and capabilities for which there is no real need. A subordinate objective was to demonstrate that the correct decisions were made in defining the model capabilities, and thus build confidence in the model among the user community. The recommendations of this report are to be used to establish a final set of Level B Requirements for the Plume Impingement Model.

Sensitivity analyses were performed in study areas pertaining to geometry, flowfield, impingement, and dynamical effects. Recommendations based on these analyses are summarized in Table 1-1, reproduced from Section 5 for convenience.

TABLE 1-1 SUMMARY OF MODELLING RECOMMENDATIONS

MODELLING AREA	RECOMMENDED IMPLEMENTATIONS
4.1 Orbiter/Jet Geometry	• Include shadowing caused by the Orbiter mold'line, cabin, OMS-pod bulkhead, and tail. • Do not consider reflections of the plume.
4.2 Object Geometry	• Include some "first order" simplification in the object modelling. • The mesh size should be variable, and on the order of 10x10 in the near field. • Include back-side shadowing, and shadowing of one payload element by another payload subshape.
4.3 Flowfield	• Model the flowfield as patched source flow with radial streamlines. • Neglect effects on the flowfield due to nozzle scarfing and ambient atmosphere effects. • Include a "practical boundary" test. • If simultaneous firings of adjacent engines occur frequently, implement an ."equivalent engine" formulation.[a]
4.4 Impingement	• Calculate impingement pressure in the continuum regime using a modified newtonian formulation. • Calculate impingement pressure in the free-molecule regime using thermal accommodation analysis; use approximations for large impingement angles. • In the transitional regime, use a linear weighting function, based on the $\sin^2$ function, to combine continuum and free-molecule results.
4.5 Dynamical Effects	• Neglect plume impingement on the RMS for integrated simulations. Use off-line "stand-alone" analysis to identify gross RMS operating constraints.
4.6 Contamination	To be supplied.

[a] Additional NASA input required for final decision.

2. INTRODUCTION

It has been clear for some time now that a plume impingement modelling capability is required to conduct meaningful studies of payload proximity operations and payload handling operations. This is because the effects of RCS thruster plume impingement--both payload disturbances and contamination effects (see Figure 2-1)--are potentially the dominant factors driving the development of techniques for these operations.

It also appears likely that new modelling software will have to be developed to support the requisite mission analysis and mission planning studies. Existing plume-modelling software falls into two general classes: (1) high- fidelity programs which are too large, too slow and too unwieldy to be integrated with total on-orbit simulation programs, and (2) simple models which may not provide sufficient performance to satisfy the requirements of the anticipated Mission Planning and Analysis Division (MPAD) users. What is desired is a model providing high accuracy, fast execution, and small storage requirements. Reference 1 documents the final Level A requirements and structure for such a model, which is being developed under Task Order D0717 of contract NAS9-14960.

The objectives of this Plume Impingement Model Sensitivity Analysis Study Report are to establish the tradeoff factors between "cost" (in terms of storage, execution time, complexity) and performance (accuracy, flexibility), and thereby support Level B decisions on modelling approaches and features.

IMPINGEMENT
FORCE

IMPINGEMENT
MOMENT

CONTAMINANT
DEPOSITION/ABRASION

RCS PLUMES

ORBITER CONDUCTING
DEPLOYMENT/RETRIEVAL
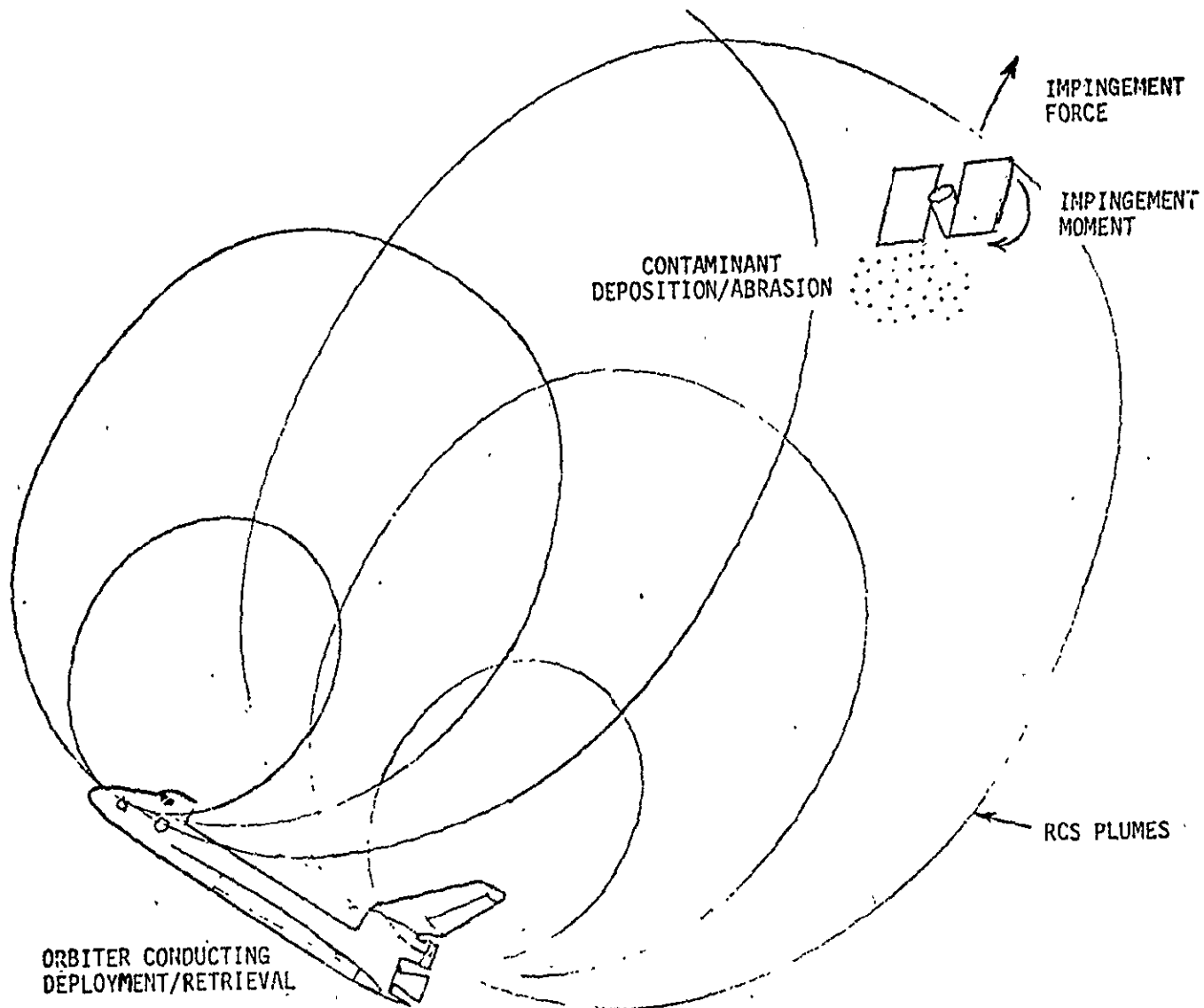
FIGURE 2-1 PLUME IMPINGEMENT PROBLEMS

3. STUDY METHODOLOGY

This section describes the sensitivity analysis study breakdown, and the analysis tools and basic data which were used by the MDTSCO/MDAC-West study team in performing the individual studies.

3.1 Study Breakdown

The basic organization of the Sensitivity Analysis Study task follows the Level A function/module breakdown of the Plume Impingement Model (Reference 1). Within each study area (e.g., Orbiter geometry, flowfields), modelling issues or alternate approaches are identified. No modelling issues are identified in the contamination area, since implementation of this module is not yet defined in detail. A dynamics study area was also established, even though vehicle dynamics are not part of the plume model itself, to explore implications of vehicle dynamics upon plume model requirements. Figure 3-1 shows the sensitivity analysis study breakdown superimposed upon the Level A function/module breakdown.

For each study area, individual studies were conducted to resolve the issues or decide among the alternate approaches; these individual studies are described in Section 4. Finally, the results of these independent studies are correlated, and potential interactions are considered. The results are integrated and presented in Section 5.

3.2 Analysis Tools and Basic Data

In the sensitivity analysis study, certain data and programs were used repeatedly. Data concerning the RCS thrusters and scientific payloads are listed here, along with general information pertaining to flowfield impingement, and contamination programs.

3.2.1 Orbiter RCS Data

The RCS thrusters (Reference 8) are Marquardt #R40 engines generating 870 pounds of thrust with an MMH/N_2O_4 propellant system. These engines can either fire continuously or operate in a 40 msec pulse mode. The oxidizer/fuel ratio is 1.6 and the chamber pressure is 152 psi.

Plume
Impingement
Model

(4.1) (4.2) (4.3) (4.4) (4.6)

Plume
Impingement
Executive
Module, PIEXEC

Orbiter/Jet
Geometry
Module, ORBJET

Orbiter/Jet
Geometry
Data Base

Object
Geometry
Module, OBGEOM

Object
Geometry
Data Base

Plume
Flowfield
Module, FLOFLD

Flowfield
Data Base

Impingement
Pressure
Module, IMPRES

Contaminant
Flux Module,
CONFLX

Contaminant
Flux Data Base

Interfacing

Initialization

Sequencing

Effective Jet
Force & Moment
Computation

Effective
Contaminant-flux
Computation

Coordinate
transformation

Orbiter
Shadowing* (4.1.1)

Orbiter
reflection* (4.1.2)

Jet Classification

Subshape
decomposition (4.2.1)

Element
subdivision (4.2.2)

Control point
designation

Payload
shadowing* (4.2.3)

Force & moment
integration (Spatial)

Moment-center offset

Coordinate
transformation

Local flow
regime*

Local flow
properties

Source Flow (4.3.1)
Thruster Scarfing (4.3.2)

Plume/Atmosphere (4.3.3)

Simultaneous
Multiple Firings (4.3.4)

Continuum-flow
Impingement
Pressure (4.4.1)

Free-molecule-flow
impingement
pressure (4.4.2)

Transition-flow
impingement
pressure (4.4.3)

Local
Contaminant
Flux

(4.5)

Vehicle
Dynamics

RMS Dynamics (4.5.1)

Propagation Effects (4.5.2)

*Tentative Function

6

FIGURE 3-1 PLUME MODEL LEVEL A FUNCTION/MODULE BREAKDOWN (FROM REFERENCE 1), SHOWING SENSITIVITY, ANALYSIS STUDY AREAS

The thrusters have bell nozzles with various amounts of scarfing (nozzle extension) determined by the Orbiter mold line; see Section 4.3.2 . For the basic (unscarfed) engine, the assumed lip angle is 16.0 degrees, the exit radius is 4.8 inches, and the expansion ratio (exit area: throat area) is 22:1. In this report, unless otherwise stated, the above basic-engine parameters are used.

These RCS engines are located in forward and aft modules on the Shuttle Orbiter, as shown in Figure 3-2 (Reference 8). The thruster identification number, thrust direction, and assumed location in station coordinates are presented in Table 3-1.

3.2.2 Payload Data

The two payloads of greatest interest for this study are the Long Duration Exposure Facility (LDEF) and the Multi-mission Modular Spacecraft-Solar Maximum Mission (MMS/SMM).

LDEF: The NASA/Langley LDEF is 30 feet in length; its actual cross-section is that of a twelve-sided regular polygon having a major diameter of approximately 14 feet (Figure 3-3). The primary structure consists of aluminum ring frames and longerons. This skeleton weighs approximately 7,000 pounds. Seventy-two experiment trays are mounted in the bays formed by the rings and longerons, adding about 7,000 pounds more in weight. LDEF is gravity-gradient stabilized and includes an 8-inch spherical viscous magnetic damper with a damping coefficient of up to 2 ft-lbs/(rad/sec) (Reference 2).

Unless stated otherwise in this report, LDEF is assumed to be a cylinder (30' x 14' D), weighing 15,000 pounds, with no damper. The mass center is assumed to be at the geometric center. The minimum principal moment of inertia is assumed to be 20,000 slug-ft^2 with the remaining two moments of inertia equal to 50,000 slug-ft^2.

MMS-SMM: The first of the Goddard Space Flight Center multimission modular spacecraft is the Solar Maximum Mission configuration, shown in Figure 3-4. The service section of the payload is the basic MMS structure. This roughly triangular section contains replaceable subsystem modules, including an

Thruster location ─────────────────────────────────── Thrust reaction

    F = fwd module   A = +X
    L = aft left   X │   F = -X
    R = aft right   X │   X │   L = +Y or + rotation vernier
Propellant manifold numbers ──────────┘   X   R = -Y or - rotation vernier
    (1 through 5)   U = +Z
                                                      D = -Z

↑ Direction of thruster plume

⇧ Direction of vehicle motion
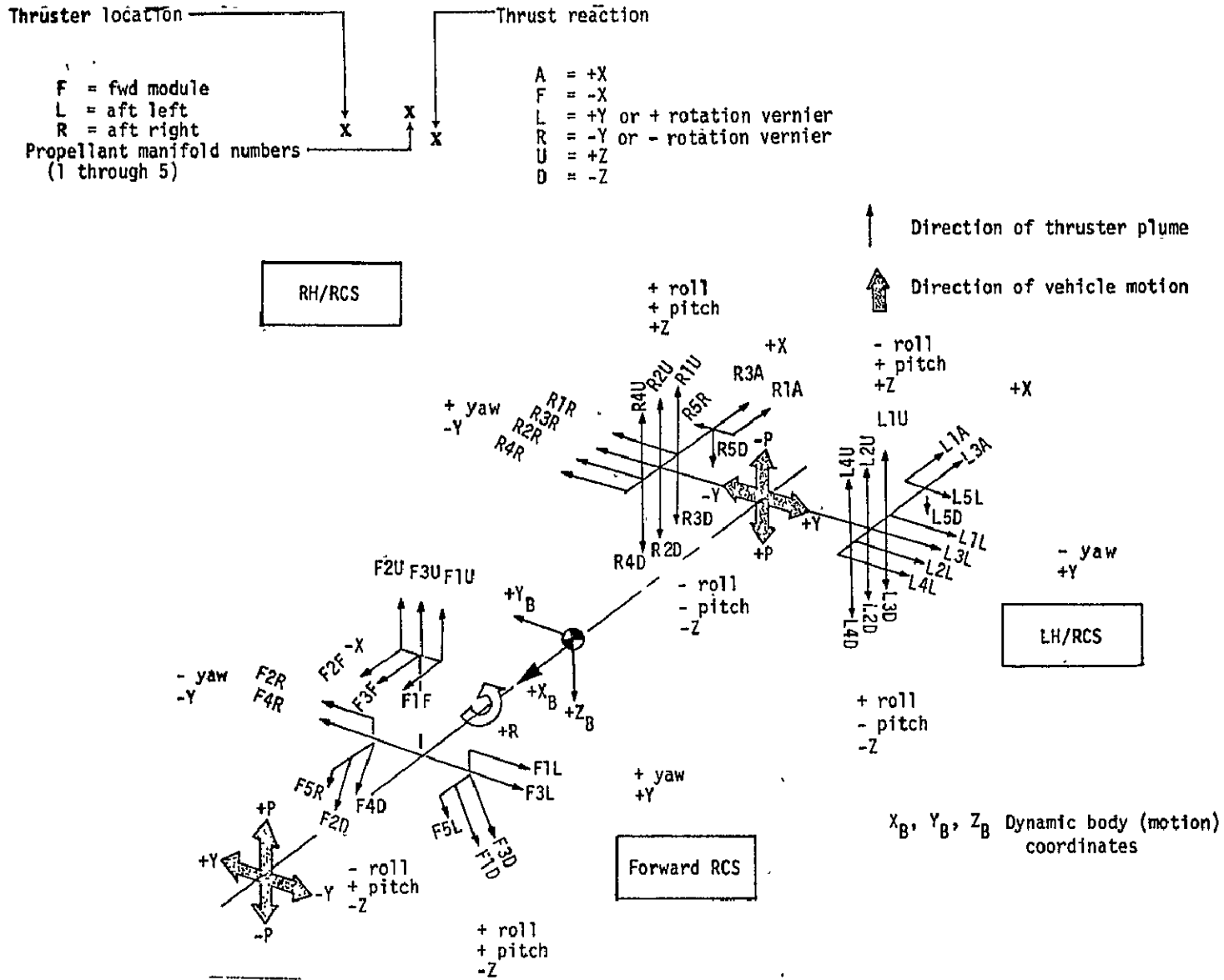
FIGURE 3-2   RCS THRUSTER NUMBER, DIRECTION OF THRUST, AND LOCATION

TABLE 3-1 RCS THRUSTER IDENTIFICATION AND LOCATION

Thrust Direction	Thruster Identification Number		Thruster Locations in Station Coordinates[d], in.		
	Old	New	X_0	Y_0	Z_0
Forward RCS Thrusters					
-X	132	F2F	327.277	14.654	392.955
	122	F3F	327.383	0.0	394.450
	112	F1F	327.277	-14.654	392.955
+Y	113	F1L	362.671	-55.631	373.728
	123	F3L	364.708	-58.579	359.250
-Y	134	F2R	362.671	55.631	373.728
	144	F4R	364.708	58.579	359.250
+Z	135	F2U	350.925	14.394	399.588
	125	F3U	350.917	0.0	400.818
	115	F1U	350.925	-14.394	399.588
-Z	136	F2D	333.840	49.814	372.350[a]
	116	F1D	333.840	-49.814	372.350[a]
	146	F4D	348.440	54.839	373.566[a]
	126	F3D	348.440	-54.839	373.566[a]
-Z (Vernier)	158	F5R	324.350	53.830	357.900[a]
	157	F5L	324.350	-53.830	357.900[a]
Aft RCS Thrusters					
+X	331	R3A	1555.293	137.00	473.058[b]
	311	R1A	1555.293	124.00	473.058[b]
	231	L3A	1555.293	-137.00	473.058[b]
	211	L1A	1555.293	-124.00	473.058[b]
+Y	243	L4L	1516.00	-135.21	459.00
	223	L2L	1529.00	-135.21	459.00
	233	L3L	1542.00	-135.21	459.00
	213	L1L	1555.00	-135.21	459.00
-Y	344	R4R	1516.00	135.21	459.00
	324	R2R	1529.00	135.21	459.00
	334	R3R	1542.00	135.21	459.00
	314	R1R	1555.00	135.21	459.00
+Z	245	L4U	1516.00	-132.00	480.50
	225	L2U	1529.00	-132.00	480.50
	215	L1U	1542.00	-132.00	480.50
	345	R4U	1516.00	132.00	480.50
	325	R2U	1529.00	132.00	480.50
	315	R1U	1542.00	132.00	480.50
-Z	246	L4D	1516.00	-111.945	437.403[c]
	226	L2D	1529.00	-111.00	440.00[c]
	236	L3D	1542.00	-110.055	442.597[c]
	346	R4D	1516.00	111.945	437.403[c]
	326	R2D	1529.00	111.00	440.00[c]
	336	R3D	1542.00	110.055	442.597[c]
-Z (Vernier)	257	L5D	1565.00	-118.00	455.44
	358	R5D	1565.00	118.00	455.44
-Y (Vernier)	357	R5R	1565.00	143.38	459.00
+Y (Vernier)	258	L5L	1565.00	-143.38	459.00

[a] Canted 37° outboard in the Y-Z plane.
[b] Canted up 10° in the X-Z plane.
[c] Canted aft 12° in the X-Z plane and 20° outboard in the Y-Z plane.
[d] Thruster mount attach points.

9

X

YAW

S_B

F

Z

VELOCITY
VECTOR

E

ROLL

D

Y

C

PITCH

B

A

S_A

LOCAL
VERTICAL
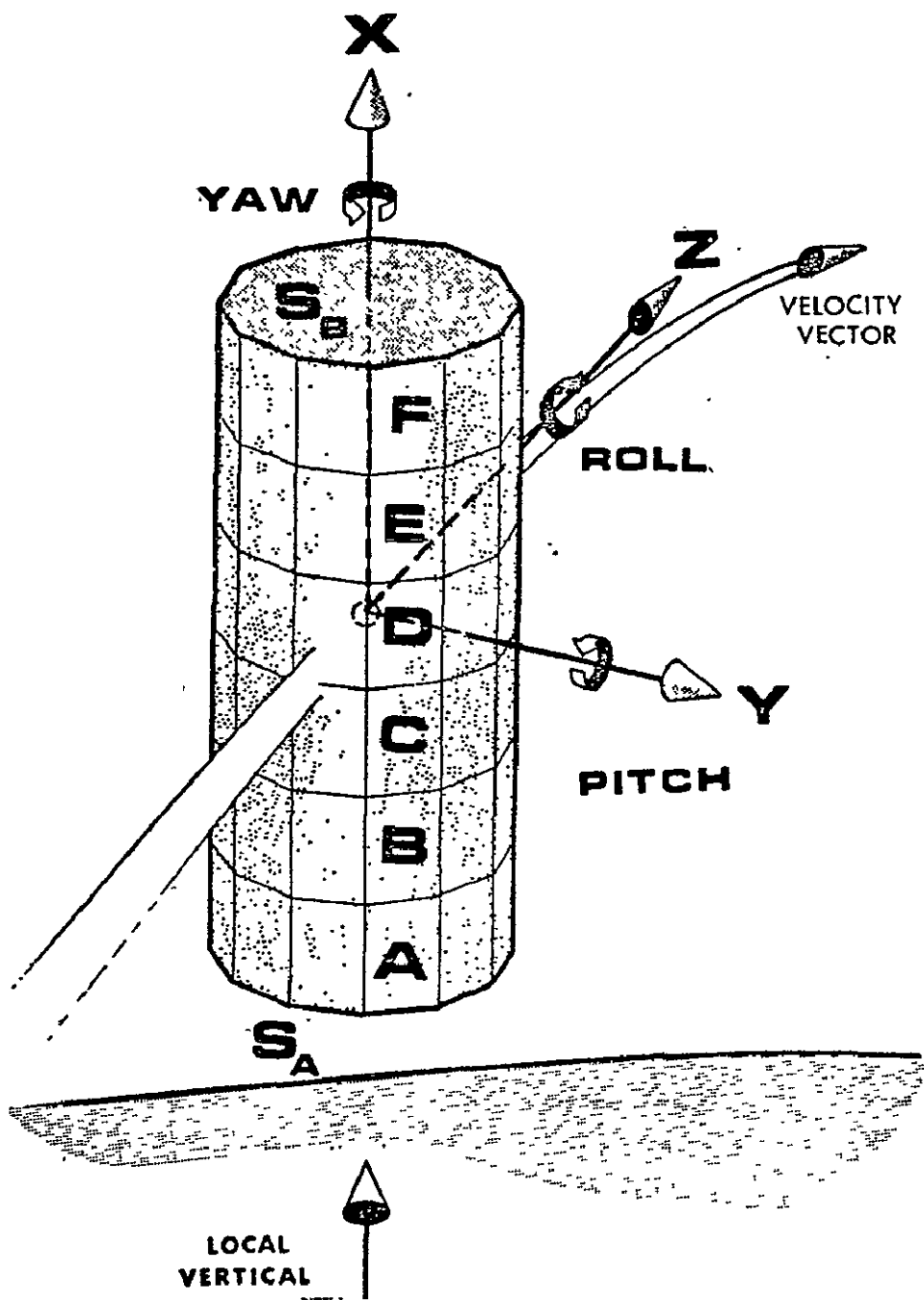
FIGURE 3-3   LDEF PAYLOAD CONFIGURATION AND NOMINAL ON-ORBIT ORIENTATION
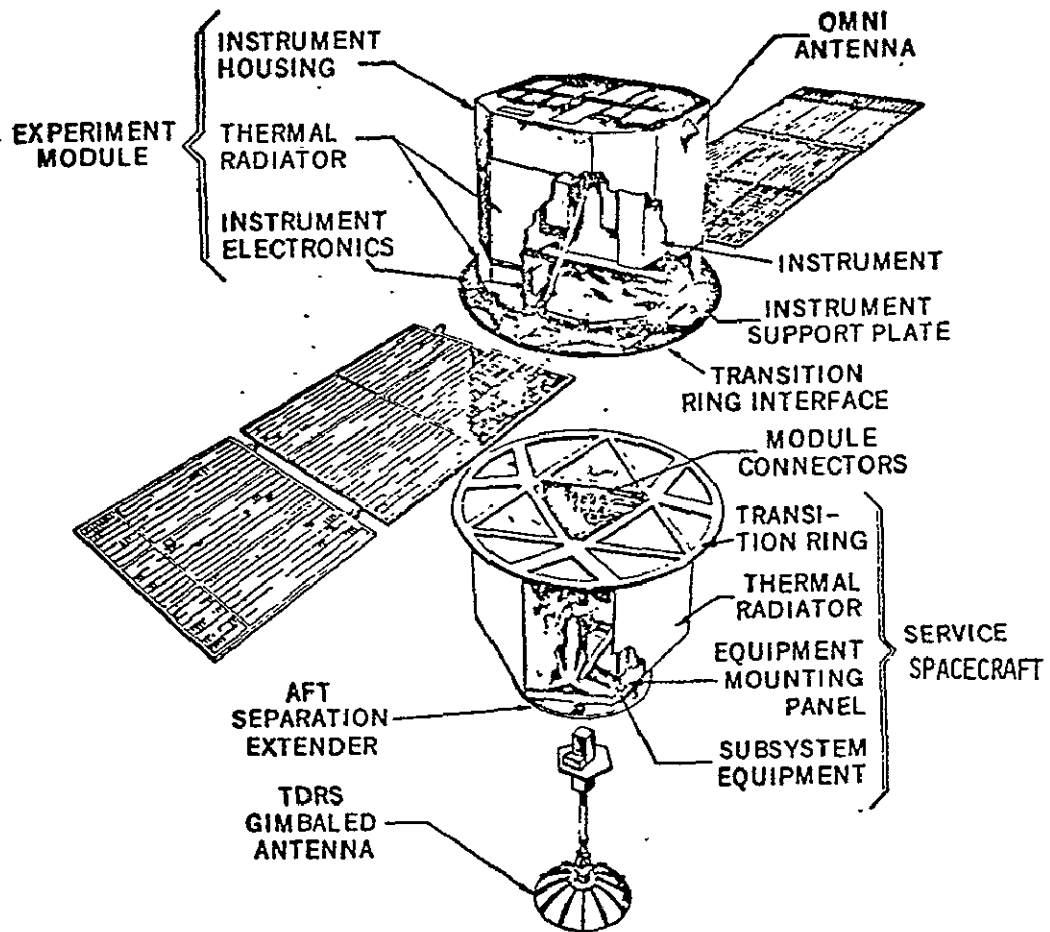
FIGURE 3-4   MMS/SMM SPACECRAFT CONFIGURATION

11

attitude control system of reaction wheels and magnetic torquers. The maximum capability of the momentum wheels to absorb external disturbance torques and maintain control of the spacecraft is approximately 12 lb-ft-sec (Reference 3).

Unless stated otherwise in this report, the MMS/SMM payload is modelled as a cylinder of 14' length and 7.2' diameter with two solar panels 8.7' on a side (see Figure 3-5). Its mass is assumed to be 4000 pounds, with principal inertias being 2000, 2000, and 680 slug-ft^2. The center of mass is assumed 10" from the geometric center of the cylindrical body.

3.2.3 Flowfield Programs

Two computer codes are used in sequence to provide plume flowfield data required for the sensitivity analysis study: (1) the one-dimensional equilibrium. (ODE) program (Reference 4) developed at NASA/Lewis, and (2) the method of characteristics (MOC) program developed by Lockheed/Huntsville (Reference 5). Both programs have been developed, improved, and extensively used for more than ten years. They are considered the "standard" programs in plume characterization by the industry.

ODE: Basically, this program calculates frozen or equilibrium chemical compositions, species concentrations and thermodynamic properties for a complex chemical system in a variety of gasdynamic flow problems under the assumption of a quasi-one-dimensional flow.

The rocket performance calculation option of ODE was used to obtain the thermochemical properties required by the MOC program. To obtain these data for a rocket nozzle, ODE requires information on chamber pressure, propellants, and oxidant/fuel (O/F) mixture ratio (see Section 3.2.1). In addition, either a prescribed pressure drop or area ratio is needed in the rocket performance calculation.

MOC: This program was developed for calculating a steady, two-dimensional, supersonic, and compressible flow in a rocket nozzle and/or plume including the effects of real gas and O/F gradients.

7.17

8.83

8.67   8.67

14.0

0.83

8.67   8.67

(DIMENSIONS IN FEET)
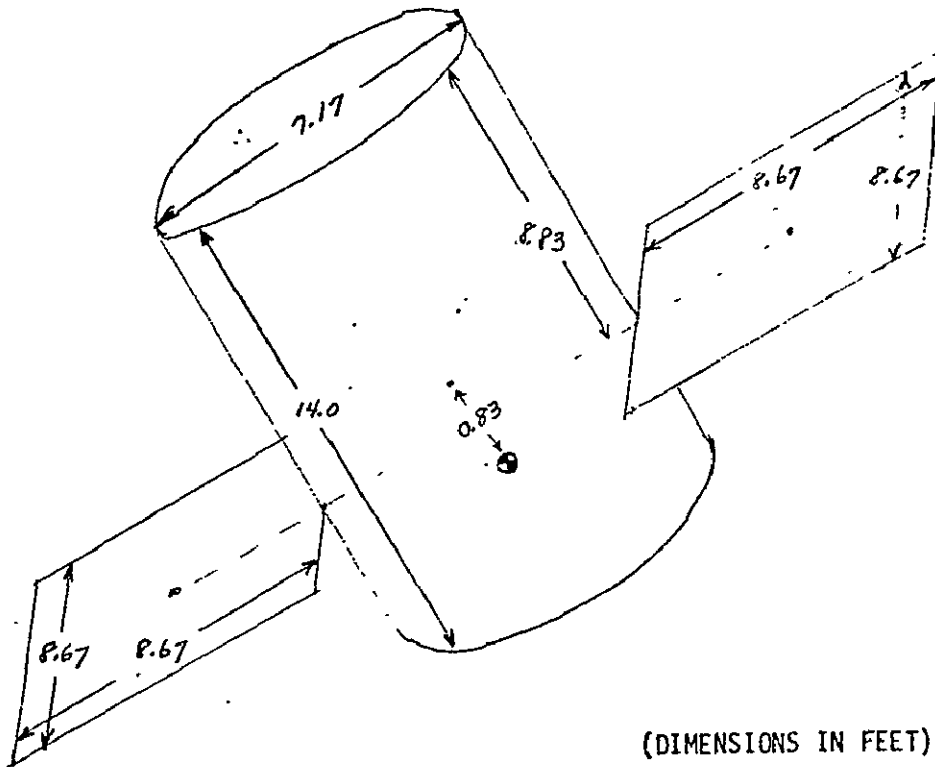
FIGURE 3-5   ASSUMED MMS/SMM CONFIGURATION

To run this program, the thermodynamic properties of a real gas mixture, and a description of nozzle geometry and external pressure boundary conditions must be input. The program then generates the flowfield and thermodynamic properties along "left-running characteristic" lines inside the nozzle and plume (see Figure 3-6). To provide the flowfield data for the plume impingement (PLIMP) program (to be discussed in the following section), we have used the nozzle exit plane start option of the MOC program with the real gas properties obtained from ODE, and nozzle parameters as listed in Section 3.2.1. The nozzle flow was assumed to expand into a vacuum.

No shock waves were simulated in the flowfield, due to the exit plane start option; however, both inviscid and viscous flowfield data (i.e., including boundary layer) were generated by the program. These flowfields were calculated out to 250 feet in the axial direction and 200 feet in the radial direction.

Although the MOC program is very versatile code, it becomes inefficient and less accurate as it tries to compute beyond the continuum regime of the flowfield. (See Section 4.3 for methods of providing flowfield data at greater distances.)

3.2.4 Impingement Programs

Two computer programs used in the sensitivity analysis study for computing plume impingement effects are (1) the PLIMP program developed by Lockheed/ Huntsville (Reference 6), and (2) the Quick-Look Disturbance Program (QLDP) developed by MDTSCO (Reference 7). Like ODE and MOC, PLIMP has also been developed, improved and extensively used for more than ten years. The QLDP program was used mainly for a quick-look "order of magnitude" analysis.

PLIMP: This program computes forces, moments, and heating rates on sur-faces immersed in or subjected to a one-rocket exhaust plume environment. Program capabilities include the treatment of continuum, transitional, and free molecular flow regimes for arbitrary body shapes. In addition, body shadowing effects can also be calculated by the program.

14
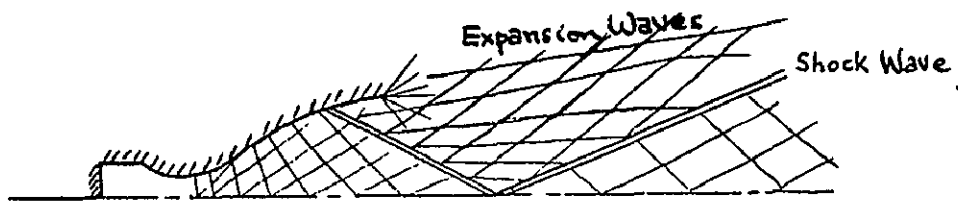
FIGURE 3-6 GENERATION OF FLOWFIELD PROPERTIES ALONG
LEFT-RUNNING CHARACTERISTIC LINES USING MOC

To run this program, plume flowfield data generated with the MOC program, as well as descriptions of the engine, reference, and subshape coordinate systems and subshape geometries, must be input. The PLIMP program first reads in the MOC-generated raw flowfield data from a tape, then rearranges, orders, and stores these data for more convenient access. Impingement calculations are then performed on each elemental area resulting from subdivision of the subshape (see Section 4.2.2). The resulting forces and moments are output in a specified coordinate system.

PLIMP requires fairly long computer time per run case because of its complexity and versatility.

QLDP: QLDP is a quick-look disturbance program developed by MDTSCO for determining "order of magnitude" plume impingement disturbances. It is used for offline analysis of approach trajectories, computing plume-induced payload dynamics.

The payload and Orbiter are modelled in only two dimensions; a plane of symmetry containing all jets is assumed. The Orbiter-relative payload initial state is input, along with time histories of payload state and thruster firings. Impingement forces and moments are computed using a MDTSCO-developed curve fit to MDAC-West data (Section 4.3.1) and the newtonian impingement formulation (Section 4.4), neglecting shadowing (Sections 4.1.1, 4.2.3). State perturbations due to these forces and moments are computed and propagated for each time interval. All motion is three degree-of-freedom: two linear coordinates and one angle.

3.2.5 Contamination Programs

(This section is to be supplied at a later date.)

16

4.. INDIVIDUAL SENSITIVITY ANALYSIS STUDIES

Individual sensitivity analysis studies are independently documented in the following subsections. Each individual study deals with a specific modelling issue in a specific area of the Level A Plume Model Function/ Module Hierarchy (Section 3.1).

A standardized structure is used for the documentation of each individual study, in each 4._._ subsection:

4._._.1 The question - What is the question to be answered or what are the modelling alternatives to be considered? Some background information will often be included, relating to physical phenomena, operational aspects, or other considerations.

4._._.2 Tradeoff factors/considerations - How will the alternatives be implemented? What will be the qualitative "cost" in terms of complexity, storage, execution time, etc.? How will the alternatives affect the performance of the model (i.e., accuracy, flexibility)?

4._._.3 Analysis approach - This section explains the theory behind the alternatives and, if the problem is to be solved analytically, how the solution will be obtained. For those problems using computer programs, the type and number of runs made is included here along with any assumptions made. If any payloads are to be used in the analysis, their position and orientation are also given.

4._._.4 Analysis results - The results of the mathematical and/or computational analysis are presented and evaluated in terms of cost and performance.

4._._.5 Preliminary conclusions and recommendations - Based on evaluation of the analysis results, conclusions and recommendations are made. These are preliminary since they depend only on the individual study under consideration; they may be revised when the interaction between the individual studies is considered in Section 5.

4.1 Orbiter/RCS Geometry Modelling Approaches

The studies documented in this section deal with alternate formulations of the Orbiter/jet geometry module, ORBJET. The following functions are allocated to ORBJET (Reference 1):

- Determine the jet classification (primary, vernier, scarfed,. . .), using the jet tag and a table look-up.

- .Determine the coordinate transformation from the object-fixed axes to the thruster axes for the proper jet.

- Determine, if necessary, Orbiter shadowing parameters (size and location of Orbiter surfaces which may shadow parts of the payload).

- Determine, if necessary, Orbiter reflection parameters (size and location of Orbiter surfaces which may reflect plume exhaust onto a payload).

The following subsections describe studies which were conducted to answer the following questions:

- Is the capability to simulate Orbiter shadowing of RCS plumes required in the model?

- Is the capability to simulate Orbiter reflection of RCS plumes required in the model?

Basic Orbiter and RCS data used in the sensitivity studies are defined in Section 3.2.1.

18

4.1.1 Orbiter Shadowing of RCS Plumes

4.1.1.1 The Question

Is it necessary to include an Orbiter shadowing capability in the plume impingement model?

Two types of Orbiter shadowing of RCS plumes may be considered. One of these is due to the moldline (Orbiter skin contour) around a thruster port and the other is due to the intruding Orbiter structural shapes,. such as the cabin, wings, tail and bulkheads. Both types of Orbiter shadowing can block the "line-of-sight" from a point on a payload or RMS arm to a thruster (similar to the payload subshape/sub-shape shadowing considered in Section 4.2.3).

4.1.1.2 Tradeoff Factors/Considerations

Implementation: To model Orbiter shadowing, we must first identify those parts of the Orbiter structure in the vicinity of RCS thrusters which may cause shadowing of a plume during payload proximity operations, then generate parametric data representing their geometry.

To implement moldline shadowing, the model would represent the Orbiter skin by the tangent plane at the thruster port, and implement the test with a simple vector dot-product operation.

Intruding objects would be represented as either circular or polygonal flat plates, specified in Orbiter station coordinates. For a particular thruster and object, the model would then generate the thruster-referenced parameters of the "shadow zone" created by the object: a cone for a circular plate, a "pyramid" for a polygonal plate. Each element is then tested to see if it falls inside any of the shadow zones for that thruster.

19

"Cost" Factors: Implementing Orbiter shadowing would require extra storage and increase complexity in programming. Additional execution time is also required for the shadowing tests themselves. However, these tests may save some execution time, due to bypassing impingement computations -- particularly for close-in operations.

Performance Factors: Neglecting the Orbiter shadowing effects would be expected to cause significant force/moment errors for payloads at close ranges.

4.1.1.3 Analysis Approach

Three different Orbiter substructures were considered for assessing Orbiter shadowing effects (Figure 4.1.1-1): (1) the Orbiter cabin for the forward +Z jet shadowing, (2) the Orbiter OMS-pod bulkhead for the aft +Z jet shadowing, and (3) the Orbiter moldline for the forward ±Y jet shadowing.

For modelling Orbiter shadowing, both the cabin and the OMS-pod bulkhead were represented by circular plates with the plate diameters taken equivalent to the respective substructures in shadowing. The moldline was represented by a flat plate placed parallel to the nozzle exit plane. Figure 4.1.1-2 depicts the various Orbiter shadowing representations.

Various objects including LDEF, MMS/SMM, and RMS were included in the Orbiter shadowing study. LDEF, MMS/SMM, and RMS were realistically placed at various locations and orientations for the cabin shadowing effect, while only LDEF was considered for the moldline and the bulkhead shadowing effects. The individual object location and orientation with respect to each RCS engine are also shown in Figure 4.1.1-2.
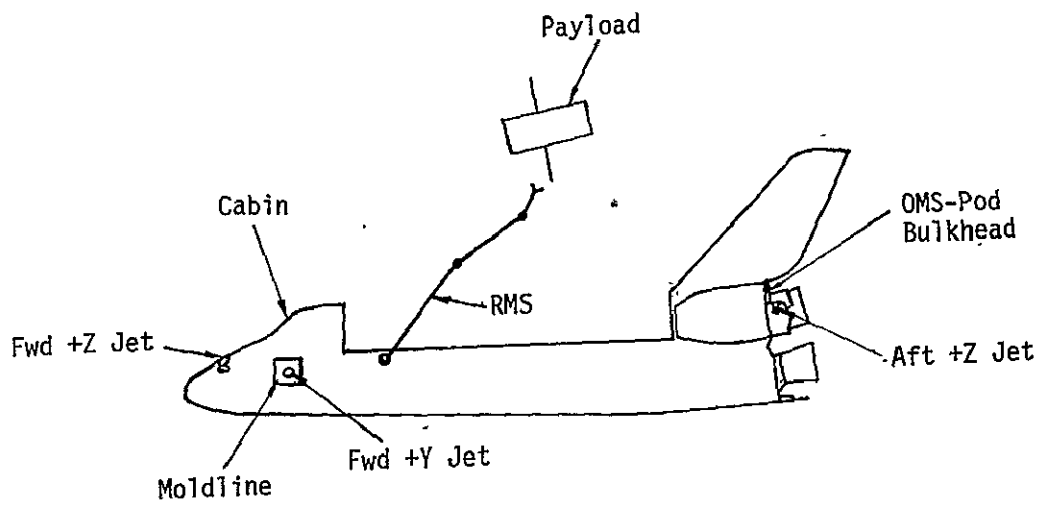
FIGURE 4.1.1-1 JETS AND ORBITER SUBSTRUCTURES ANALYZED IN THE ORBITER SHADOWING STUDY
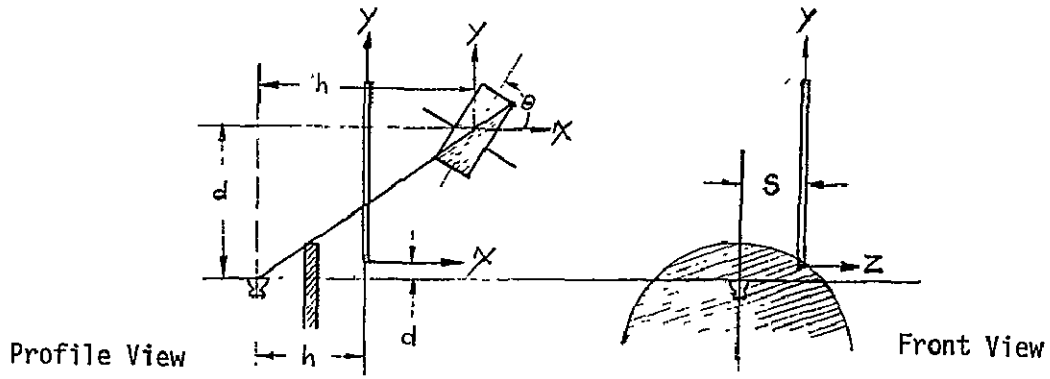
(a) Cabin Shadowing of Fwd +Z Jet on LDEF, MMS, and RMS
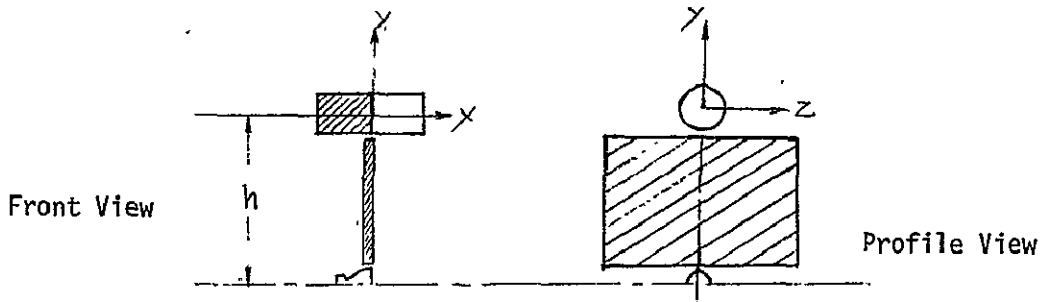
(b) Moldline Shadowing of Fwd +Y Jet on LDEF ·
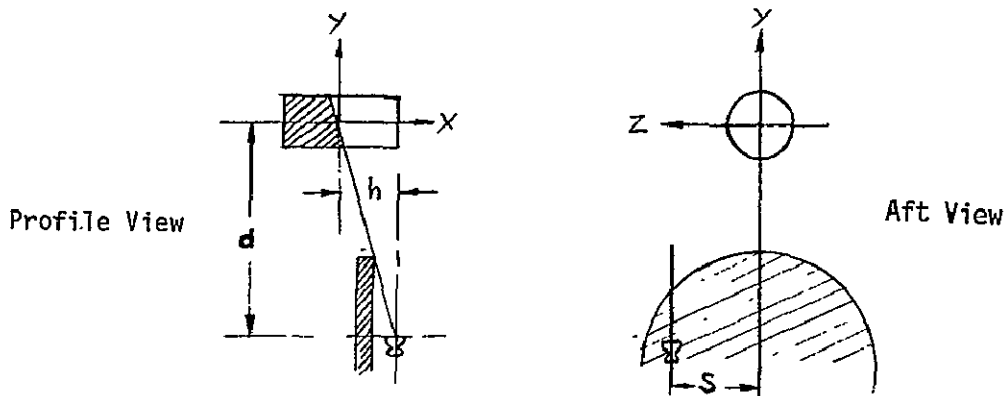
(c) Bulkhead Shadowing of Aft +Z Jet on LDEF

FIGURE 4.1.1-2   SCHEMATIC DRAWINGS OF VARIOUS   ORBITER SHADOWING
REPRESENTATIONS AND OBJECT LOCATIONS AND ORIENTATIONS

Making use of the PLIMP program (Section 3.2.4), impingement calculations were performed for all the Orbiter shadowing combinations discussed in the previous paragraph. Each run was made with and without the Orbiter shadowing option enabled. Both inviscid and viscous flowfields were provided by MOC (Section 3.2.3). The inviscid flowfield was used in the cabin and bulkhead shadowing cases, while the high angle viscous flow-field was used in the moldline shadowing case.

Modified Newtonian impingement pressure (Section 4.4:1) was used in all the runs made; the mesh fineness used was between 10 x 10 and 20 x 20 (Section 4.2.2) for all the object subshapes.

4.1.1.4 Analysis Results

Table 4.1.1-1 provides case-by-case performance data for the runs made to analyze Orbiter shadowing. Note the substantial errors occurring for some test cases -- over 100% in force magnitude and 10° in force direction; up to 50% in moment magnitude and 5° in moment direction.

Typical computer time in terms of Univac 1108 Central Arithmetic Unit was roughly 25 seconds per run. Furthermore, all the runs with shadowing took slightly less time than those without shadowing.

4.1.1.5 Preliminary Conclusions and Recommendations

Based upon the above study, we have found that neglecting Orbiter shadowing effects can cause significant errors in both force and moment calculations. Furthermore, inclusion of the shadowing effects may actually save computer time.

23

TABLE 4.1.1-1 PERFORMANCE VARIABLES FOR ORBITER SUBSHAPE SHADOWING

SHADOWING SURFACE	TEST CASE[a]					RAW PERFORMANCE DATA						SENSITIVITY[c]			
	Number	Location & Orientation[b]				With/Without Orbiter Shadowing						Force Errors		Moment Errors	
		d (ft)	h (ft)	s (ft)	θ (deg)	F_x (lb)	F_y (lb)	F_z (lb)	H_x (lb-ft)	M_y (lb-ft)	M_z (lb-ft)	ΔMag (±%)	ΔDir (deg)	ΔMag (±%)	ΔDir (deg)
Cabin	L1	40.	69.4	-	0.	1.753/1.753	0.104/0.309	-	-	-	-2.223/-2.69	1.4	6.6	21.0	-
	L2	40.	69.4	-	90.	1.496/1.862	0. /0.04	-	-	-	-9.704/-6.513	24.5	1.2	32.9	-
	L3	60.	103.9	-	0.	0.622/0.622	0.063/0.17	-	-	-	-0.967/-0.919	3.1	9 5	5.0	-
	L4	60.	103.9	-	90.	0.571/0.801	0. /0.041	-	-	-	-3.856/-1.943	40.5	2.9	49.6	-
	L5	60.	103 9	-	120.	0.588/0.829	0.34 /0 478	-	-	-	-5.766/-4.025	40.9	0.1	30.2	-
	H1	60.	103.9	-	20.	0.402/0.534	0.147/0.2	-	-	-	-2.845/-1.755	33.2	0.5	38.3	-
	M2	60.	103.9	-	45.	0.275/0.392	0.253/0.369	-	-	-	-3.011/-2.074	44.1	0.7	31.1	-
	H3	60.	103.9	-	70.	0.117/0.162	0.197/0.287	-	-	-	-1.948/-1.482	43.8	1.3	23.9	-
	R1	2.65	27.39	9.	90.	1 613/1.646	0. /0.	0.53/0.541	-17.148/-17.224	0./0.	-52.182/-52.411	2.1	0.0	0.4	0
Holdline	L6	0.	29.5	0.	0.	0. /0.	0.578/0.778	0./0.	0./0.	0./0.	4.85/3.629	34.6	0.0	25.2	0.
Bulkhead	L7	78.5	37.75	0.	0.	-2.62/-2.62	9.847/21.043	-1.201/0.	0./0.	6.55/0.	102.38/77.045	106.7	10.3	24.9	3.2
	L8	78.5	37.75	5.05	0.	-2.604/-2.604	8.687/20.755	-1.894/-1.59	0./0.	15.264/5.6	94.45/76.22	126.4	12.0	20.1	5.0

NOTES:

[a] L denotes LDEF
H denotes HIS/SRM
R denotes RMS

[b] See Figure 4.1.1-2

[c] With respect to the results with Orbiter shadowing

Therefore, we recommend that the Orbiter shadowing capability be implemented in the plume impingement model.

4.1.2 Orbiter Reflection of RCS Plumes

4.1.2.1 The Question

Is it necessary to account for the effect on the payload due to the reflection
of the RCS plumes from Orbiter surfaces? Since the reflection mechanism is
different depending on the impingement regime (free molecular, transitional,
or continuum), the question must be answered for each regime. These impingement
regimes are discussed in Section 4.4. One Orbiter surface which could
reflect an RCS plume enough to effect a payload is the tail, which potentially
could reflect an aft +Z RCS engine plume.

4.1.2.2 Tradeoff Factors/Considerations

To assess cost and performance factors, consideration of how plume reflection
would be implemented in the model is necessary.

Implementation: To implement plume reflection in the model, a technical effort
would be required to analyze and develop techniques to calculate the plume
reflection and the effect of this reflection on the payload. The developed
techniques and associated equations and logic would then be incorporated into
the model.

"Cost" Factors: The costs of implementing plume reflection are: (1) the cost
associated with developing the necessary techniques and implementing the tech-
niques into the model, and (2) the associated storage and execution time.

Performance Factors: Since the effect on the payload due to plume reflection
from the tail is expected to be minor, the increase in accuracy in the calculation
of the plume impingement effects including the effects of plume reflection
should be minimal.

4.1.2.3 Analysis Approach

The impingement Knudsen number (ratio of the molecular mean-free-path in the
plume, λ_∞, to the characteristic dimension of the impinged surface, L_s) was
calculated for the case of an aft +Z RCS plume impinging the tail surface

26

(Section 4.4 includes a discussion on the impingement Knudsen number and how it is used to determine the impingement regime). If the impingement mechanism is free molecular or transitional, the impinging molecules will be re-emitted from the surface in a random manner; some of them could impact the payload. If the impingement mechanism is continuum in nature, a boundary layer will be formed which will build up toward the top of the tail. Impingement regimes on the tail were calculated and the boundary layer height and mass flow in the boundary layer were calculated.

4.1.2.4 Analysis Results

The surface Knudsen number (which varies from 0.01 close to the tail base to 0.0007 at the tail tip) reveals the impingement mechanism of the aft +Z RCS plume on the tail is continuum in nature over the entire tail surface. Therefore, no molecules will be re-emitted from the surface. A boundary layer is formed (Figure 4.1.2-1) which originates close to the tail base and builds as the plume flow moves up the tail surface. The maximum boundary layer thickness (which exists at the tail tip) is on the order of 17 inches; however, the mass flow in the boundary layer is on the order of 0.2 percent of the total mass flow of the RCS engine.

4.1.2.5 Preliminary Conclusions and Recommendations

Based on the above analysis, our conclusions and recommendations are:

- Since the RCS plume impingement on the tail is continuum in nature and the mass flow in the boundary layer is such a small percentage of the total RCS mass flow, the effect of plume reflections on the payloads is negligible. Therefore, we recommend that reflection of RCS plumes not be included in the model.

Boundary Layer

Orbiter Tail

Shock

Not to Scale
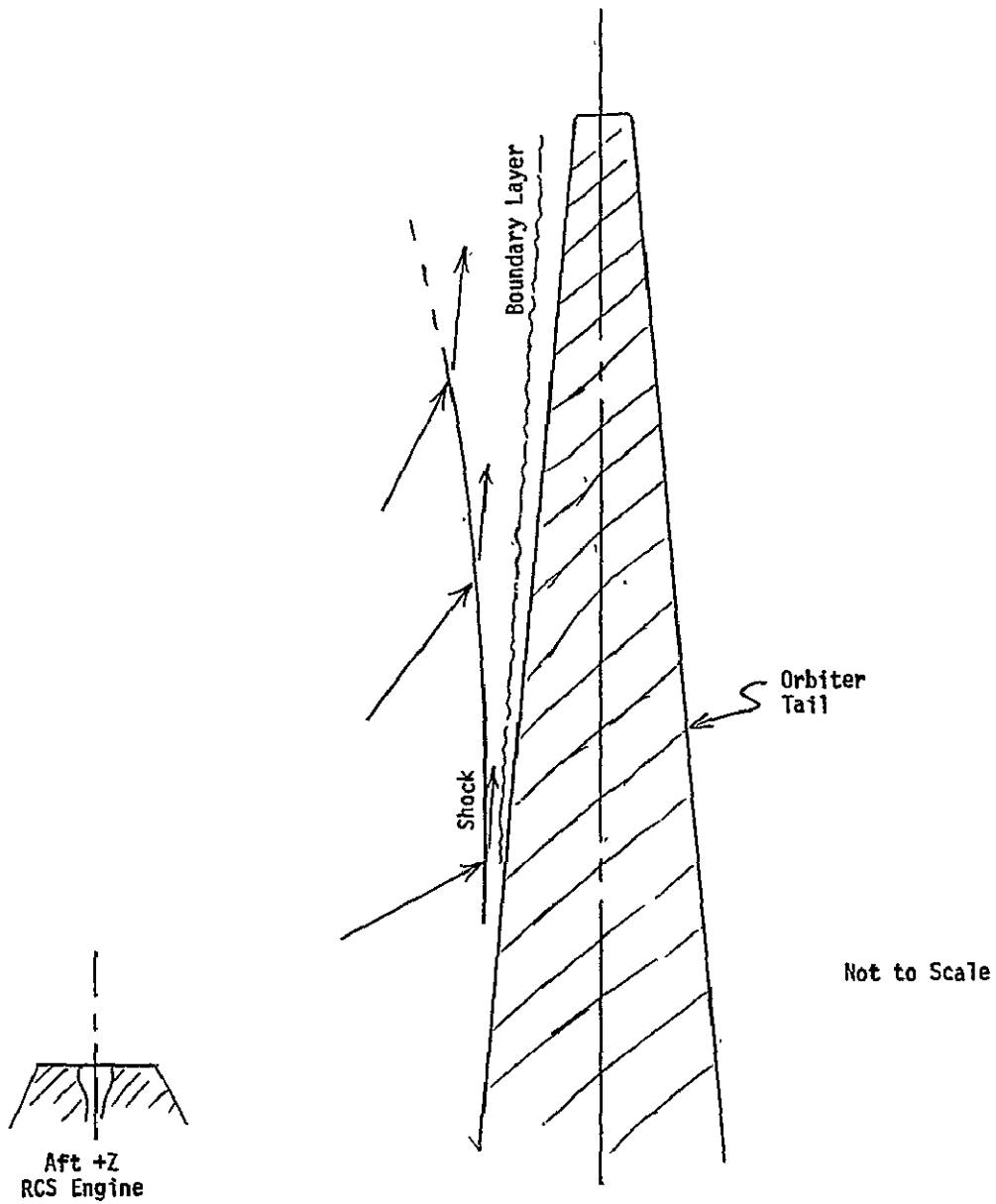
Aft +Z
RCS Engine

FIGURE 4.1.2-1.   SKETCH OF CONTINUUM FLOW AROUND TAIL DUE TO
                  AFT +Z RCS ENGINE PLUME

4.2 Object Geometry Modelling Approaches

The studies documented in this section deal with alternate formulations of the Object Geometry Module, OBGEOM. The following functions are allocated to OBGEOM (Reference 1):

- Decompose object into subshapes (e.g., cylinders, flat plates).

- Decompose subshapes into "elemental flat plates".

- Designate "contamination control points" for computation of contaminant flux.

- Transform from subshape axes to thruster axes and from thruster axes to object axes.

- Compute, if necessary, object shadowing (the shadowing of one part of the payload by another).

- Spatially integrate the elemental forces and moments.

- Compensate for any offset of the object moment center (e.g., c.g. offset).

The following subsections describe studies which were conducted to answer the following questions:

- How much can the subshape geometry representation be simplified (e.g., 12-sided polygon⇒cylinder ⇒flat plate)?

- How fine an elemental subdivision ("mesh size") is required for the model? Should the mesh size be fixed or variable?

- Is the capability to simulate object shadowing required in the model?

Basic object geometry data used in these studies are defined in Section 3.2.2.

29

4.2.1 Representation of Object Geometry

4.2.1.1 The Question

Is a drastic simplification of payload geometry representation acceptable in the new plume impingement model? Currently, there are three payload configurations under consideration: LDEF, MMS/SMM, and Skylab. Among these payloads, we only have detailed information on LDEF and Skylab geometries. Therefore, the MMS/SMM payload will not be discussed in the present study.

4.2.1.2 Tradeoff Factors/Considerations

Implementation: In general, for the purposes of analysis, any complicated payload geometry may be represented and approximated with varying levels of fidelity. The first step in the approximation would be to replace the actual payload geometry by a collection of simple subshapes, e.g., cylinder, circular plate, rectangular plate, etc. The next step would be to further approximate these simple subshapes by either performing a direct subdivision of each subshape into smaller elements, or making further simplifications to the subshapes and then subdividing the resulting shapes into elements.

Since detail information on the MMS/SMM configuration is unavailable at present, only LDEF and Skylab configurations are presented in Figure 4.2.1-1. For the present study the actual LDEF configuration is either represented as a cylinder or a "T-plate" approximation. The Skylab configuration is represented either by a collection of circular cylinders and rectangular plates, or approximated by boxes and rectangular plates as shown (see References 7 and 9).

"Cost" Factors: The direct benefits of simplification of object representation are: fairly minor savings of storage requirements and computer time, and a simplification of programming. There is also an indirect saving of computer time, due to the use of coarser mesh sizes (see Section 4.2.2) appropriate with simplified geometries.

Actual LDEF   Approximation by Cylinder   "T-Plate" Approximation

(a) LDEF CONFIGURATION

Solar panels
seen edge-on

Solar panels
seen broadside

Cylinder

Box

Rectangular Plates

Rectangular Plate
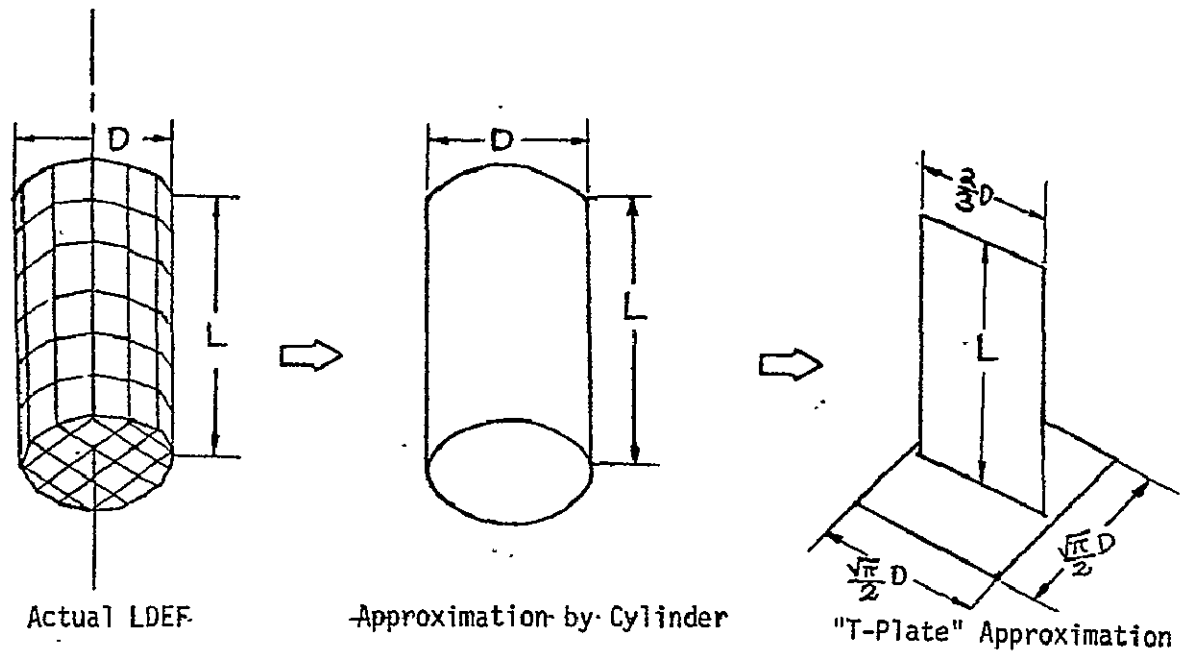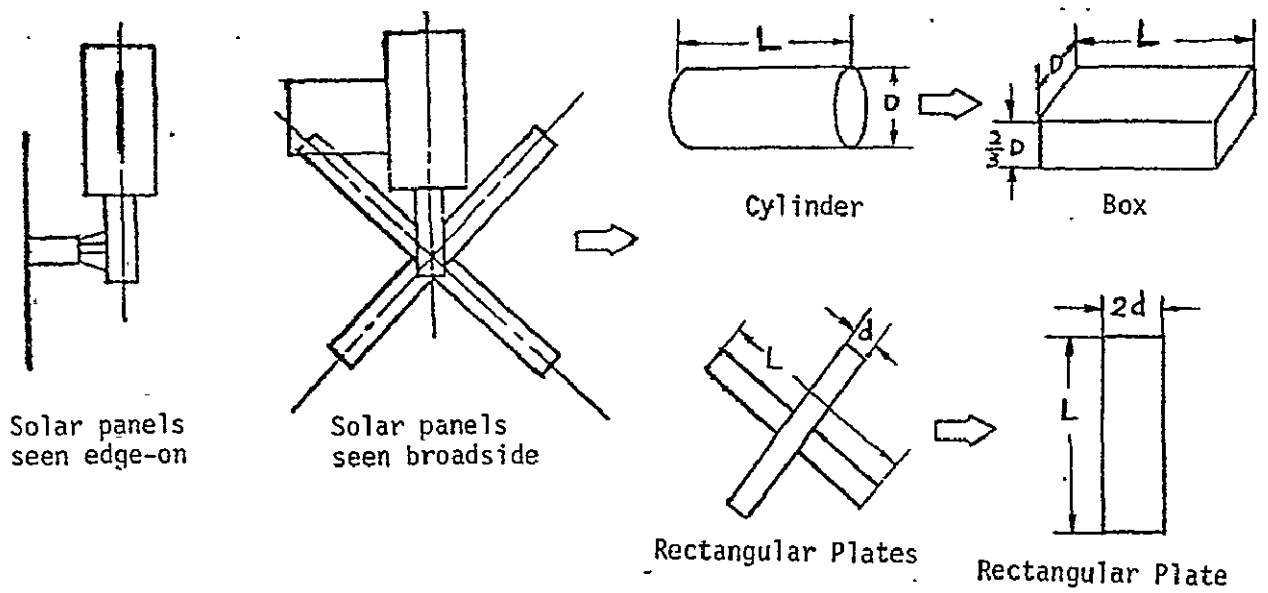
(b) SKYLAB CONFIGURATION

FIGURE 4.2.1-1   LDEF AND SKYLAB CONFIGURATIONS AND THEIR SIMPLIFYING REPRESENTATIONS

31

Performance Factors: In general, a closer representation of an original
payload geometry will give better accuracy in impingement calculations. On
the other hand, a drastic simplification of the payload geometry may induce
substantial errors in the impingement calculations.

4.2.1.3 Analysis Approach

In order to study the effect of subshape representation,the PLIMP program
(Section 3.2.4) was used to calculate the disturbances for the LDEF geometry,
approximated by either a circular cylinder or a T-plate configuration, at
several locations and orientations. The impingement pressure used in PLIMP
was the modified newtonian formulation. A finer mesh size was used for the
cylinder representation than for the T-plate representation.

In a related study (Reference 10), the Skylab configuration approximated by
a collection of cylinders and plates was analyzed by the PLIMP program;
resulting forces and moments were compared for the same geometry approximated
by boxes and plates in the QLDP program (Reference 7) , as reported in
Reference 9.

4.2.1.4 Analysis Results

Table 4.2.1-1 summarizes performance data for impingement calculations by
PLIMP for the LDEF geometry. Cost data (not shown) indicated that running
the T-Plate approximation on PLIMP takes roughly the same execution time as
a cylinder representation with comparable mesh fineness. In a simpler pro-
gram (where geometry calculations would be relatively more significant), the
T-plate approximation might take a quarter to a half of the execution time
for the cylinder. However, we note from Table 4.2.1-1 that errors are gen-
erally large in both force and moment data for the T-plate approximation of
the LDEF geometry.

For convenience, we also repeat in Table 4.2.1-2 relevant results for Skylab
which were reported in Reference 10. Again, large differences in force and
moment data are noted between the two representations for the Skylab configu-
ration.

32

TABLE 4.2.1-1   PERFORMANCE VARIABLES FOR LDEF ·REPRESENTATION
BY CIRCULAR CYLINDER AND T-PLATES

TEST CASE				RAW PERFORMANCE DATA						SENSITIVITY[a]		
Number	d (ft)	ϕ (deg)	θ (deg)	Circular Cylinder			T-Plates			Force Errors		Moment
				F_x (lb)	F_y (lb)	M_z (lb-ft)	F_x (lb)	F_y (lb)	M_z (lb-ft)	Δ Mag (± %)	Δ Dir (± deg)	Error (± %)
1.	40.	60.	0.	1.753	0.309	-2.69	1.754	0.625	-4.272	4.61	9.62	58.81
2.	40.	60.	90.	1.862	0.040	-6.51	1.333	0.040	-4.843	28.40	0.49	25.61
3	60.	60.	0.	0.622	0.170	-0.92	0.622	0.261*	-1.222	4.61	7.48	32.83
4	60.	60.	90.	0.801	0.041	-1.94	0.627	0.041	-1.546	21.66	0.81	20.31
5	60.	60.	120.	0.829	0.478	-4.03	0.722	0.417	-3.266	12.87	0.04	18.96
6	100.	30.	0.	2.160	9.124	-27.64	2.10	8.88	-24.92	2.68	0.01	9.84

NOTES:

[a]With respect to the cylinder results

GEOMETRY :

33
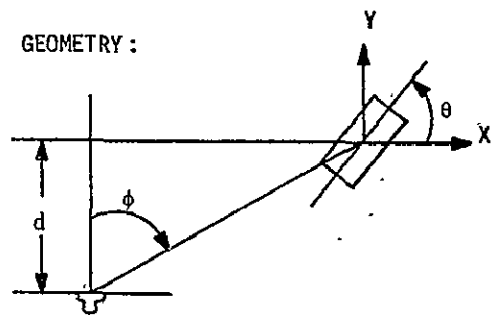
TABLE 4.2.1-2   PERFORMANCE DATA COMPARISON OF TOTAL SKYLAB DISTURBANCE DUE TO THREE
UP-FIRING JETS: QLDP VS. PLIMP (from Reference 10)

PROGRAM	RAW PERFORMANCE DATA								SENSITIVITY[a]			
	Fx (lb)	Fy (lb)	Fz (lb)	F-mag (lb)	Mx (lb-ft)	My (lb-ft)	Mz (lb-ft)	M-mag (lb-ft)	Force		Moment	
									ΔMag	ΔDir	ΔMag	ΔDir
QLDP	-25.69	28.89	-	38.66	-	-	-603.27	603.27	+64.9%	3.65°	+113.8%	13.97°
PLIMP	-16.49	16.64	-0.68	23.44	0	-68.11	-273.77	282.12	-	-	-	-

NOTES:

[a]with respect to PLIMP results

4.2.1.5 Preliminary Conclusions and Recommendations

Based on the above analysis and results, we conclude that, although a certain degree of simplification of payload configuration is required, a drastic simplification of geometry can induce significant errors in the impingement calculations. Therefore, a drastic simplification of subshape representation is not recommended in the plume impingement model.

4.2.2 Element Subdivision Mesh Size

4.2.2.1 The Question

How fine an element subdivision "mesh size" is required for ac-
ceptable accuracy? Should the mesh size be fixed or variable?

4.2.2.2 Tradeoff Factors/Considerations

Implementation: In the present study three different subshapes
(cylinder, circular plate and rectangular plate) are considered.
Each subshape is divided into a number of elements for impinge-
ment force and moment calculations. Figure 4.2.2-1 shows how
various subshapes are divided, using a single "fineness parameter",
n. (The PLIMP program (Section 3.2.4) actually allows for two
fineness parameters, n and m, for each subshape.) The fineness
parameter(s) would be provided by user input. On-line varia-
tion of mesh-size would be implemented by simple logic based on
distance and/or angle "breakpoints". For each individual element,
the program "quantizes" flowfield properties and impingement
angle at the centroid (properties and angle are assumed uniform
over the "elemental flat plate").

"Cost" Factors: Variation of n causes minor impact on computer
storage and complexity of the programming. Execution time var-
ies roughly as the square of n.

Performance Factors: Using a finer mesh size should increase
accuracy, by allowing more precise accounting for flowfield
gradients and variation of impingement angle over the object
surface. Figure 4.2.2-2 shows, qualitatively, the form of the
expected cost/performance effects of mesh-size variation for
fixed object geometry and orientation, neglecting roundoff:

- At a fixed distance, increasing fineness will reduce
  error.
- Increasing distance will reduce the fineness required
  to attain a given error level.

36
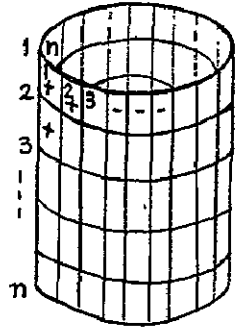
Cylinder
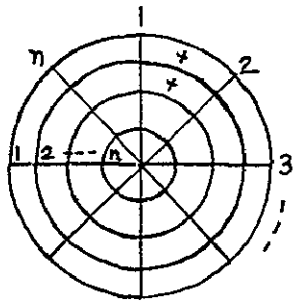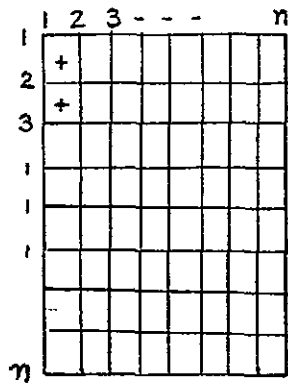
Circular Plate

Rectangular Plate

FIGURE 4.2.2-1   SUBDIVISION OF VARIOUS SHAPES;
CROSS INDICATES ELEMENT CENTROID
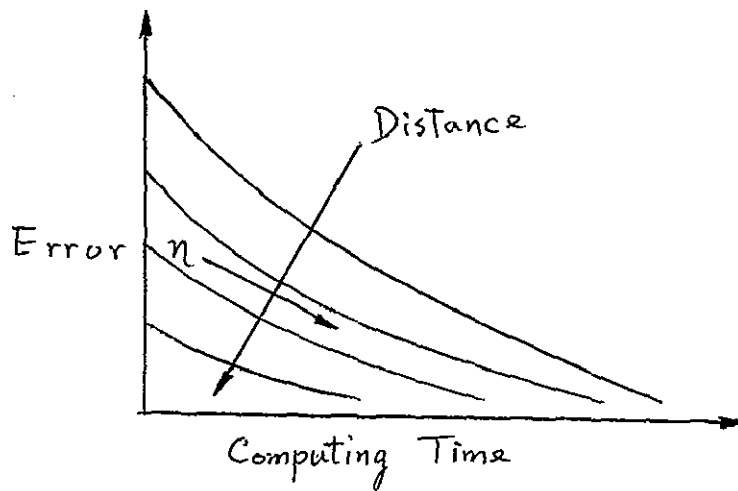
FIGURE 4.2.2-2 EXPECTED FORM OF COST/PERFORMANCE
VARIATION (FIXED GEOMETRY AND
ORIENTATION; ROUNDOFF NEGLECTED)

4.2.2.3 Analysis Approach

To evaluate effects of subdivision mesh size, a number of runs
of PLIMP were made, for both MMS/SMM and LDEF payloads (Sec-
tion 3.2.2) at various on-centerline distances and orientations.
Object shadowing computations (Section 4.2.3) were included
for all data runs. Impingement-pressure formulations used
(Section 4.4.1) were modified newtonian and oblique shock.

In addition, to investigate the property gradient effect on the
mesh size, a special case was also included with the LDEF being
displaced 30 degrees (57.74 ft) off the nozzle center line at
d = 100 ft. This position was chosen because the rate of change
of dynamic pressure with angle is maximal around 30 degrees.

Finally, three runs were made with a cylindrical payload 60 feet
in length and 15 feet in diameter, which is the maximum payload
size specified for the Orbiter. This cylindrical payload was placed
in the RCS plume 30 degrees from the centerline.

Three different mesh sizes were chosen for the cylinder surface
and its circular end plate, such that all the element dimensions
are comparable for a particular run. The modified newtonian
impingment formulation was used for these three runs.

4.2.2.4 Analysis Results

Table 4.2.2-1 provides case-by-case cost and performance data for
the LDEF and MMS/SMM runs. Errors were surprisingly small in many
cases. Execution time displays the expected trend. Data for the
60 X 15 payload, shown in Table 4.2.2-2, also show little variation
in accuracy as mesh fineness is reduced.

| TEST CASE				MESH SIZE	COST DATA		RAW PERFORMANCE DATA			SENSITIVITY[d]		
										Force Errors		Moment
Number[a]	d (ft)	φ (deg)	θ (deg)	nxm	Execution Time (Sec)	Time Ratio[d]	F_x (lb)	F_y (lb)	M_z (lb-ft)	Δ Mag (±%)	Δ Dir (± deg)	Error (±%)
M1	35	0	45[b]	60 x 60	364.6	-	74.05	46.62	-494 8	0	-	-
				30 x 30	89.8	0.25	74 23	46.50	-494.6	0.09	0.13	0.04
				15 x 15	25.9	0.07	74.44	46.44	-493.9	0.26	0 23	0.18
				8 x 8	7.2	0.02	74.49	46.23	-495.4	0.18	0.36	0.12
				4 x 4	2.8	0 01	70.95	49.36	-515 4	1.23	2.64	4.16
M2	50	0	20[c]	30 x 30	303.2	-	65.44	21.73	-117.8	-	-	-
				15 x 15	88 1	0 29	65.27	21.64	-119.5	0.28	0.03	1.44
				8 x 8	22.0	0.07	65.34	21.63	-119.0	0.17	0.05	1.01
				4 x 4	7.4	0.02	65.98	21.73	-114.3	0.75	0.14	2.97
M3	50	0	70[c]	30 x 30	287.5	-	21.34	2.74	-71.1	-	+	-
				15 x 15	63.6	0.22	20.99	2.88	-70.8	1.53	0.49	0.42
				8 x 8	22.2	0.08	19.65	3.28	-70.9	7.43	2.16	0.28
				4 x 4	6 8	0.02	19.08	3.47	-71.9	10.13	2.99	1.12
M4	100	0	20[c]	30 x 30	277.0	-	16.71	5.52	-17.1	-	-	-
				15 x 15	64.3	0.23	16.68	5.52	-17.2	0.17	0.03	0.58
				8 x 8	23.4	0.08	16.59	5.52	-17.6	0.68	0.12	2.92
				4 x 4	6 6	0.02	16.56	5 55	-17.9	0.74	0.25	4.67
L1	100	0	0[b]	30 x 30	35.2	-	21.37	0.0	0.0	-	-	-
				15 x 15	12.8	0.36	21.37	0.0	0.0	0.0	0.0	-
				8 x 8	4.8	0.14	21.35	0.0	0.0	0.09	0.0	-
				4 x 4	1.9	0.05	21.41	0.0	0.0	0.18	0.0	-
L2	100	0	20[b]	30 x 30	55.4	-	18.81	2.84	6.08	-	-	-
				15 x 15	16.2	0.29	18.81	2.84	6.03	0.0	0.0	0.82
				8 x 8	4.7	0.08	18.85	2.87	5.85	0.26	0.07	3.78
				4 x 4	2.1	0.04	18.70	2.90	5.63	0.53	0.23	7.40
L3	100	0	70[b]	30 x 30	40.3	-	27.71	-8.80	29.44	-	-	-
				15 x 15	10 3	0.26	27.69	-8.79	29.33	0.07	0.01	0.37
				8 x 8	3.6	0.09	27.60	-8.76	29.54	0.38	0.01	0.34
				4 x 4	1.8	0.05	27.60	-8.76	27.24	0.38	0.01	7.47
L4	100	0	90[b]	30 x 30	33.4	-	32.47	0.0	0.0	-	-	-
				15 x 15	8.8	0.26	32.55	0.0	0.0	0.20	0.0	-
				8 x 8	3.4	0.10	32.58	0.0	0.0	0.30	0.0	-
				4 x 4	1.7	0.05	32.20	0.0	0.0	0.80	0.0	-
L5	100	30	90[b]	30 x 30	33.1	-	9.124	2.16	27.64	-	-	-
				15 x 15	9.23	0.28	9.114	2.12	27.53	0.21	0.26	0.4
				8 x 8	3.33	0.101	9.08	2 12	27 13	0.56	0.18	1.9
				4 x 4	1.80	0.054	7.57	2.12	20.77	19.3	2.33	24.9

NOTES:
[a] M denotes MMS/SIMH, L denotes LDEF
[b] Modified newtonian impingement pressure
[c] Oblique shock impingement pressure
[d] With respect to the finest mesh size

GEOMETRY

40
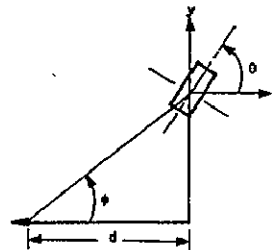
TABLE 4.2.2-2 COST & PERFORMANCE VARIABLES FOR A LARGE PAYLOAD
DUE TO ELEMENT SUBDIVISION MESH SIZE

	TEST CASE			MESH FINENESS		COST DATA		RAW PERFORMANCE DATA			SENSITIVITY[b]		
											Force Errors		Moment Error
Number	d (ft)	ϕ (deg)	θ (deg)	Cylinder nxm[a]	Disc nxm	Execution Time (sec)	Time Ratio[b]	F_x (lb)	F_y (lb)	M_z (lb-ft)	Δ Mag (±%)	Δ Dir (±deg)	(±%)
T1	100	30	90	30x60	30x7	79.40	-	21.531	1.762	239.20	-	-	-
T2	100	30	90	15x30	15x4	21.04	0.265	21.535	1.762	239.09	0.02	0.0009	0.046
T3	100	30	90	5x10	5x2	3.57	0.045	21.435	1.759	234.52	0.44	0.013	1.96

NOTES:

[a] n denotes angular subdivision;
m denotes linear subdivision

[b] with respect to the finest mesh size

GEOMETRY:
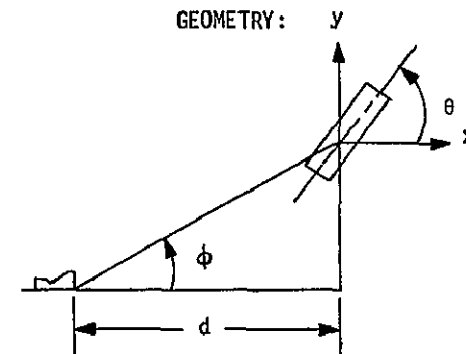
4.2.2.5 Preliminary Conclusions and Recommendations

Based upon the above analysis and results, it appears clear
that there is no need to use a fine subdivision mesh. Some-
thing of the order of 10 x 10 appears adequate in the "near
field", and probably 5 x 5 in the "far field". It appears
that the flow field property gradients do not contribute a
significant effect in choosing mesh size.

At a slight increase in program complexity, the mesh size
can be made variable with payload distance and/or orientation.
This feature is recommended for use with offline programs,
where average computing time is important; it is of minor value
in realtime simulations, where maximum computing time is most
important.

4.2.3 Object Shadowing

4.2.3.1 The Question

Do we require an object-shadowing capability in the plume imping-
ment model?

Figure 4.2.3-1 conceptually shows the types of object shadowing to
be considered: front/back and subshape/subshape. At least half
of every subshape is shadowed, since there is a "back side". Fur-
ther shadowing can occur with payloads which have multiple subshapes;
one subshape may block the "line-of-sight" from another subshape
to the thruster. This "optical" shadowing is the highest fidelity
implementation considered; no attempt is made to model the actual
flow around an object. If shadowing tests are not implemented in
the model, the flow is assumed to impinge on every element, regard-
less of position and orientation.

4.2.3.2 Tradeoff Factors/Considerations

To qualitatively assess "cost" and performance factors, first con-
sider how object shadowing would be implemented in the model.

Implementation: Each subshape is divided into elements as depicted
in Figure 4.2.3-1 (a); see Section 4.2.2. The outward normal of
each element, $\underline{n}$, is dotted onto the vector along the thruster line
of sight to that element, $\underline{\ell}$. If $\underline{\ell} \cdot \underline{n} <0$, the element is visible;
if $\underline{\ell} \cdot \underline{n} >0$, the element is on the back side and is invisible to
the plume.

The subshape/subshape shadowing determination is more complex,
as can be seen in Figure 4.2.3-2. The general methodology for
determining shadowing of a particular element is as follows:
1. Transform coordinates to write the equations of
   the subshape and line-of-sight in same axes.
2. Determine whether an intersection of the subshape
   and line-of-sight exists within the limits of the
   subshape.

43
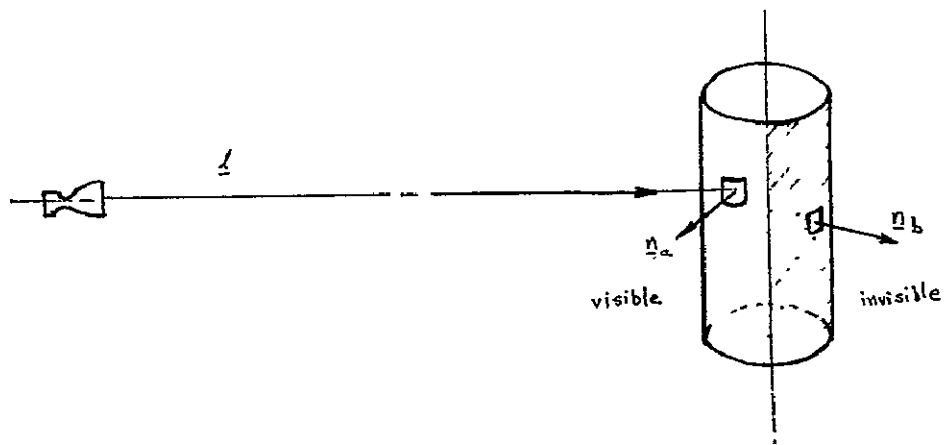
(a) Front/back Shadowing
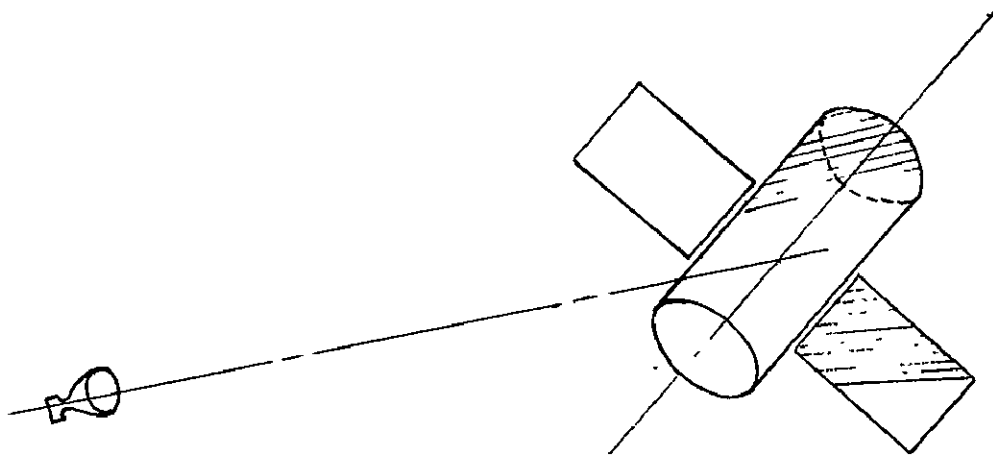
(b) Subshape/Subshape "Optical" Shadowing

Figure 4.2.3-1   Types of Object Shadowing Considered
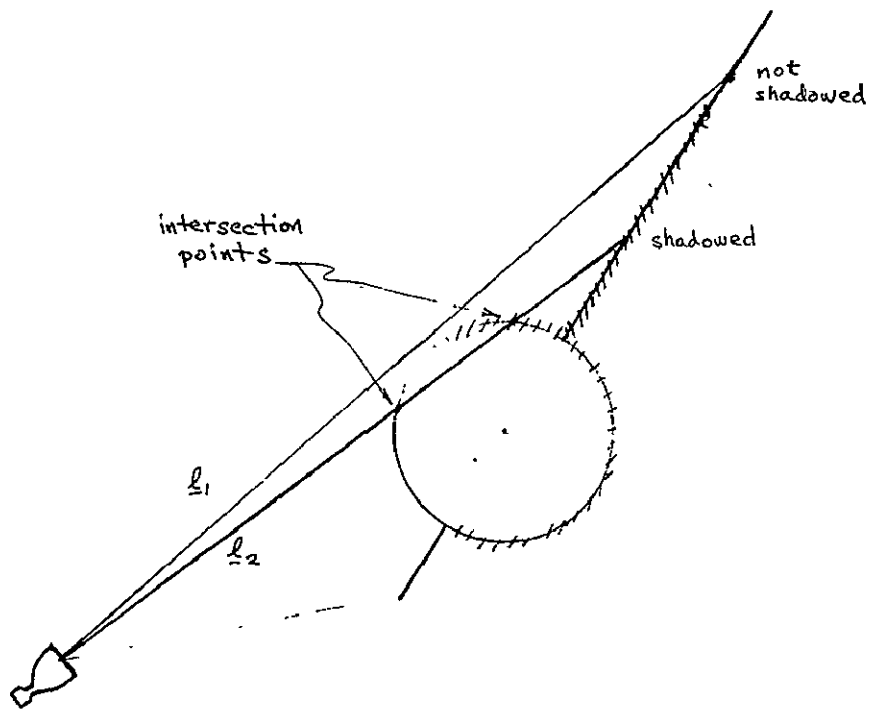
Figure 4.2.3-2 Subshape Shadowing Determination

3. If there is an intersection, determine whether it is
   "upstream" of the current element.

These calculations must be done for every element of every subshape.
(Note that a solid cylinder is represented as three subshapes: a
hollow cylindrical "tube" and two circular end plates.) Short
cuts may, however, be possible.

"Cost" Factors: The cost of the back side test is minor, since
the element position must always be expressed in thruster coordi-
nates to get local flow properties. The "cost" of subshape/sub-
shape shadowing depends partially upon logical complexity (different
form of equations for each type of subshape - e.g., cylinder,
circular and rectangular plates). There are also core requirements
for the additional equations and logic. The execution-time cost
may be positive or negative, since computations of intersection
equations (some of which may be quadratic) and coordinate trans-
formations must be added, but flow parameters, forces and moments
will not have to be determined for shadowed elements.

Performance Factors: Neglecting back side shadowing would obviously
cause unacceptable errors in the force and moment calculations.
Neglecting subshape/subshape shadowing will also obviously intro-
duce error into the force and moment computations—in general, in
both magnitude and direction. One can easily conceive of "path-
ological" cases for which neglecting subshape/subshape shadowing
reverses the sign of the computed moment; see Figure 4.2.3-3.

4.2.3.3 Analysis Approach

The following steps were taken to evaluate tradeoff factors for
object shadowing: PLIMP runs (Section 3.2.4) were made at various
on-centerline distances and orientations with respect to a single
thruster, using MMS-SMM geometry data as defined in Section 3.2.2;
see Figure 4.2.3-4 for a definition of coordinates. Each run was
made with and without the subshape/subshape shadowing option enabled

46
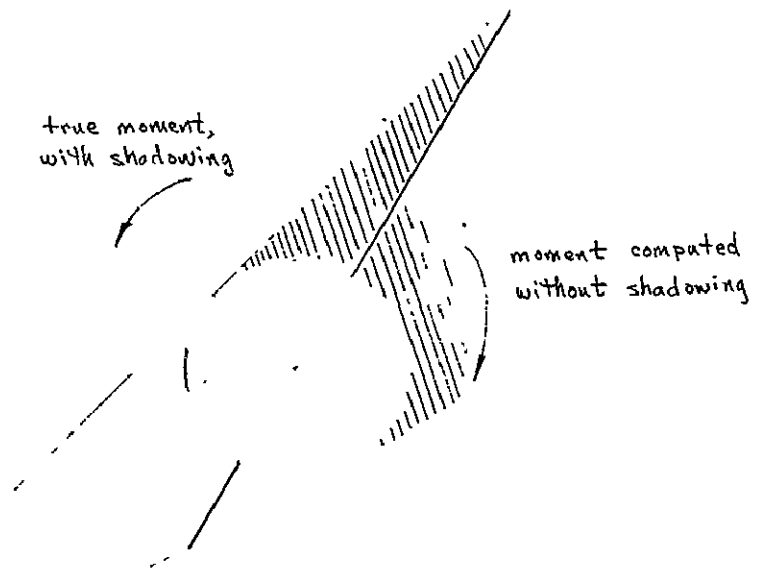
Figure 4.2.3-3 "Pathological" Case Showing Sign Reversal of Moment
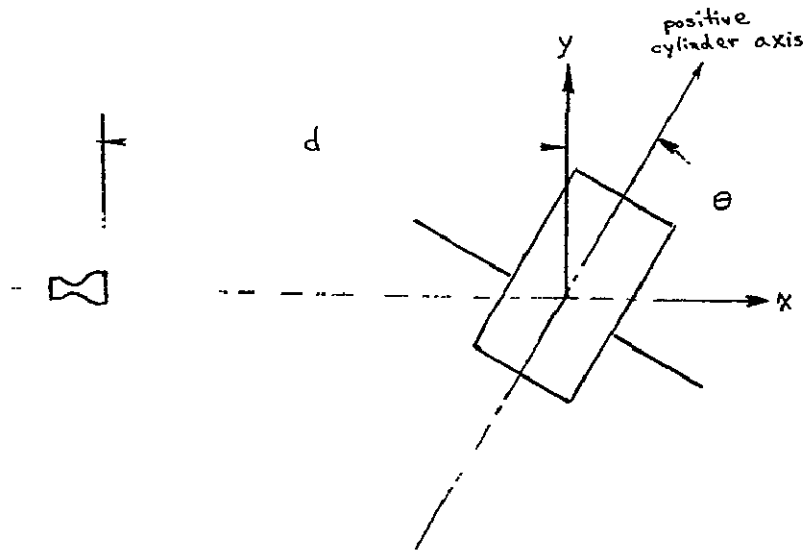
Figure 4.2.3-4   Coordinates Illustration

(the front/back computation is not optional). Forces, moments, and execution time with and without shadowing were compared for each test case. The inviscid-flow flowfield used for all runs was provided by MOC (Section 3.2.3). All runs were made with a constant mesh size of 30x30 (see Section 4.2.2); the impingement formulation was sometimes modified newtonian and sometimes tangent wedge/oblique shock (see Section 4.4.1).

4.2.3.4 Analysis Results

No comparative results of the effect of back side shadowing are provided, since this is not an optional feature in PLIMP.

Table 4.2.3-1 provides case-by-case performance and "cost" data for the runs made to analyze subshape/subshape shadowing. Cost data is in terms of Univac 1108 Central Arithmetic Unit (CAU) execution time.

The "fixed cost" (additional storage required) to implement subshape/subshape shadowing has been roughly estimated by identifying those PLIMP routines which are used only for this computation, adding their core storage and converting to decimal. The estimated total storage required for subshape/subshape shadowing in PLIMP is approximately 800 1108 words. (Our implementation may not be the same as that in PLIMP.)

4.2.3.5 Preliminary Conclusions and Recommendations

Based upon the above analysis we have come to the following conclusions:

- Significant errors in force and moment determination may be expected if shadowing capability is not included in the model.
- Shadowing routines will require additional core, but will actually save computer time at some payload orientations.

Therefore, we recommend that object shadowing, both back side and subshape/subshape, be implemented in the plume impingement model.

48

TABLE 4.2.3-1 COST AND PERFORMANCE VARIABLES FOR SUBSHAPE/SUBSHAPE SHADOWING

TEST CASE			"COST" DATA			RAW PERFORMANCE DATA						SENSITIVITY [c]		
No	d (ft)	θ (deg)	Execution Time (sec)		Time Ratio $\left(\frac{With}{Wo}\right)$	Without Shadowing			With Shadowing			Force Errors		Moment Error
			Without Shadowing	With Shadowing		F_x (lb)	F_y (lb)	M_z (lb-ft)	F_x (lb)	F_y (lb)	M_z (lb-ft)	ΔMag (+%)	ΔDir (± deg)	(+%)
1	35	45[a]	101.1	89.8	0.80	93.17	50.20	-414.8	74.23	46.50	-494.6	20.8	3.75	16.13
2	50	45[a]	63.3	58.7	0.93	44.57	23.01	-152.6	34.72	21.77	-184.5	22.4	4.78	17.29
3	50	70[b]	400.4	287.5	0.72	30.07	1.93	-69.0	21.34	2.74	-71.1	40.0	3.64	2.95
4	100	20[a]	78.9	79.5	1.01	17.55	5.31	-14.9	16.77	5.35	-16.8	4.1	0.89	11.31
5	100	20[b]	323.8	277.0	0.86	17.46	5.54	-14.7	16.71	5.52	-17.1	4.1	0.68	14.04
6	100	45[a]	69.2	65.3	0.94	10.78	5.23	-20.3	8.14	5.27	-25.2	23.6	7.04	19.44
7	100	70[a]	71.5	69.6	0.97	7.41	0.77	-11.7	5.50	0.54	-16.3	34.8	0.33	28.22
8	100	70[b]	427.6	314.6	0.74	7.19	0.21	-11.1	5.35	0.14	-14.2	34.4	2.92	21.83

Notes:

a Modified Newtonian Impingement Pressure
b Oblique Shock Impingement Pressure
c Shadowing is considered the correct result

Geometry:
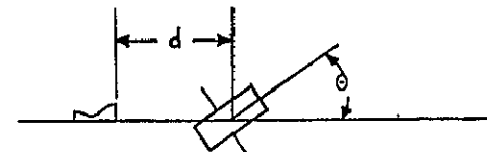
4.3 Plume Flowfield Modeling Approaches

This section deals with alternative formulations of the RCS engine plume flow-field module, FLOFLD. The FLOFLD module provides the plume thermodynamic and flow properties necessary to calculate the plume impingement pressure effects on the payload. The data provided by FLOFLD are derived from a standard thermo-chemical/method-of-characteristics generated plume flowfield which is discussed below.

Since the Orbiter RCS engines are operational at orbital altitudes (above 100 nautical miles), the plume will be highly expanded. As the plume expands, the density decreases, and therefore the intermolecular collisions decrease and the molecular mean free path increases. Eventually, the intermolecular collisions become so few that the gas no longer obeys the laws of continuum fluid mechanics during the plume expansion process. At the molecular level, a gas has three energy modes: translation, rotation, and vibration. In the continuum regime, equilibrium is maintained among these modes; however, this may not be true in the low density region of the plume. When the gas undergoes a sudden change in translational temperature, several collisions are required to bring the rotational temperature into equilibrium, and several thousand collisions are required to bring the vibrational temperature into equilibrium. If the number of collisions is not great enough to keep these energy modes in equilibrium, the law of · equipartition of energy no longer holds. Therefore, each energy mode "freezes" at a different location. The temperature associated with that particular energy mode is then frozen, and the specific heat ratio and gas constant are adjusted to account for the loss of the degrees of freedom associated with that particular energy mode. Once all modes of energy have frozen, the flow is considered free molecular.

When the continuum flow is source-like, i.e., high Mach numbers (low Mach angles) the streamlines are nearly straight. If transition to noncontinuum flow begins in the source-like flow regime, the freezing of each energy mode at its particular location has a less pronounced effect on the plume flowfield. Therefore, in the plume definition presented here, only the transition to free molecular flow was defined, i.e., all energy modes have frozen. The flow prior to transition was assumed continuum, and the thermodynamic and flow properties

50

were defined using continuum gas dynamics. After transition to free molecular flow, free molecular flow techniques were used to characterize the plume flowfield.

The degree of rarefaction in the plume flow depends on the ratio of the molecular mean free path in the plume, λ_∞, and a characteristic dimension used to characterize the transition mechanism. The characteristic dimension used here was chosen as the nozzle exit radius. The dimensionless ratio is the Knudsen number in the plume flowfield, K_{np}. The plume Knudsen number can be expressed in terms of familiar parameters of fluid mechanics. From the kinetic theory of gases, the coefficient of viscosity is related to the mean free path (References 11 and 12):

$$\mu_\infty = (1/2)\lambda_\infty \rho_\infty V_m \qquad (4.3\text{-}1)$$

where

μ_∞ = plume coefficient of viscosity

λ_∞ = plume mean free path

ρ_∞ = plume density

V_m = plume average molecular velocity

The average plume molecular velocity can be related to the plume speed of sound as follows. The speed of sound is given by:

$$a_\infty = \sqrt{(\gamma_\infty \, P_\infty)/\rho_\infty} \qquad (4.3\text{-}2)$$

where P_∞ is the plume static pressure and γ_∞ is the plume specific heat ratio. The plume root-mean-square velocity of the molecules is given by (Reference 12):

$$V_{rms} = \sqrt{3P_\infty/\rho_\infty} \qquad (4.3\text{-}3)$$

The relation between root-mean-square velocity and average velocity (References 12 and 13) is:

$$V_m = \sqrt{8/3\ \pi}\ V_{rms} \qquad (4.3\text{-}4)$$

Combining (4.3-2), (4.3-3), and 4.3-4):

$$V_m = \sqrt{8/\gamma_\infty\ \pi}\ a_\infty \qquad (4.3\text{-}5)$$

Substituting (4.3-5) into (4.3-1), dividing by L_p (nozzle exit radius) and multiplying numerator and denominator by the plume flow velocity U_∞:

$$K_{np} = \frac{\lambda_\infty}{L_p} = \sqrt{\frac{\gamma_\infty \pi}{2}}\ \frac{M_\infty}{R_e} \qquad (4.3\text{-}6)$$

where

$$R_e = \frac{\rho_\infty U_\infty L_p}{\mu_\infty} \qquad \text{and} \quad M_\infty = \frac{U_\infty}{a_\infty}$$

This is the plume Knudsen number in terms of familiar parameters of fluid mechanics.

The calculation of the coefficient of viscosity in a reacting multispecies flow system, such as exists in an exhaust plume, is quite complex. The coefficient of viscosity for species "i", (Reference 14) is:

$$\mu_i = 2.67\ X\ 10^{-5}\ \frac{\sqrt{M_i\ T_\infty}}{\sigma_i\ _\Omega\ (2,2)^*} \qquad (4.3\text{-}7)$$

where
M_i = molecular weight of species "i"
T_∞ = plume temperature
σ_i = collision diameter of species "i"
$\Omega^{(2,2)*}$ = binary collision integral

52

For a mixture of gases with "j" components:

$$\mu_\infty = \sum_{i=1}^{j} \mu_i \left[1 + \sum_{\substack{k=1 \\ k \neq i}}^{j} G_{ik} \frac{X_k}{X_i} \right]^{-1}$$

(4.3-8)

where

X_i = mole fraction of species "i"

and G_{ik} is given by:

$$G_{ik} = \frac{\left[1 + \sqrt{\mu_i/\mu_k} \, (M_k/M_i)^{1/4} \right]^2}{2.83 \sqrt{1 + M_i/M_k}}$$

(4.3-9)

The coefficient of viscosity for a reacting multispecies flow system can be calculated using the TRANS 72 computer program (Reference 15). This program was used to obtain the plume coefficient of viscosity used in Equation 4.3-6 to define the plume Knudsen number.

The criteria used here to define transition to free molecular flow in the plume is that suggested in Reference 11:

$$\frac{M}{Re} > 3$$

(4.3-10)

For the RCS plume, this indicates free molecular flow is reached when the mean free path is approximately 4.4 times the nozzle exit radius. This is the value used to determine transition to free molecular flow in the RCS plume.

Another important aspect which must be considered when defining the thermo-dynamic and flow properties in the plume is how the nozzle boundary layer

53

affects the plume flowfield. The reduced velocity in the boundary layer perturbs the plume expansion at the nozzle lip. This perturbation is quite acute at high altitudes, which is the case here. This effect on the plume expansion was accounted for using a turbulent boundary layer analysis starting at the nozzle throat, Reference 14.

Real gas effects in the exhaust plume were accounted for assuming equilibrium chemical reactions throughout the flowfield utilizing a one-dimensional equilibrium chemical kinetics computer program (ODE) discussed in Section 3.2.3. The thermodynamic properties and species concentrations for the RCS propellant system (MMH/N_2O_4) are then used with a method-of-characteristics (MOC) computer program (discussed in Section 3.2.2) to define the plume. The MOC is a mathematical technique which defines the plume flowfield along left-running characteristics, and stores the data in a cartesian coordinate system located at the nozzle exit.

Figures 4.3-1 through 4.3-6 present Mach number, temperature, density, and dynamic pressure contours in the standard RCS engine plume both in the near field (up to 200 feet from the nozzle exit) and in the far field (up to 1000 feet from the exit). The operating and geometric characteristics of the RCS engine are given in Section 3.2.1.

The transition from continuum to free molecular flow and the reflected shock are also shown in the figures. After free molecular flow has been reached, the mass flow streamlines remain straight and the temperature, velocity, and Mach numbers along these streamlines remain frozen at the values attained at the transition point. The labelling of each mass flow streamline represents the percent of the total mass flow in the plume which falls below that stream-line. Since the other thermodynamic and flow properties in the plume have frozen at the transition point and the streamlines are straight, the density simply changes as the inverse of the cross-sectional area ($1/r^2$ law).

This plume definition will be used to calculate the plume-induced pressure effects on the payloads. Since the plume flowfield data generated by the

method of characteristics are at random locations, an extensive search and interpolation scheme is required when flowfield information is needed at a particular location in the plume. It would therefore be very advantageous to be able to represent the plume using some type of closed-form technique which would make data retrieval fast and efficient. The possibility of using source flow equations or a mathematical curve fit technique to represent the standard data is discussed in Section 4.3.1.

Many of the RCS engines whose plumes may affect the payloads have scarfed nozzles. The effect on the plume due to nozzle scarfing is discussed in Section 4.3.2.

The engines may operate over a large range of altitudes (100 to 350 nautical miles). Effects of the ambient atmosphere in this altitude range are discussed in Section 4.3.3.

For certain maneuvers, engines may operate simultaneously. Plume characterization for simultaneous engine operation is discussed in Section 4.3.4.
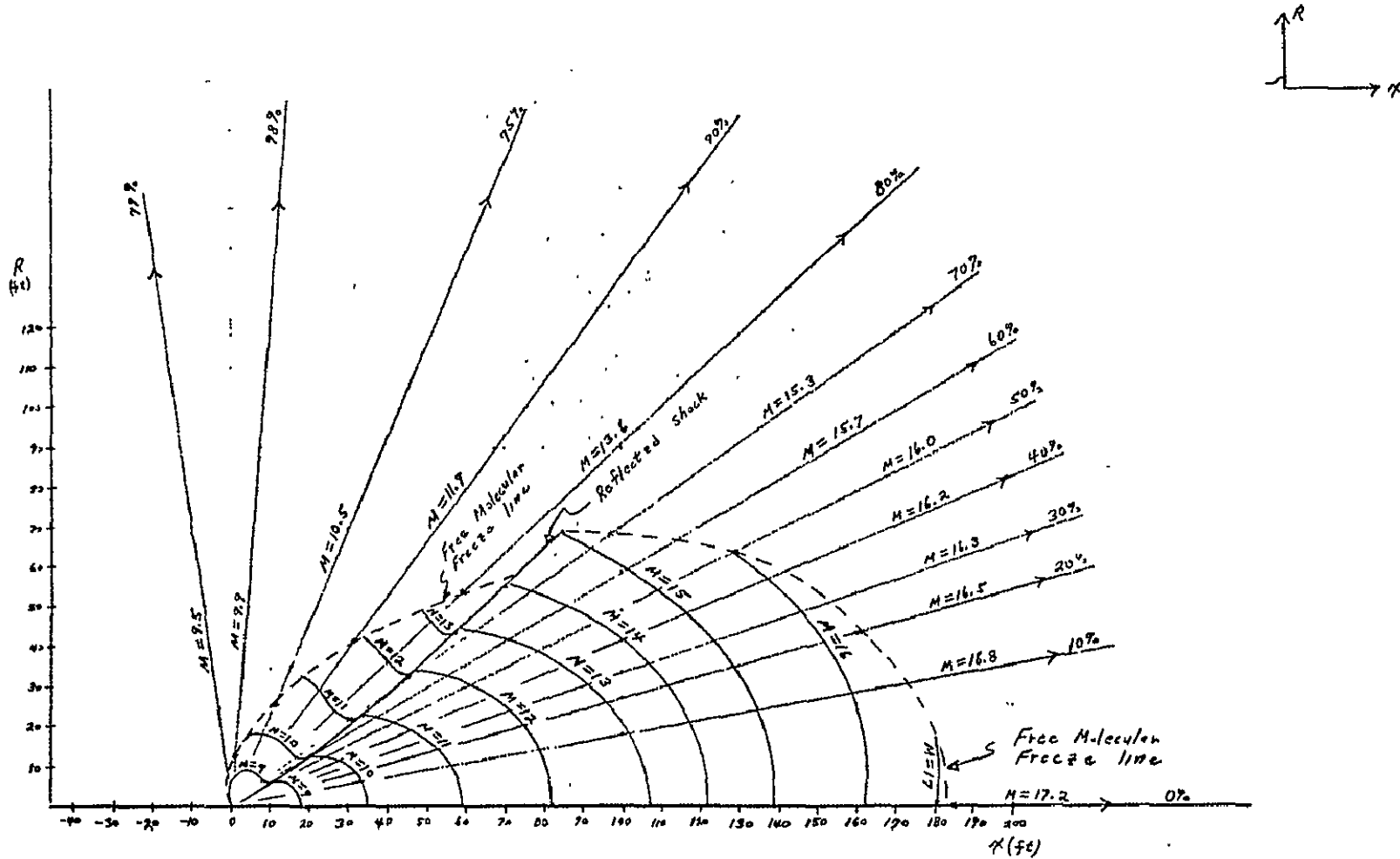
FIGURE 4.3-7   .. Mach Number Contours in the RCS Engine Plume (continuum and free molecular regimes)

56
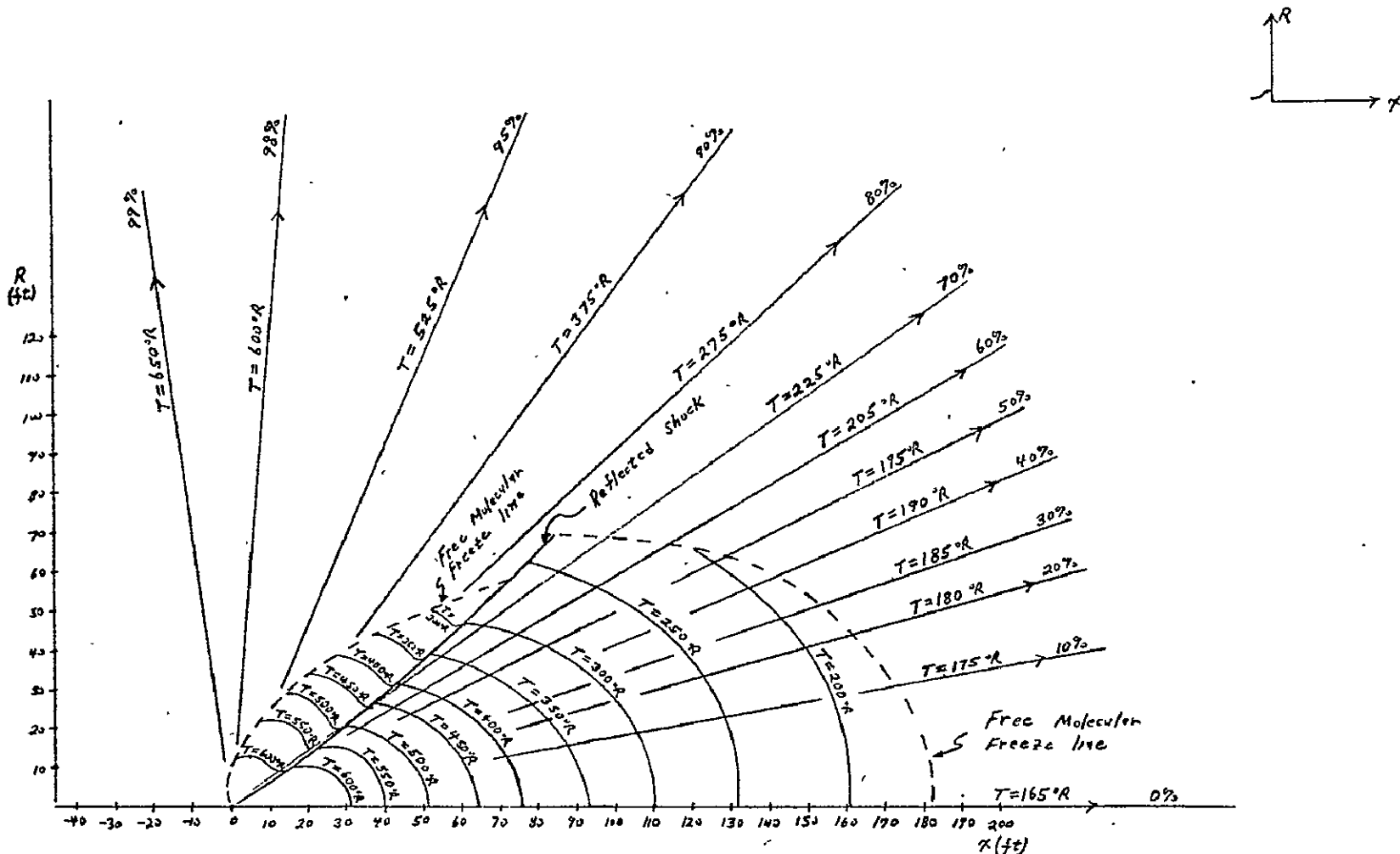
FIGURE 4.3-2 . Temperature (°R) Contours in the RCS Engine Plume (continuum and free molecular regimes)

57
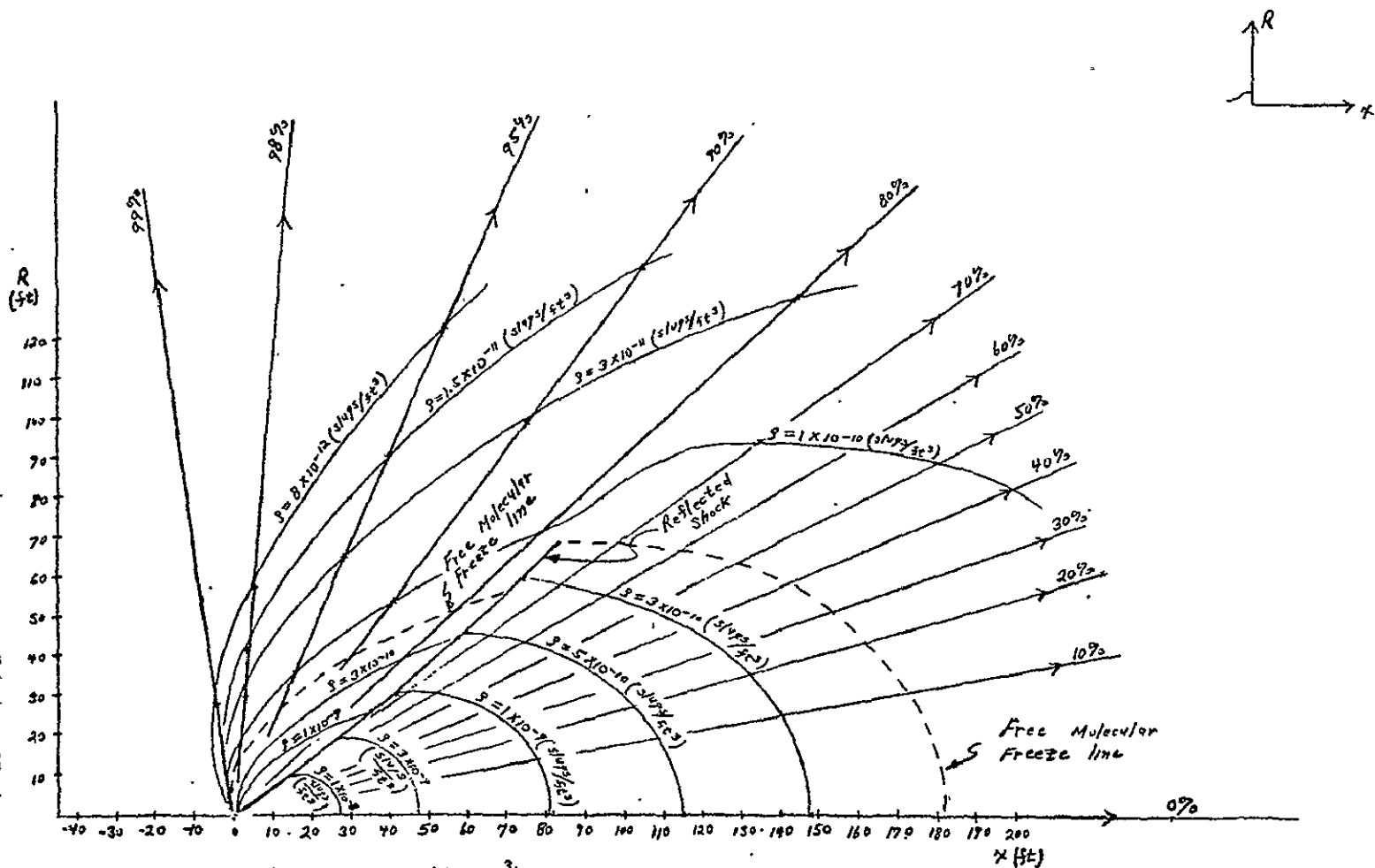
FIGURE 4.3-3.. Density (slugs/ft³) Contours in the RCS Engine Plume (continuum and free molecular regimes)

58
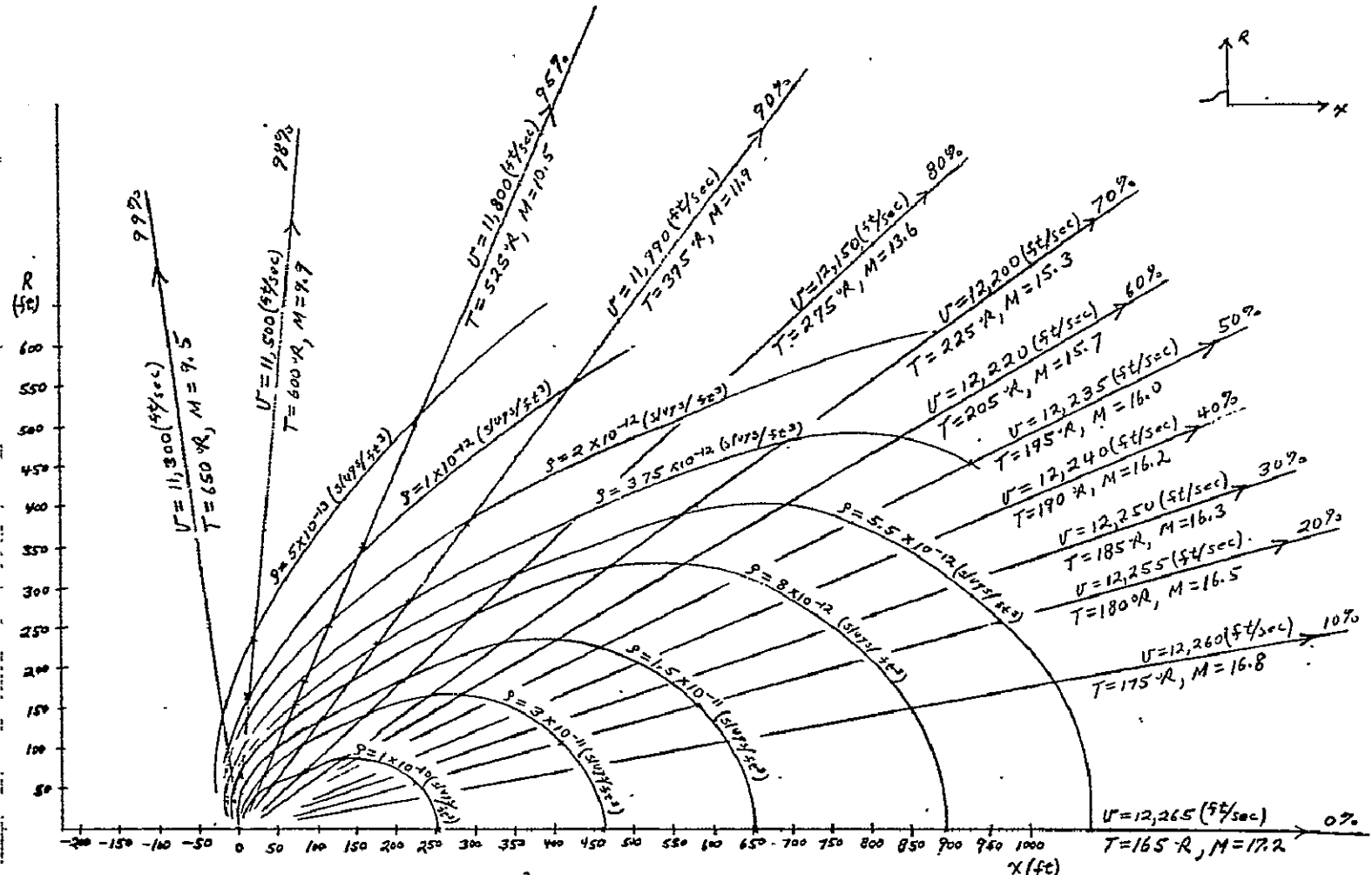
FIGURE.4.3-4 Density (slugs/ft³) Contours and Velocity (ft/sec) in the RCS Engine Plume (free molecular regime)
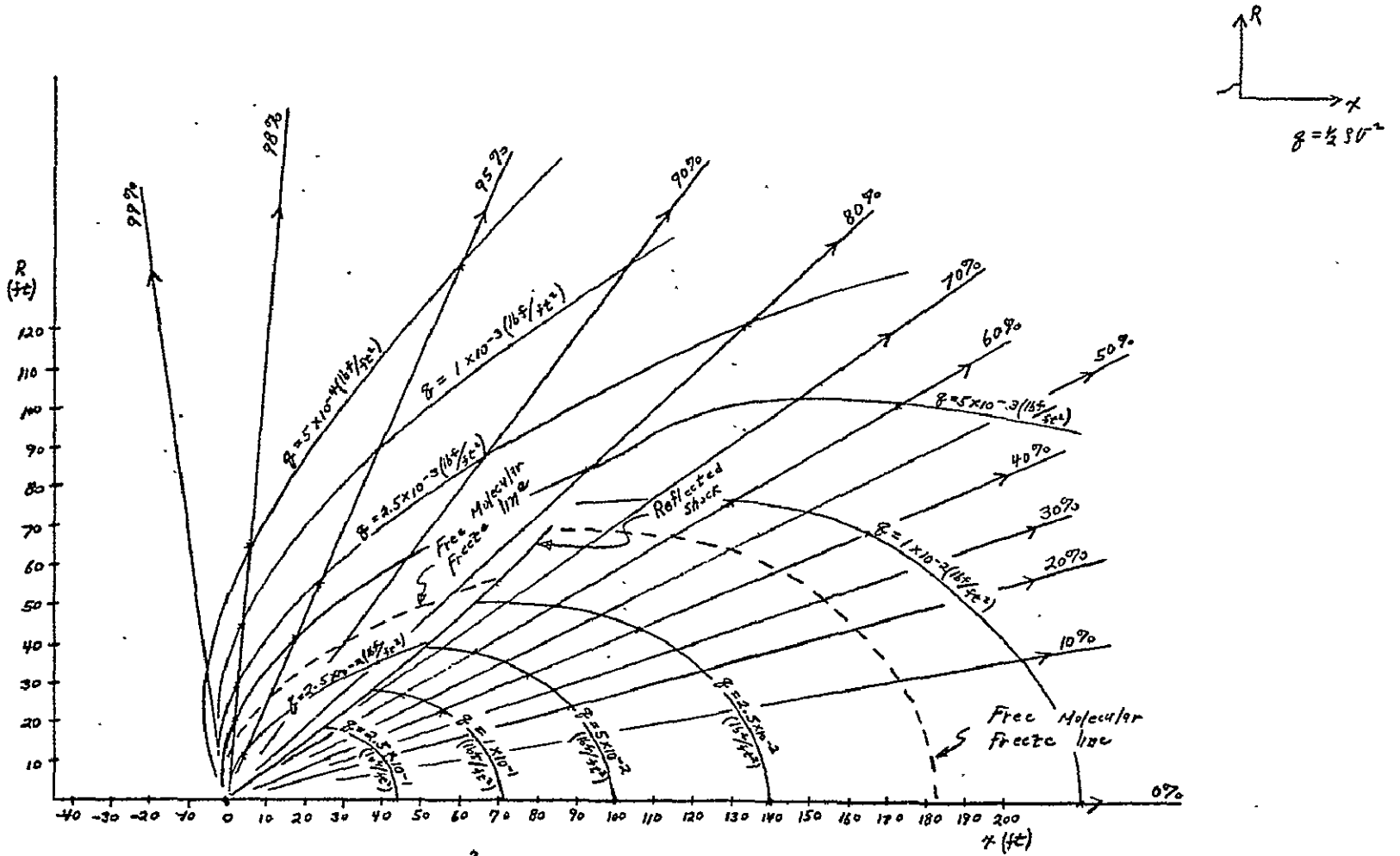
FIGURE 4.3-5. Dynamic Pressure (1bf/ft^2) Contours in the RCS Engine Plume (Continuum and free Molecular regimes)
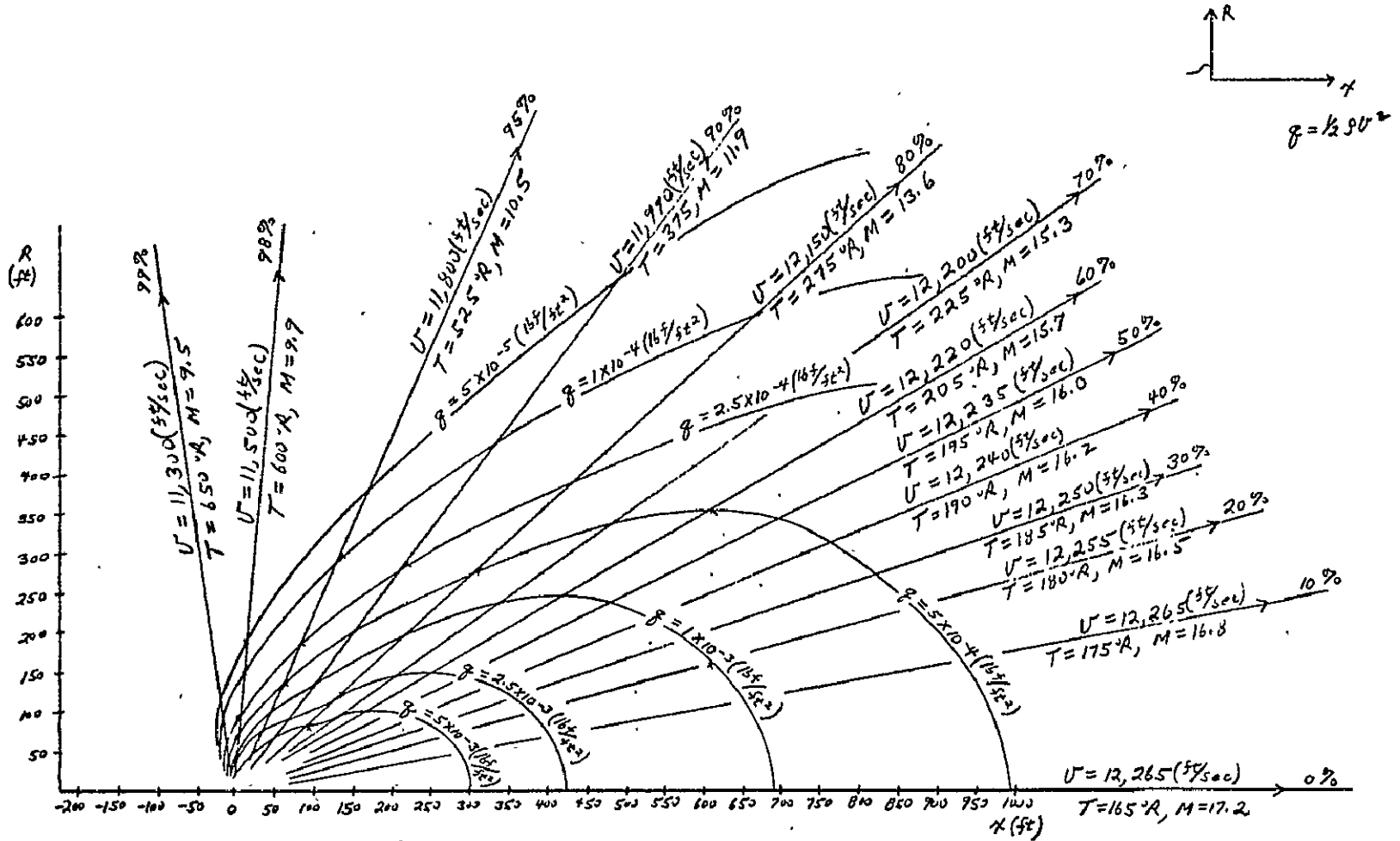
FIGURE.4..3÷6 Dynamic Pressure (lbf/ft^2) Contours in the RCS Engine Plume (free Molecular regime)

61

4.3.1 Use of Source-Flow Approximations

4.3.1.1 The Question

What is the best method of representing the high-fidelity plume flowfield
and obtaining data at desired points?

The alternatives are:

● Use some type of source flow equations to represent the MDAC-West standard
plume data

● Use the MDAC-West standard flowfield data described in Section 4.3, either
in raw tabular form, or reduced by conventional curve/surface-fit tech-
niques.

Various "source flow" and source flow-like models have been considered for
representing plume flowfields. These models, described in some detail be-
low, are as follows:

● Simple source flow (entire flowfield)

● Source flow with boundary-layer correction (entire flowfield)

● Source-flow forms with "curve-fit" constants and corrections
(entire flowfield)

● Patched source flow (flowfield subdivided into "regions")

Simple Source Flow: The source flow model of a rocket plume (Reference 16)
is derived from two basic assumptions:

● At any fixed angle from the thruster centerline, the gas acts as though
emanating from a point source; thus, all streamlines are straight, and
density along each streamline obeys an inverse-square law.

● The thermodynamic parameter (ratio of specific heats) of the gas, γ, is
constant over the field.

Choosing an empirical functional form for the angular dependence (Reference
17), the dynamic pressure at any point (r,θ) can then be calculated by:

$$q(r,\theta) = \frac{A}{r^2} \cos^B(C\theta)$$

(4.3.1-1)

where A, B, and C are constants determined by the thruster parameters and
the choice of γ. Similar equations can be developed for density, Mach
number, and other flow properties.

Source Flow With Boundary Layer Correction: For a finite boundary layer thickness, the simple source flow analysis can be modified to include an exponential boundary layer correction term in the calculation of dynamic pressure at high angles from the plume centerline (Reference 17):

$$q(r,\theta) = \frac{A}{r^2} f(\theta) \qquad f(\theta) = \begin{cases} \cos^B(c\theta), & \theta \le \theta_0 \\ \cos^B(c\theta_0)\exp[-\beta(\theta-\theta_0)] & \theta > \theta_0 \end{cases} \qquad (4.3.1\text{-}2)$$

Here β and θ_0 are additional constants which depend on the boundary layer thickness and nozzle exit radius.

Source Flow With "Curve-Fit" Constants: This technique predicts dynamic pressures using the same form as Equation 4.3.1-2 ; however, the five constants are now considered mathematical "curve fitting" parameters which are calculated by curve fitting the standard data.

MPAD Mathematical Curve Fit Model: MPAD has developed a similar method of calculating dynamic pressures based on curve fits to standard data. The dynamic pressure, q, is calculated as:

$$q = \tfrac{1}{2}\rho V^2 \quad \text{and}$$

if $\theta < 38.6°$:
$$\begin{cases} \rho = \dfrac{6.356 \times 10^{-6}}{r^2} \cos^{5.1}\left(\dfrac{\pi}{2} \dfrac{\theta°}{98.6}\right) \\ V = 11400 + 865\cos\theta \end{cases}$$

if $\theta \ge 38.6°$
$$\begin{cases} \rho = \dfrac{1.40679 \times 10^{-6}}{r^2} \exp\left(-7.564 \times 10^{-2}[\theta - 38.6°]\right) \\ V = 11400 + 865\cos\theta \end{cases}$$

(4.3.1-3)

if $\rho > 1.91885 \times 10^{-10}$
$$\begin{cases} \rho = \dfrac{6.5712 \times 10^{-6}}{r^2} \cos^{5.1}\left(\dfrac{\pi}{2} \dfrac{\theta}{98.6}\right) \\ V = 12600 - .0012\left(abs[110-r]\right)^3 \end{cases}$$

63

Patched Source Flow Equations: With this technique, we again use Equation 4.3.1-2 with "curve-fit" parameters. However, the constants are determined independently in various "regions" of the plume, rather than for the entire plume at once. (Of course, fitting the entire plume can be considered a special case of this procedure.) These regions are then "patched" together to cover the entire flowfield, generating a table of source-flow parameters as functions of thruster coordinates.

Note that this technique may cause non-physical discontinuities in flowfield properties at the region boundaries. It may be desirable to use overlapping patches and/or some type of averaging scheme.

Manipulation of Standard Data: MDAC-West standard data can be stored in on-line tables; search and interpolation techniques can then be used to find flowfield properties at given thruster coordinates. Another approach is to fit the standard data with conventional mathematical curves or surfaces--e.g., polynomials or splines.

4.3.1.2   Tradeoff Factors/Considerations

Implementation: Implementation of the entire-field source flow and source flow-like techniques is simple and straightforward. Implementation of the patched source flow technique will require searching a small data block in the program. Using the technique involving manipulation of standard data will require complex search and interpolation schemes and logic in the program.

In implementing a flowfield model for plume impingement calculations, one must include a streamline model in order to calculate impingement angles. For the high-fidelity streamlines shown in Section 4.3, the common assumption of radial streamlines appears justified for all distances from the nozzle large compared to the nozzle exit diameter.

"Cost" Factors: In terms of complexity, storage, and execution time, the simple source flow, source flow with boundary layer correction, and source flow with curve fit constants are the easiest and fastest to use, since

64

they require at most one comparison (θ vs. θ_0) and one calculation. The MPAD model and the patched source flow are also simple, and have fast execution times. Direct use of the MDAC-W standard data will require very large storage areas, and considerable complexity in manipulation of data. Storage and execution time requirements for the use of conventional curve fits to the standard data are difficult to estimate at this time. Execution time is expected to be proportional to the complexity, with one special caution: if the available main-storage area were too small to hold all the standard data, the need to use "overlay" techniques would increase execution time dramatically.

Performance Factors: Since the expected end use of this model will include analysis of "R-bar" and "V-bar" approaches (Reference 18), the plume flow-field must be accurately modelled in the highly rarified regions of the plume at large angles from the centerline, even at the expense of storage and execution time. Accuracy requirements are of fundamental importance in recommending a plume flowfield technique. Those flowfield models which satisfy certain accuracy criteria will then be considered for minimum storage and execution time.

4.3.1.3 Analysis Approach

To calculate the theoretical constants in a source-flow model, a value must be chosen for γ; all other parameters required are engine parameters (e.g., chamber pressure). For the simple source flow, γ must be a constant; we use $\gamma = 1.236$, as suggested in Reference 19. Actually, γ varies in the plume. (In regions of low chemical activity, γ is basically a function of gas temperature.) Therefore, it is important to consider the sensitivity of the source-flow results to the value of γ.

The constants in Equation 4.3.1-1 are all functions of γ. Computing these constants for various γ's allows one to plot dynamic pressure contours using simple source flow analysis. Figure 4.3.1-1 shows two example dynamic pressure contours for various γ's. Qualitatively, we see that the value of γ can significantly affect the pressure contours.

To get more quantitative results, the radial dependence in Equation 4.3.1-1

65

Legend:

A $\gamma = 1.20$ E $\gamma = 1.28$
B $\gamma = 1.22$ F $\gamma = 1.30$
C $\gamma = 1.236$ G $\gamma = 1.32$
D $\gamma = 1.26$ H $\gamma = 1.34$

99
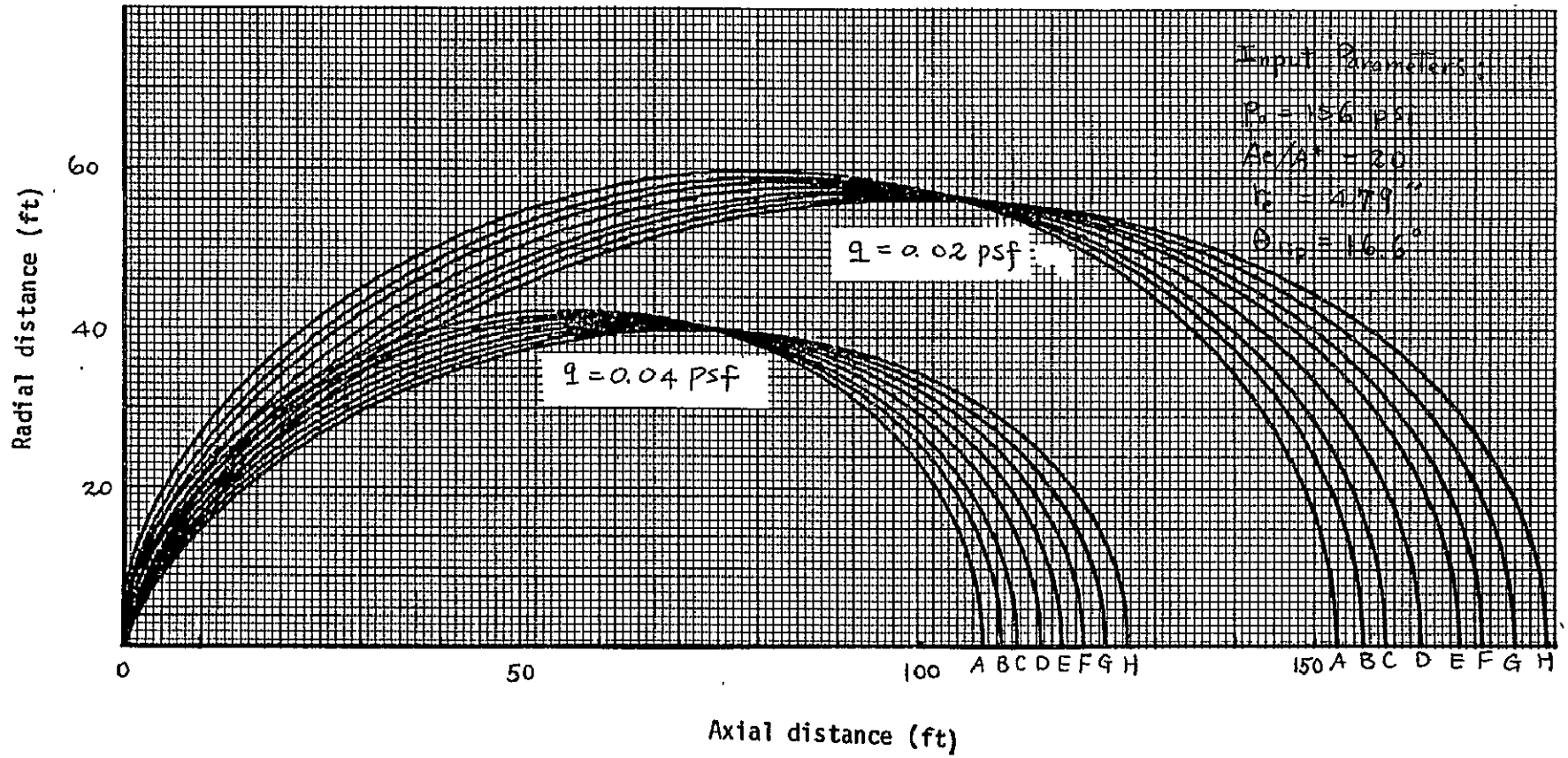
FIGURE 4.3.1-1   SENSITIVITY OF DYNAMIC PRESSURE CONTOURS TO VALUE OF THERMODYNAMIC   PARAMETER (γ)

. is eliminated by plotting qr^2 as a function of γ for various values of streamline angle, θ, as shown in Figure 4.3.1-2. Since the plots are roughly linear for a given θ, we see that the sensitivity of the dynamic pressure to γ is constant for a given θ. On the centerline ($\theta = 0$) a 1% change in γ gives a 3% change in dynamic pressure; at $\theta = 60^o$, a 1% change in γ gives a 15% change in dynamic pressure. Therefore, the dynamic pressure contours generated using source flow analysis are very sensitive to γ.

The various methods for generating flowfields described in Section 4.3.1.1 were used to determine dynamic pressures. The results were compared to MDAC-W standard dynamic pressure data.

Two sets of comparisons were made to the MDAC-W data. The first comparison is qualitative, and consists of overlaying dynamic pressure contours. The second comparison is a quantitative analysis of radial and angular slices of dynamic pressure. In investigating the patched source flow technique, a few representative sample regions were chosen for evaluation.

4.3.1.4 Analysis Results

Constants used in the five techniques are given in Table 4.3.1-1. Dynamic pressure contour overlays for the various techniques are shown in Figures 4.3.1-3 through -7; in each figure, (a) is the near-field analysis, (b) is the far field. Our data indicate that a source flow model must include a boundary layer correction in order to predict high-angle pressures accurately.

The comparisons to MDAC-W dynamic pressure data along radial and angular slices are shown in Figures 4.3.1-8 through 4.3.1-12. We believe the re-plotted MDAC-W data to be accurate within ±2 feet. This random plotting error may be significant at high angles, where the pressure gradient is steep. (To generate actual model data, we would use the standard data directly, in digital form, thus eliminating such plotting errors.)

The simple source flow model appears good at low angles, with typically 10% error, but fails at high angles. The technique using source flow with a boundary layer correction gives better agreement (at least in the form of the contours) at large angles, but errors in this region are still large.

67
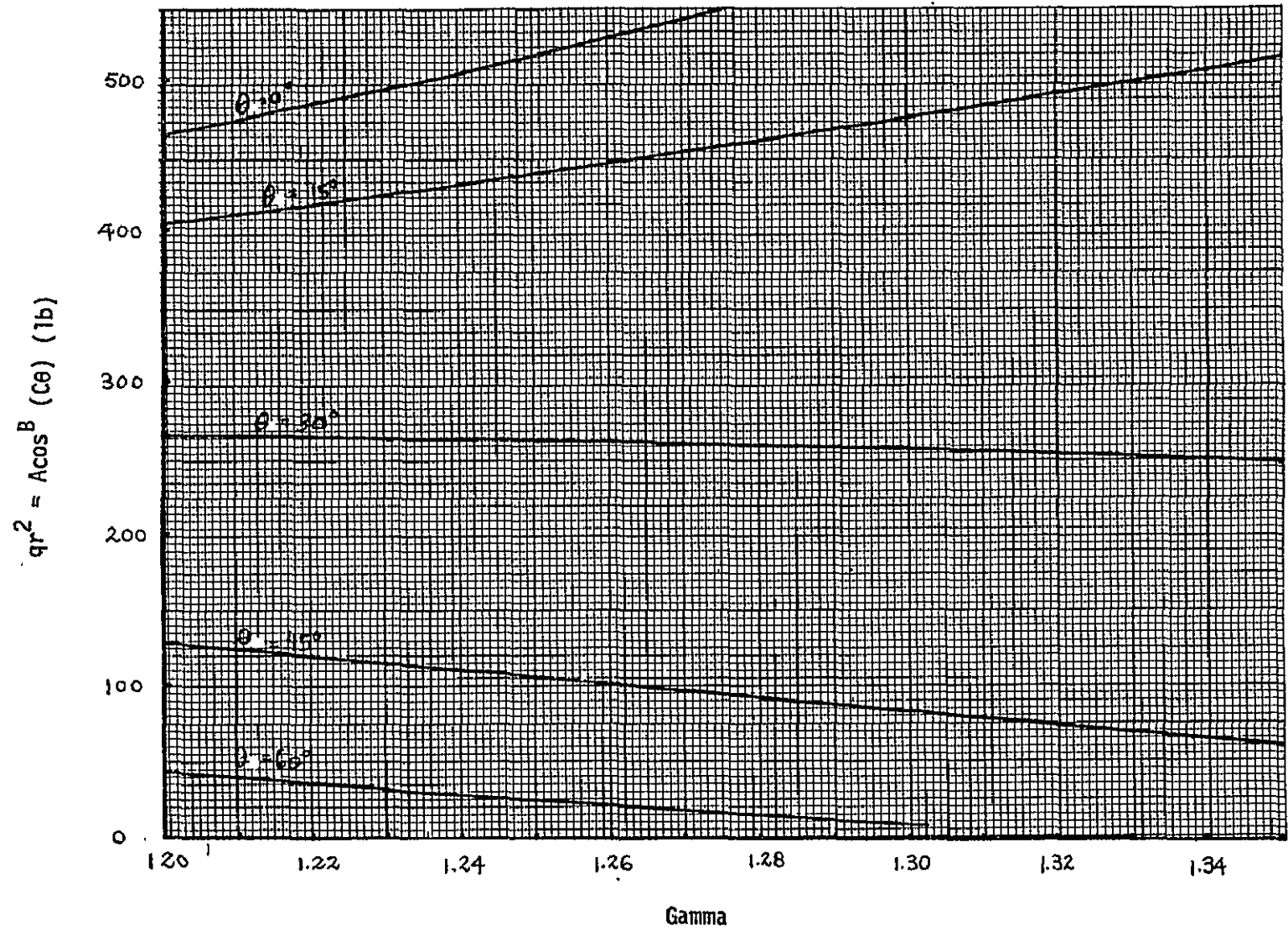
FIGURE 4.3.1-2   SENSITIVITY OF SOURCE FLOW – FLOWFIELD TO γ; RADIAL SLICES

TABLE 4.3.1-1 CONSTANTS USED FOR THE FIVE FLOWFIELD MODELS

CONSTANTS MODEL	A	B	C	β	θ_0
Simple Source Flow	480.4	8.47458	.77102	N/A	N/A
Source Flow with Boundary Layer Correction	480.4	8.47458	.77102	4.94	51.5^0
Source Flow with Curve-Fit Constants	480.4	8.47458	.77102	4.94	30^0
MPAD Fit	N/A - see Equation 4.3.1-3				
Patched Source Flow: Region[a] (1)	500				
(2)	480				
(3)	480	8.47458	.77102	4.94	30^0
(4)	400				
(5)	460				

[a] See Figure 4.3.1-7

(a) Near Field Dynamic Pressure Contours

Axial distance (ft)

FIGURE 4.3.1-3   SIMPLE SOURCE FLOW VS. STANDARD DATA
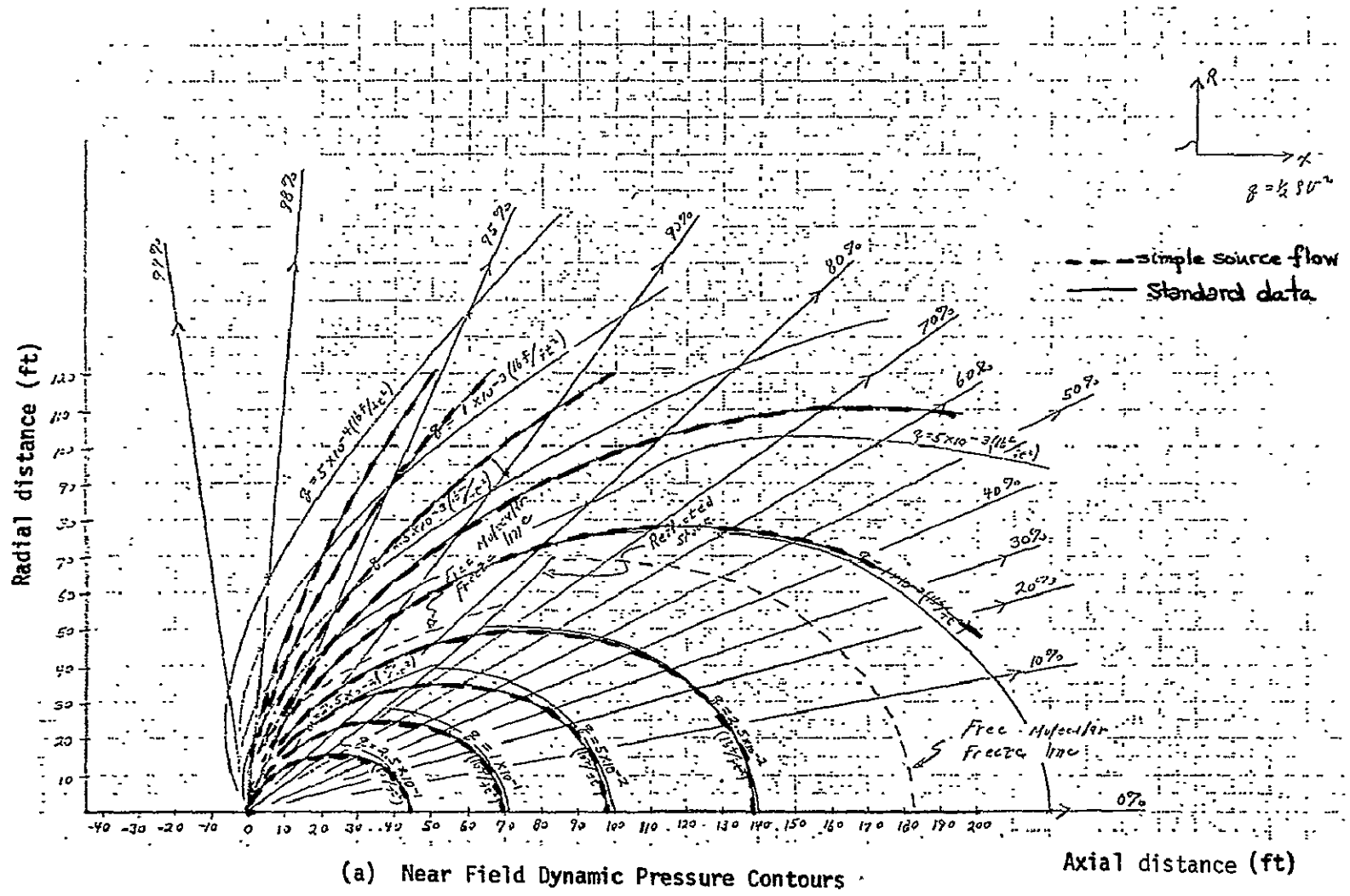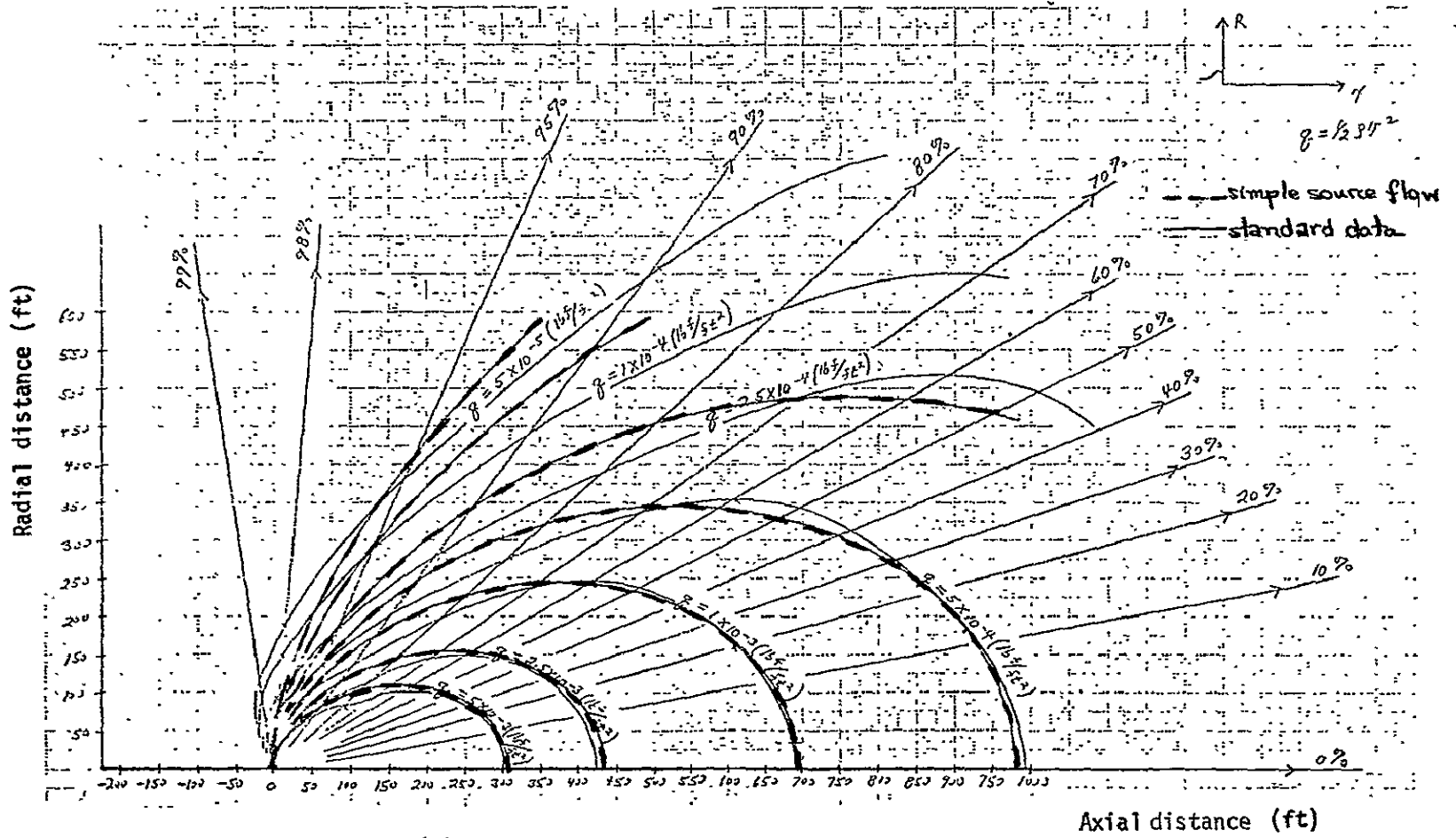
(b) Far Field Dynamic Pressure Contours

FIGURE 4.3.1-3   (Continued)

(a) Near Field Dynamic Pressure Contours

FIGURE 4.3.1-4   SOURCE FLOW WITH BOUNDARY LAYER CORRECTION VS. STANDARD DATA
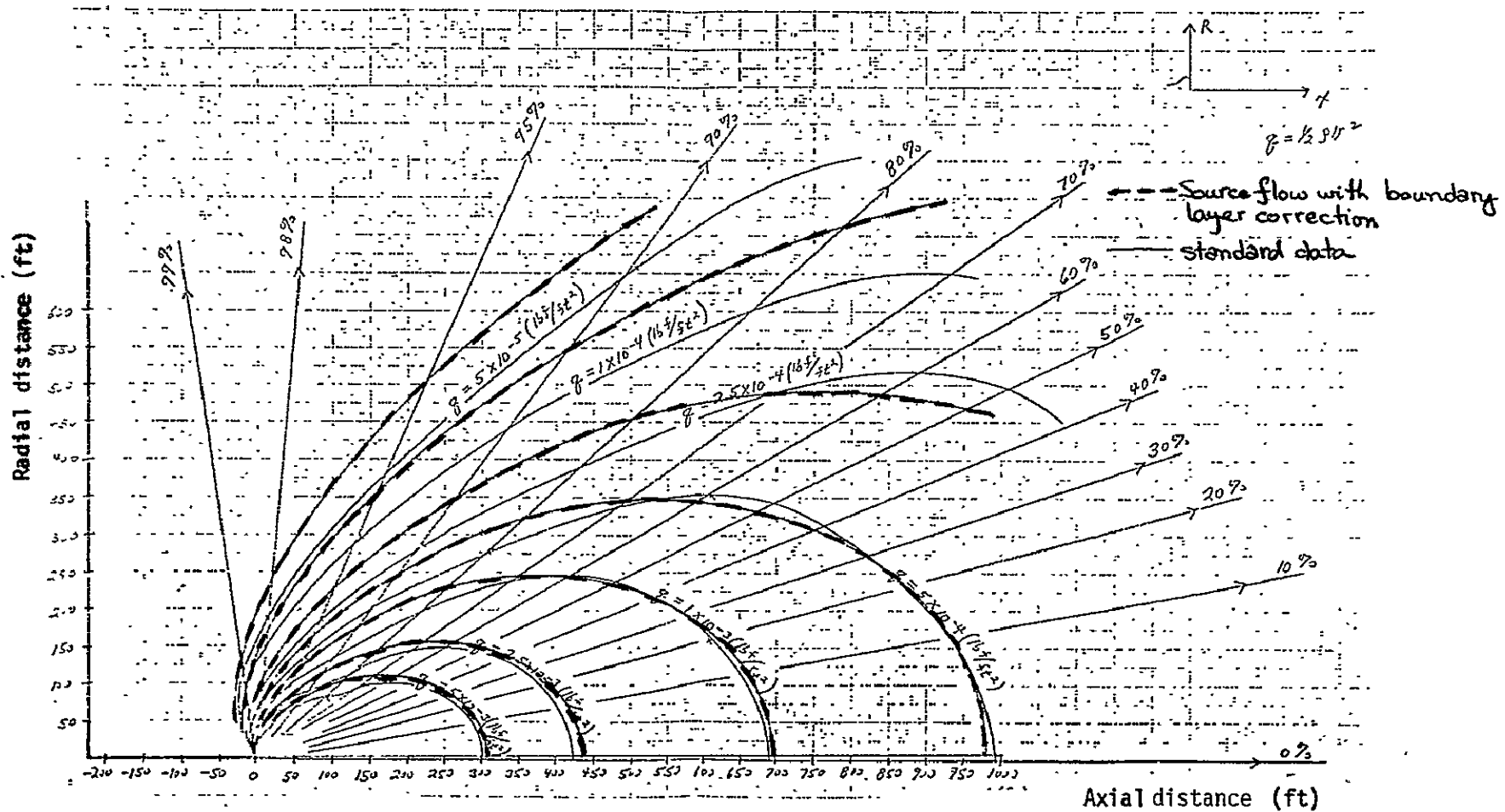
(b)   Far Field Dynamic Pressure Contours

FIGURE 4.3.1-4   (Continued)
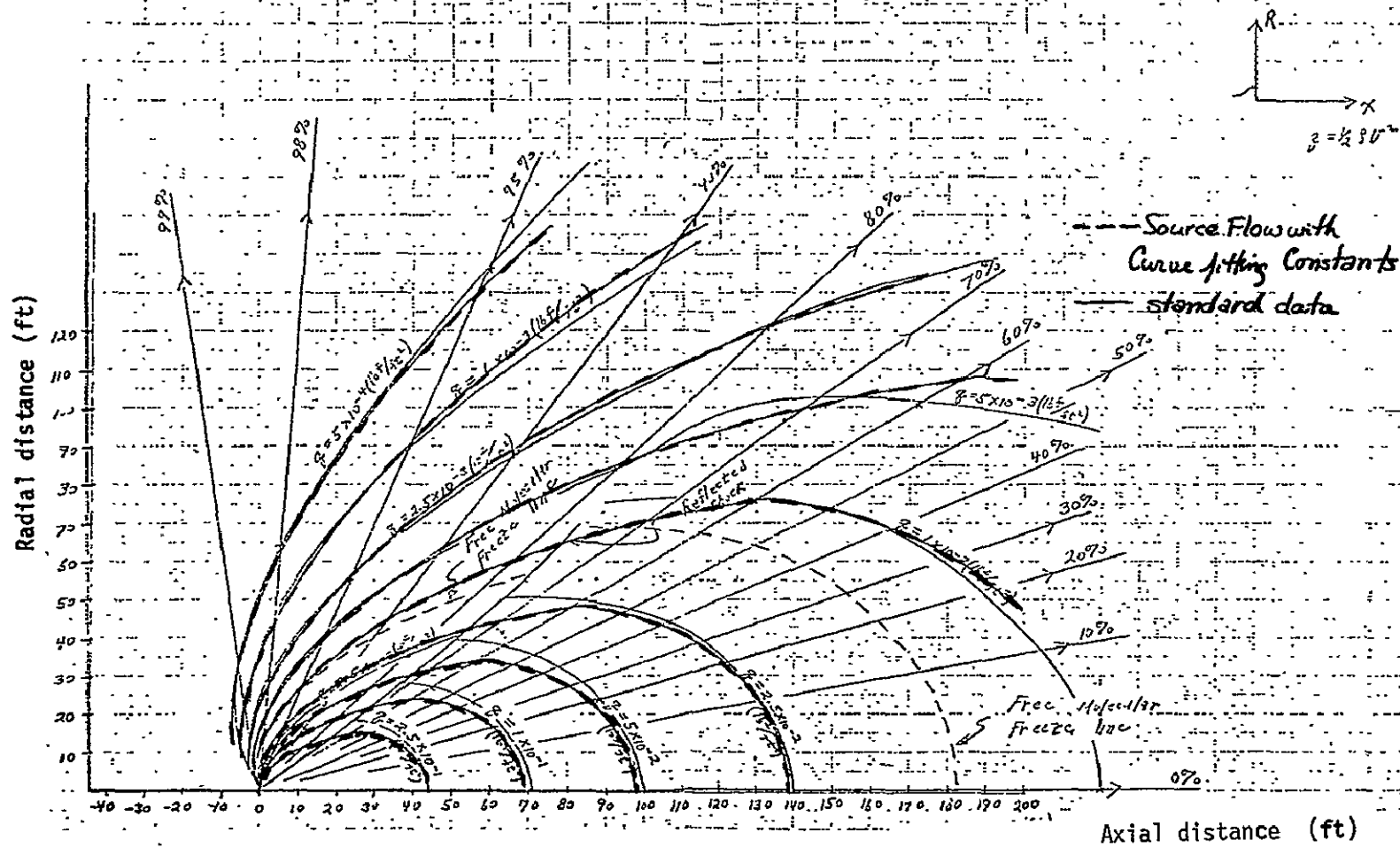
(a)   Near Field Dynamic Pressure Contours

FIGURE 4.3.1-5   SOURCE FLOW WITH CURVE FITTING CONSTANTS VS. STANDARD DATA
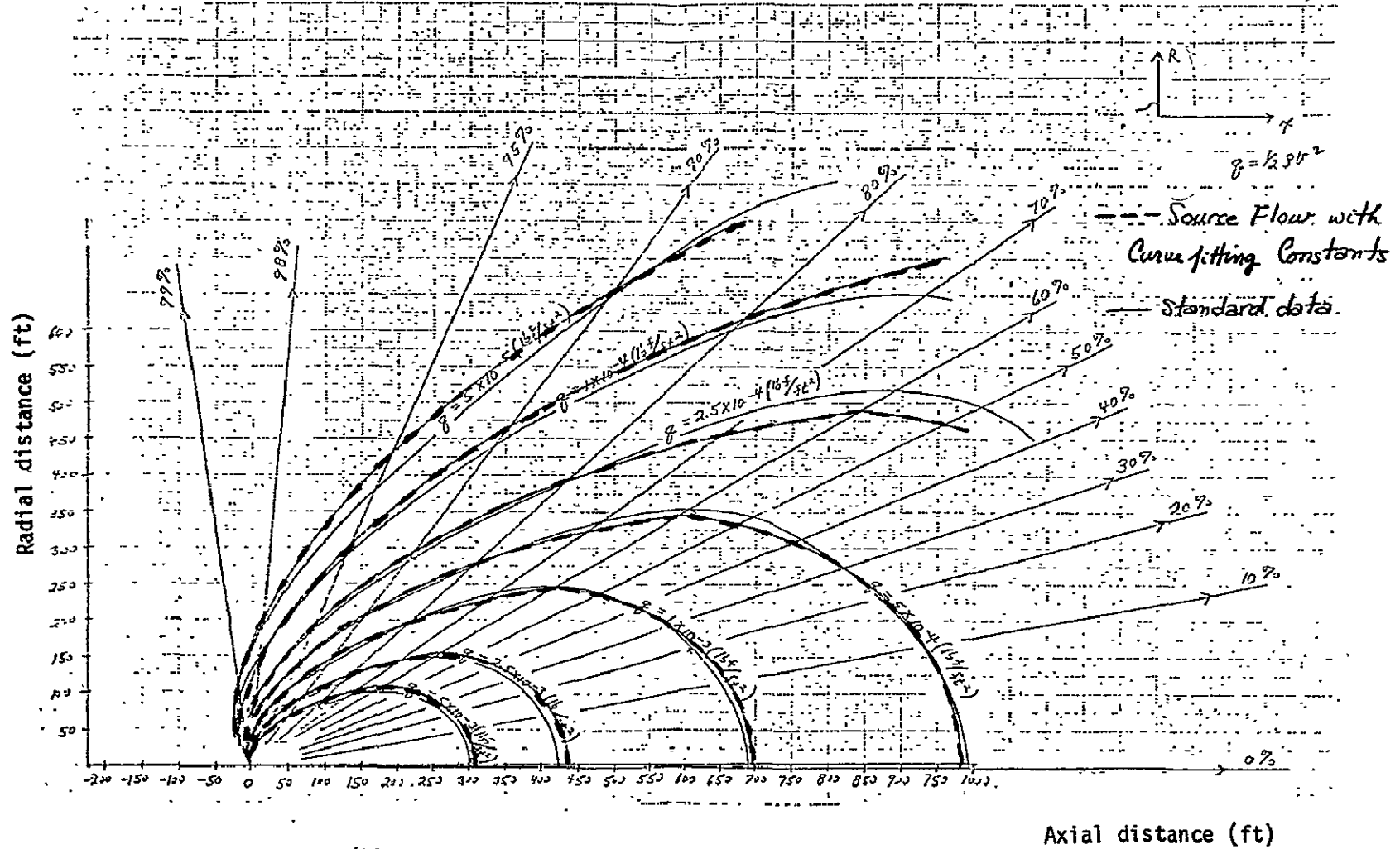
(b) Far Field Dynamic Pressure Contours

FIGURE 4.3.1-5 (Continued.)

(a) Near Field Dynamic Pressure Contours
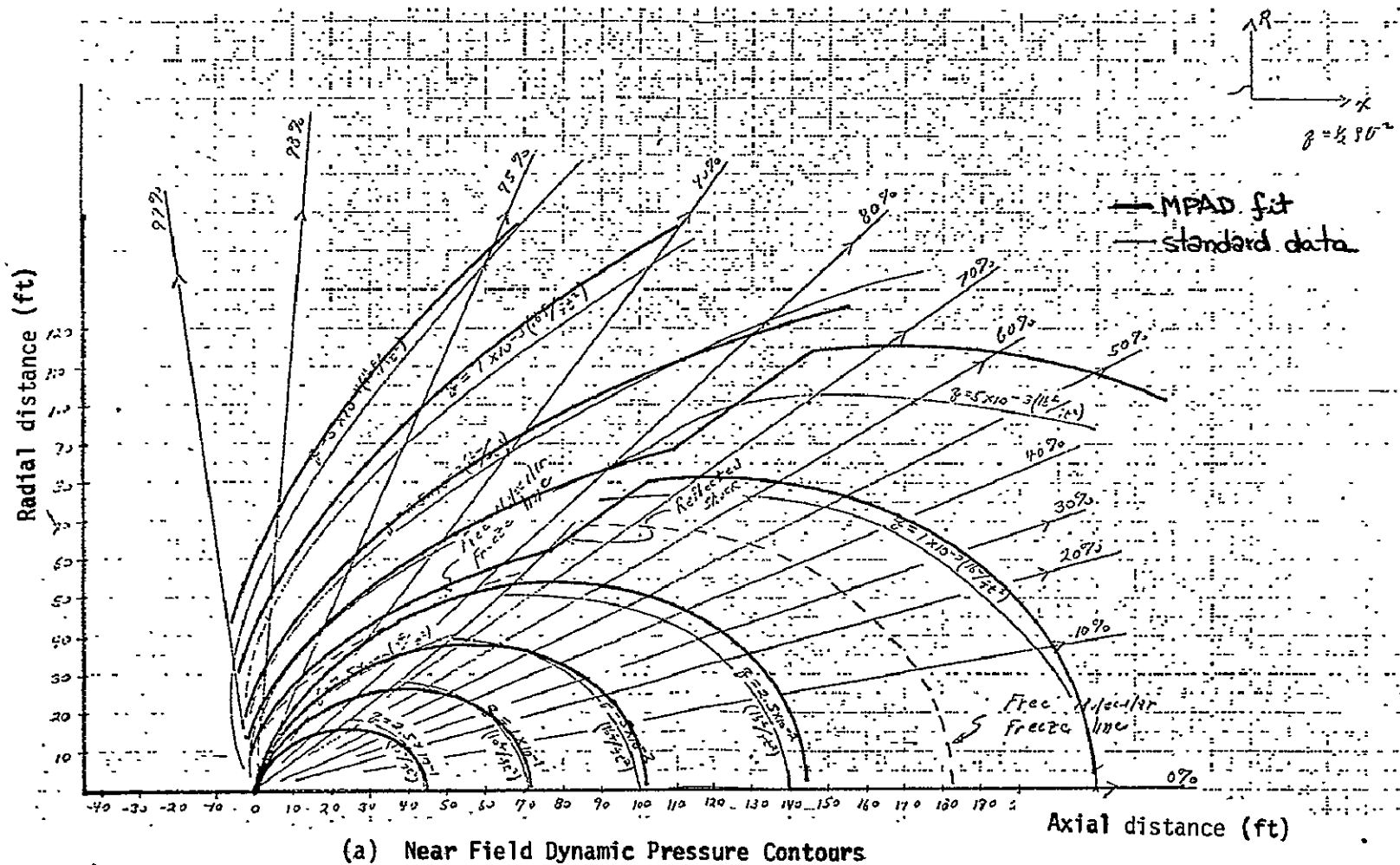
FIGURE 4.3.1-6 MPAD FIT VS. STANDARD DATA
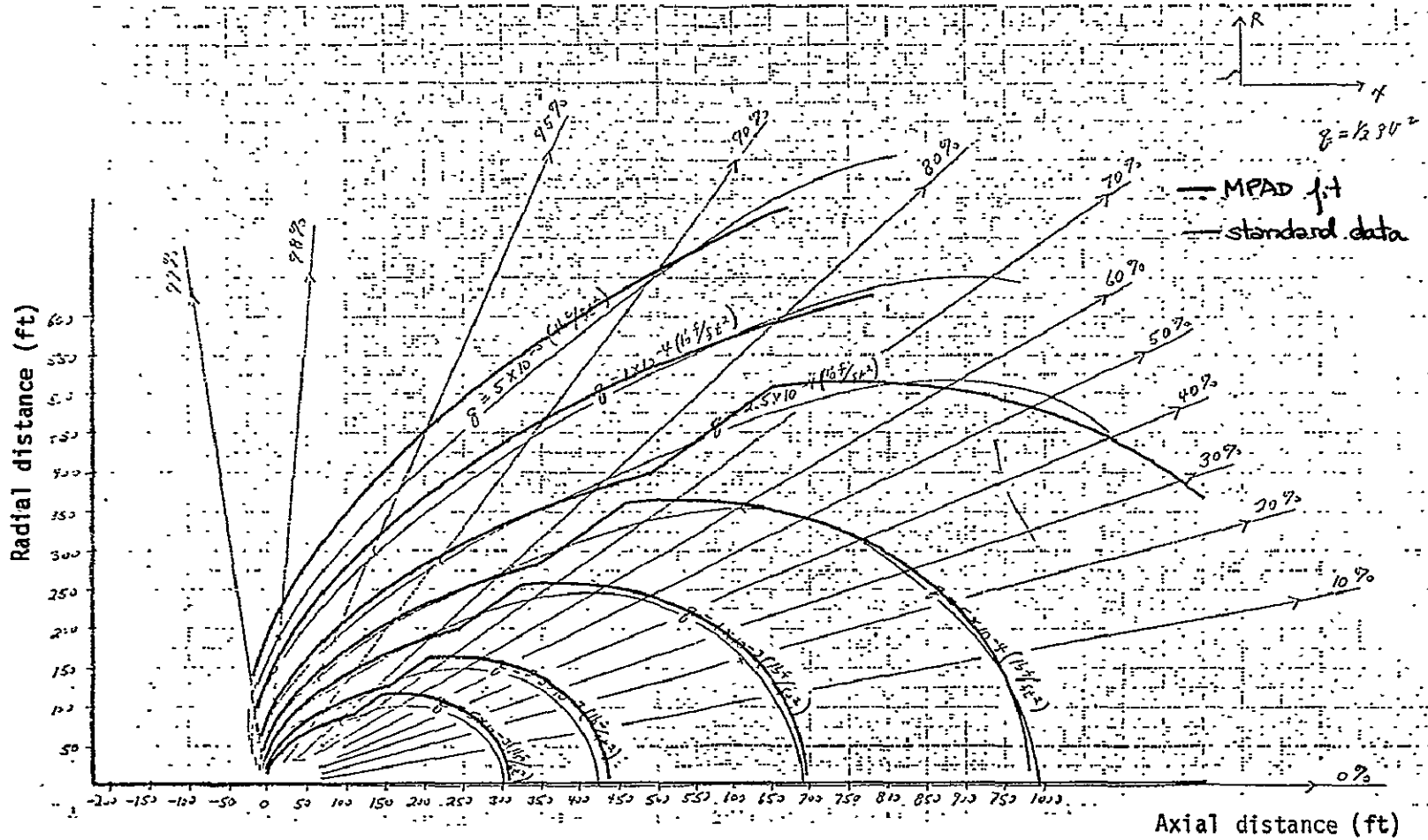
(b) Far Field Dynamic Pressure Contours

FIGURE 4.3.1-6 (Continued)
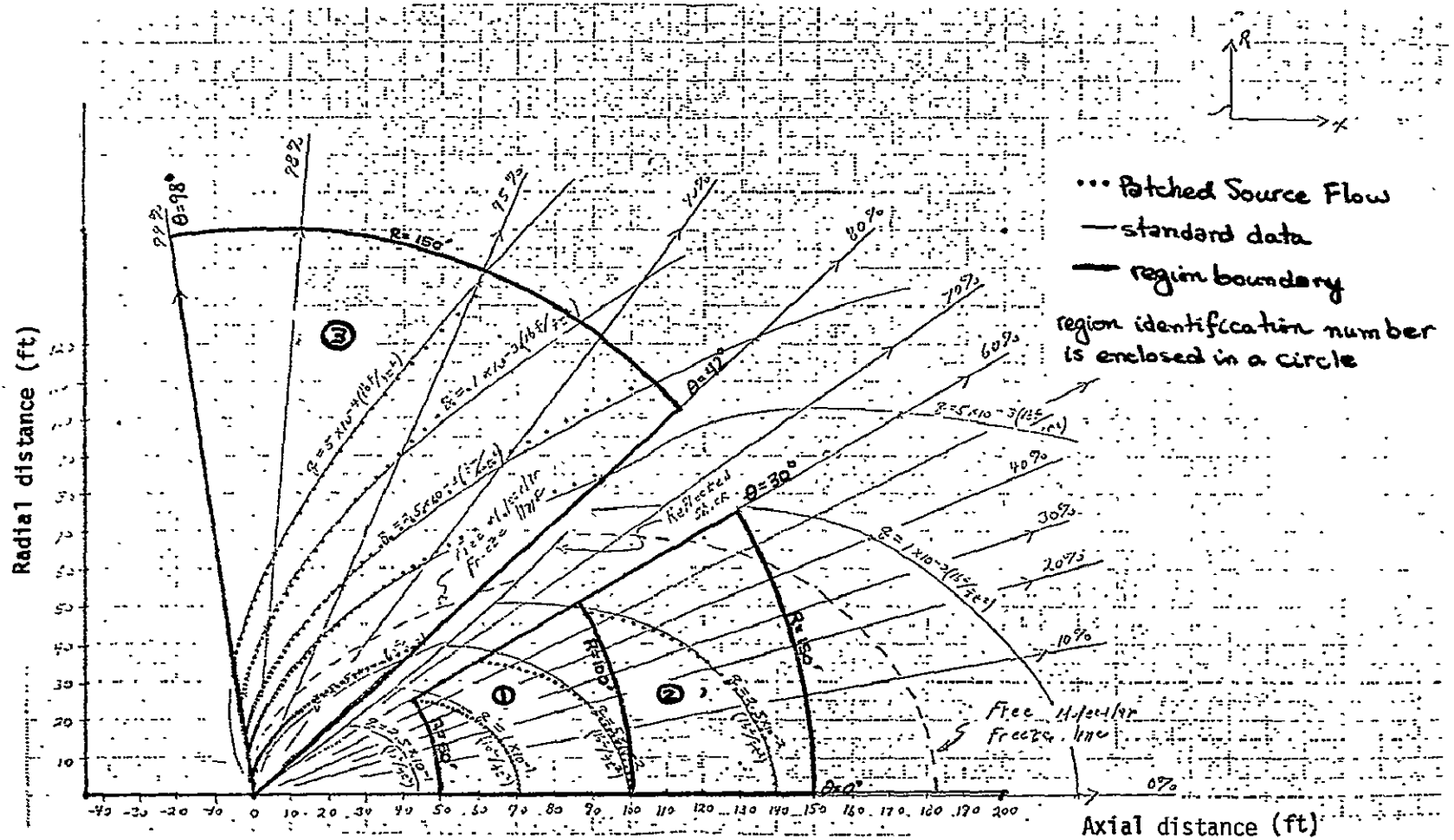
(a) Near Field Dynamic Pressure Contours

FIGURE 4.3.1-7 PATCHED SOURCE FLOW VS. STANDARD DATA

88
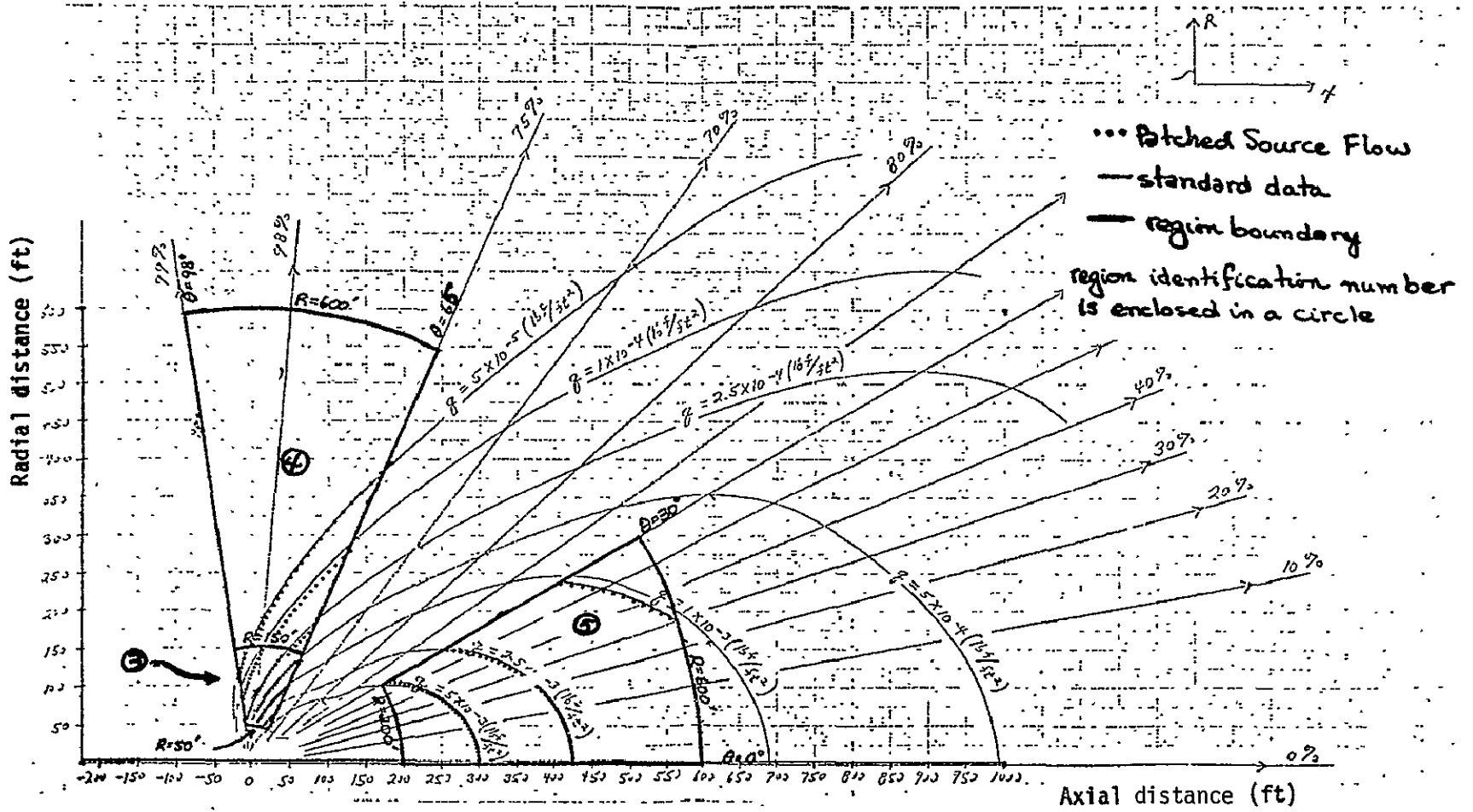
(b)   Far Field Dynamic Pressure Contours

FIGURE 4.3.1-7   (continued)
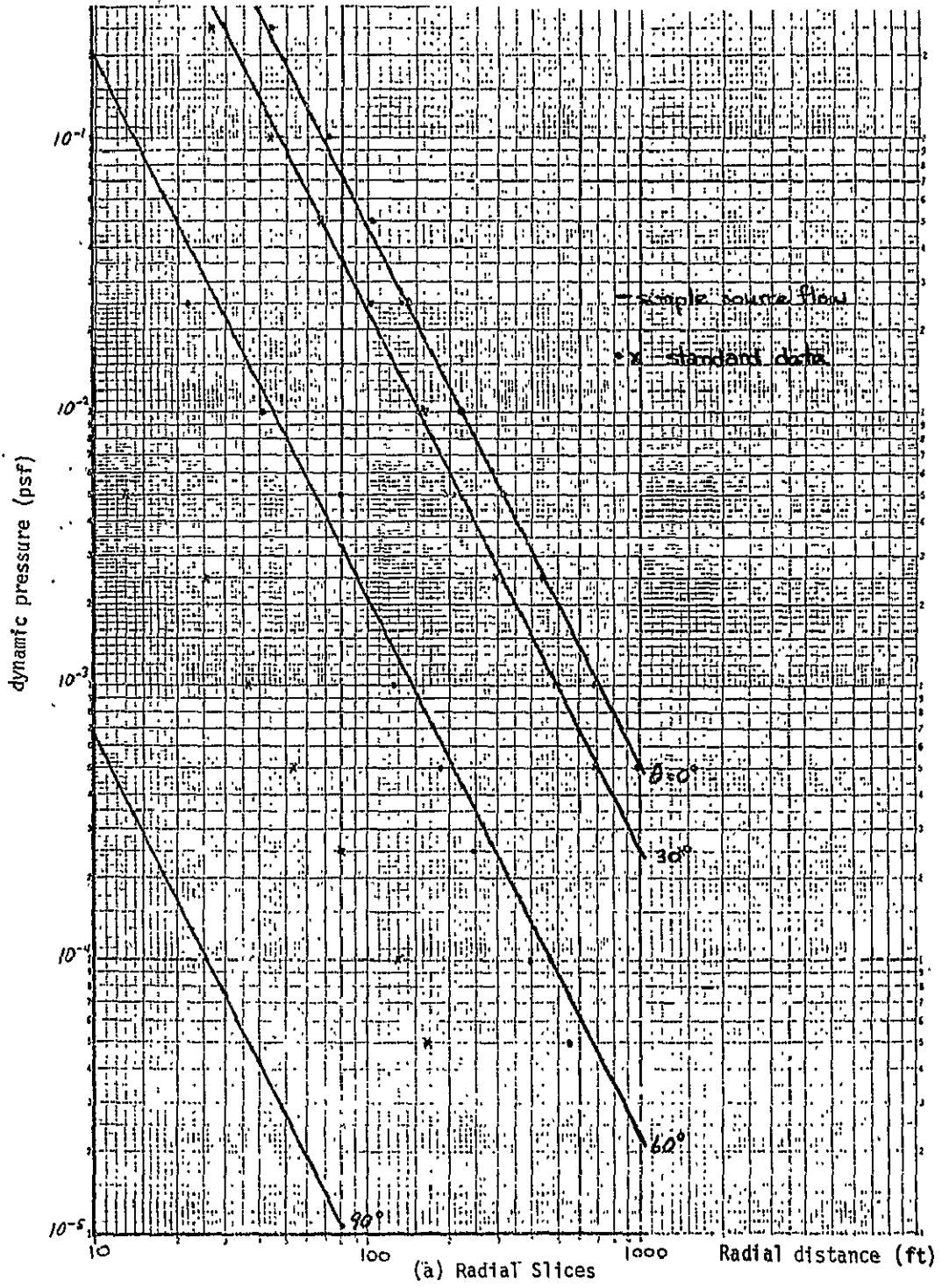
FIGURE 4.3.1-8 SIMPLE SOURCE FLOW VS. STANDARD DATA
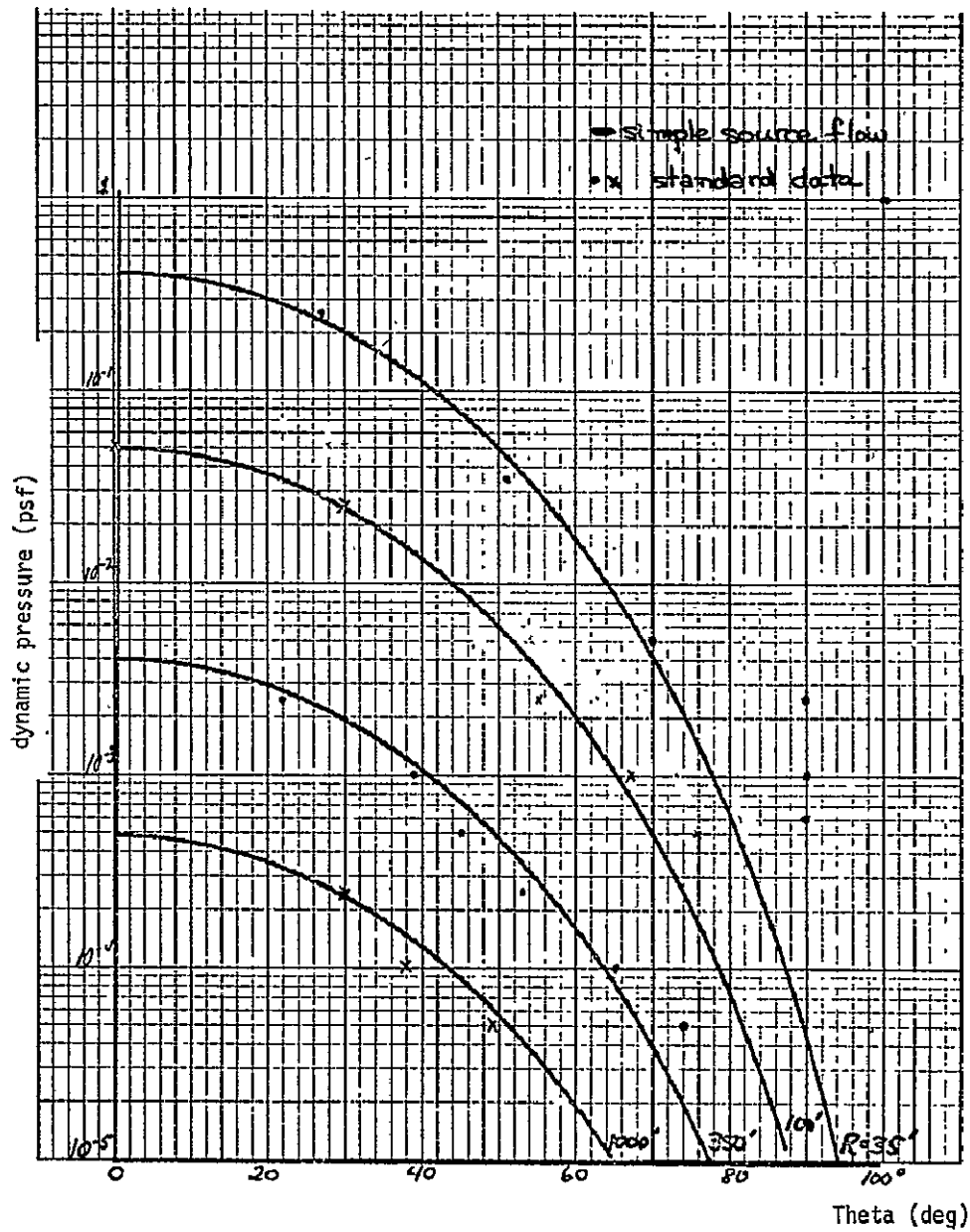
(b) Angular Slices

FIGURE 4.3.1-8 (continued)
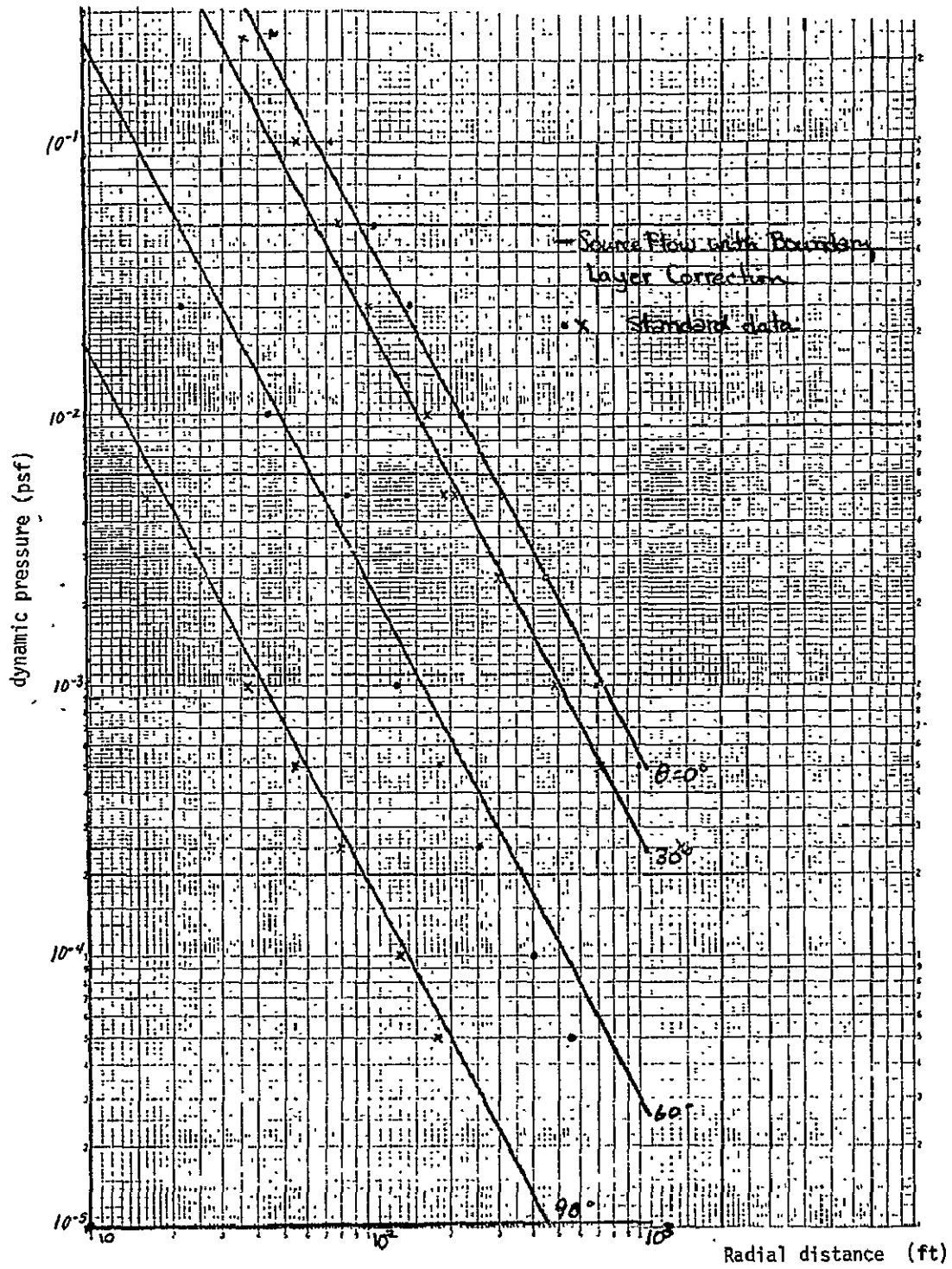
(a) Radial Slices

FIGURE 4.3.1-9 SOURCE FLOW WITH BOUNDARY LAYER CORRECTION VS. STANDARD DATA

82

y-axis: dynamic pressure (psf)

x-axis: Theta (deg)

Curve labels: Source Flow with Boundary Layer Correction; x standard data; R=35'; 100'; 150'; 350'
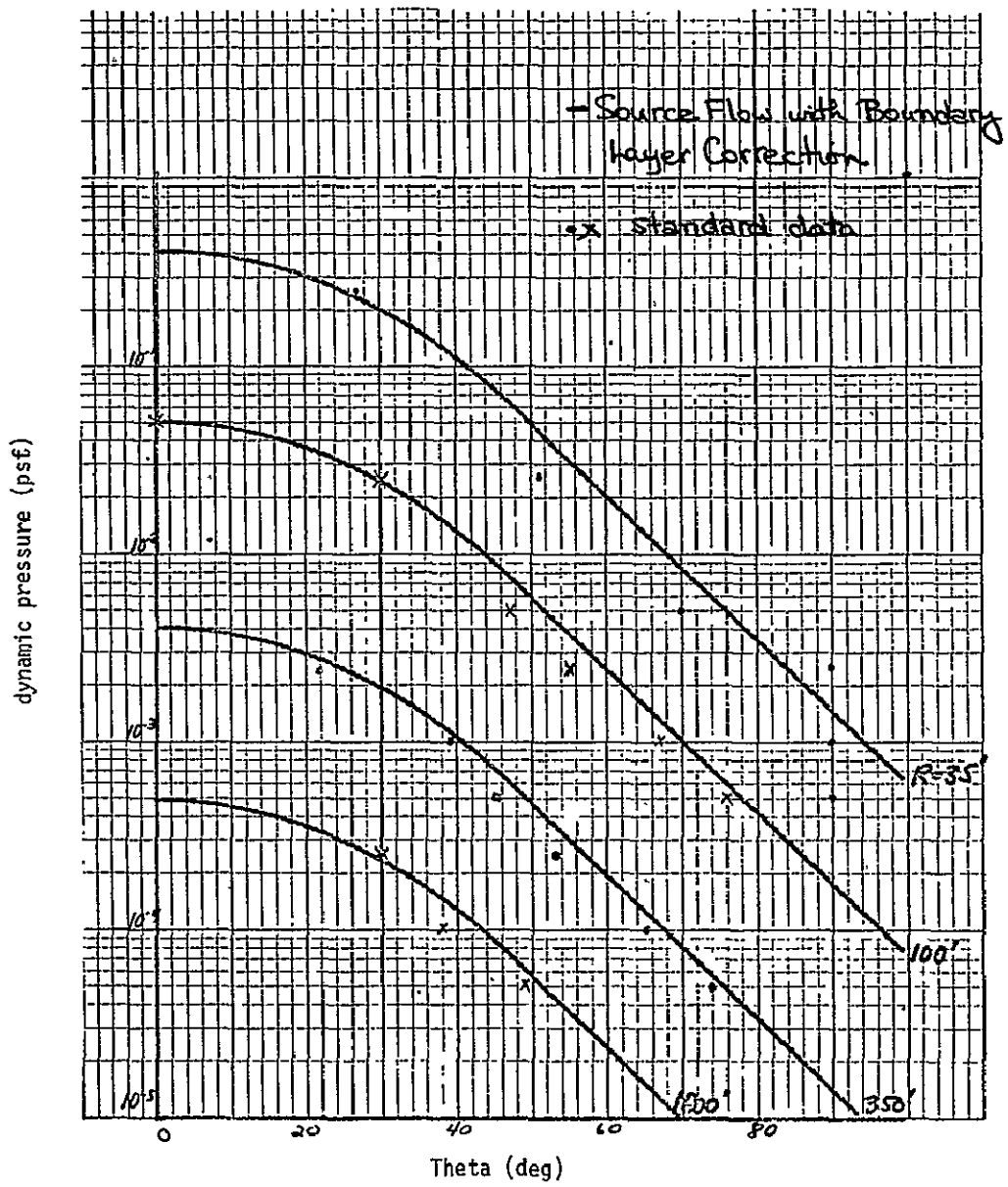
(b) Angular Slices

› FIGURE 4.3.1-9 (continued)
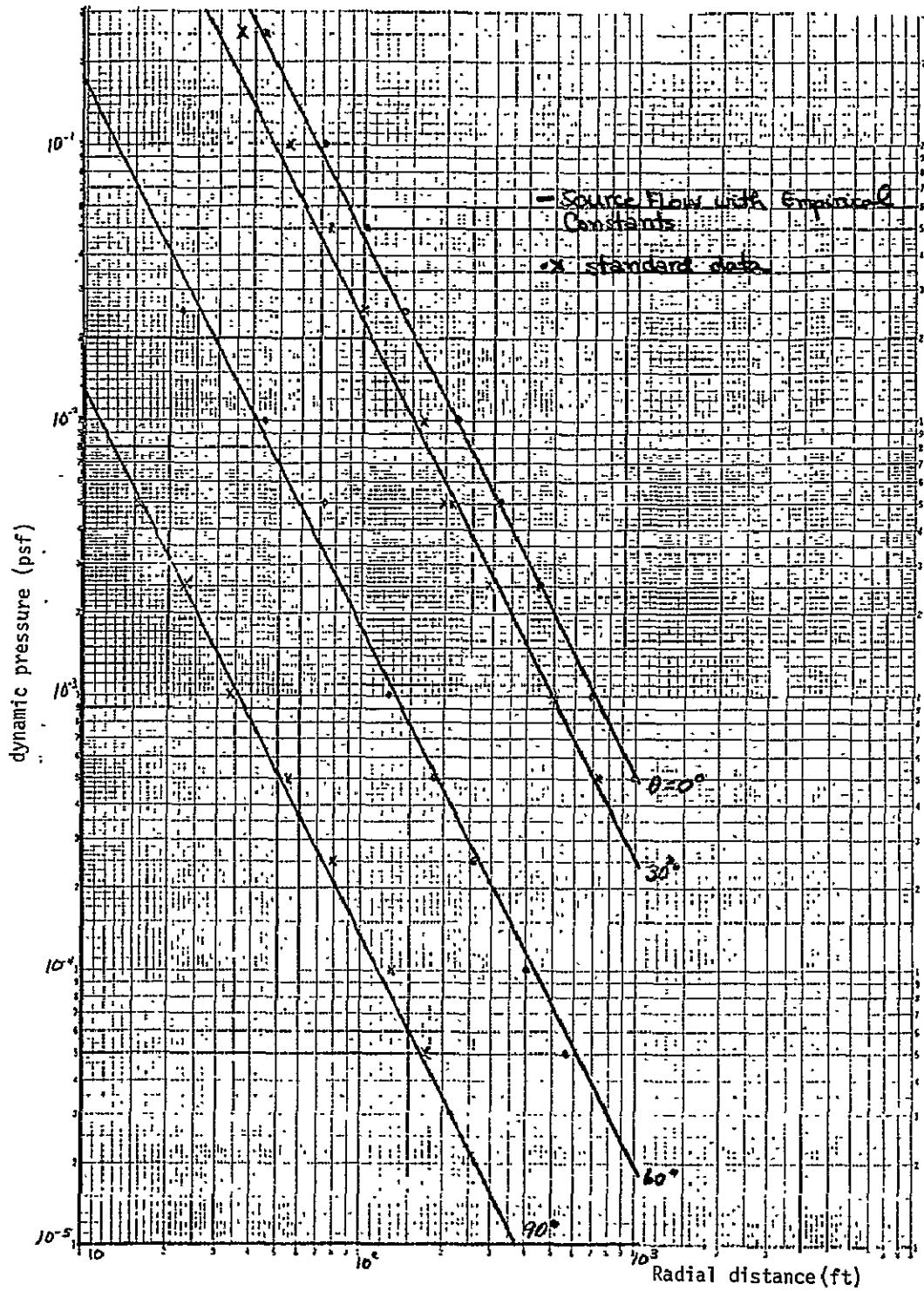
(a) Radial Slices

FIGURE 4.3.1-10 SOURCE FLOW WITH CURVE FITTING CONSTANTS VS. STANDARD DATA

84
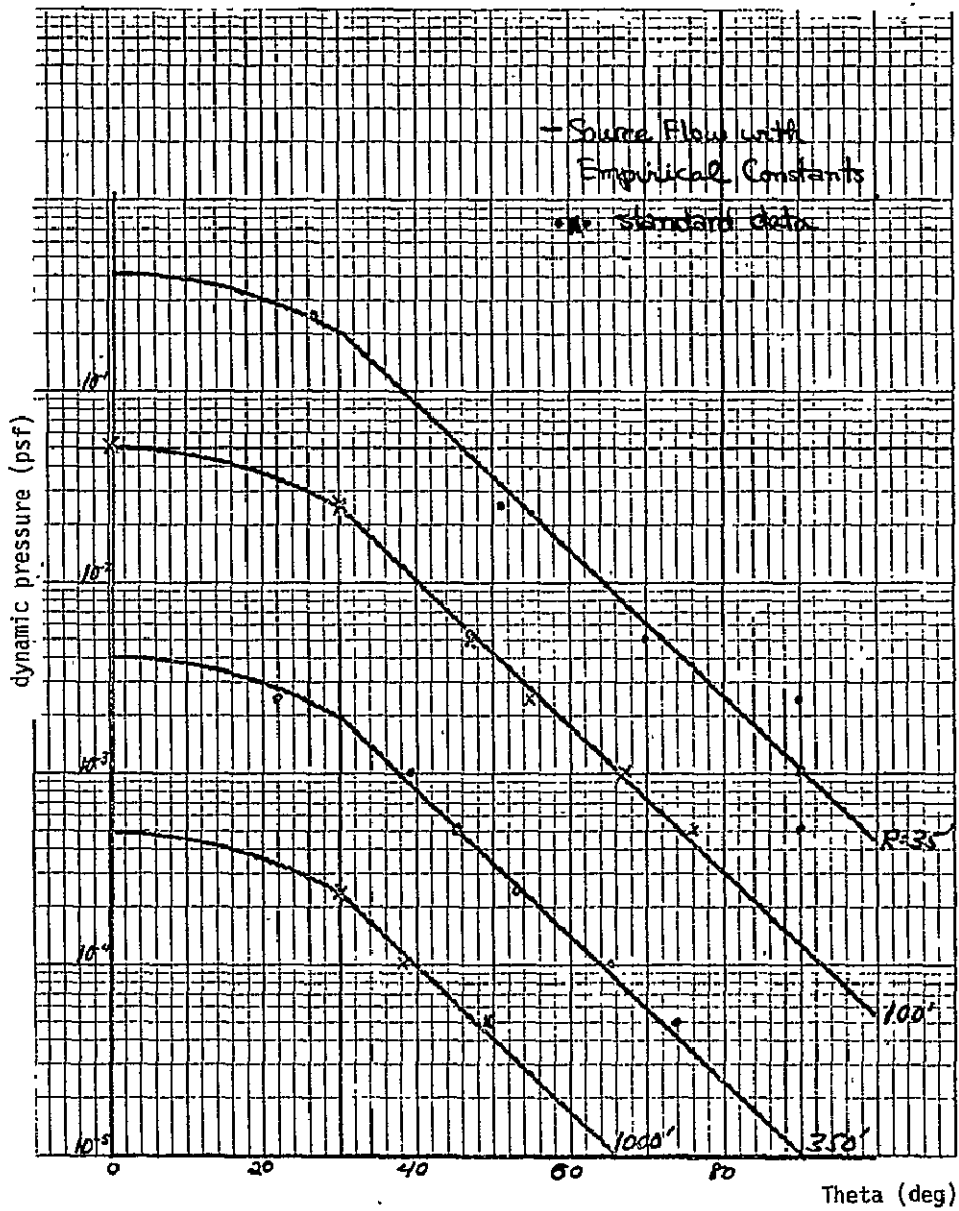
(b) Angular Slices

FIGURE 4.3.1-10 (continued)
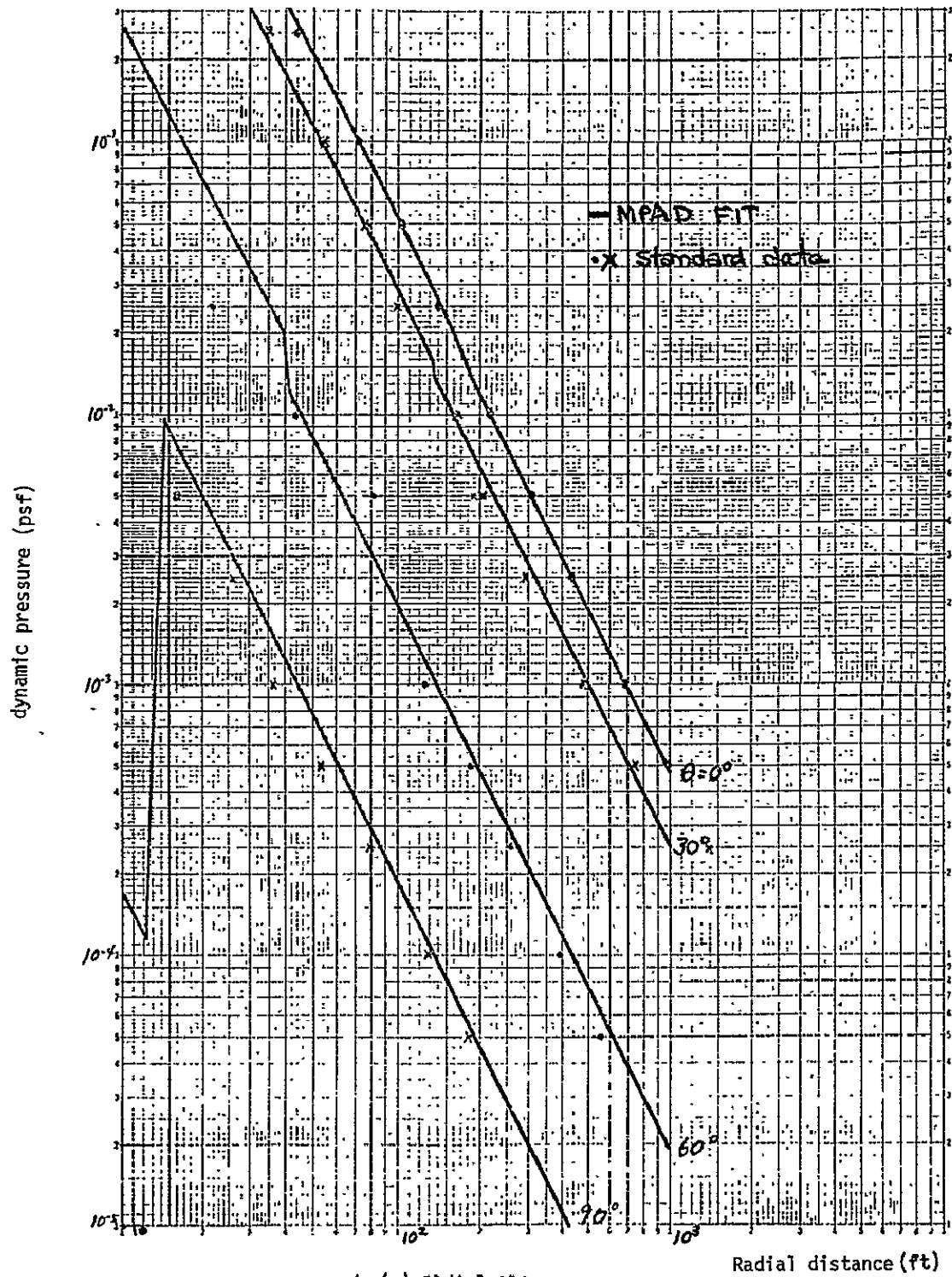
(a) Radial Slices

FIGURE 4.3.1-11 MPAD FIT VS STANDARD DATA

86
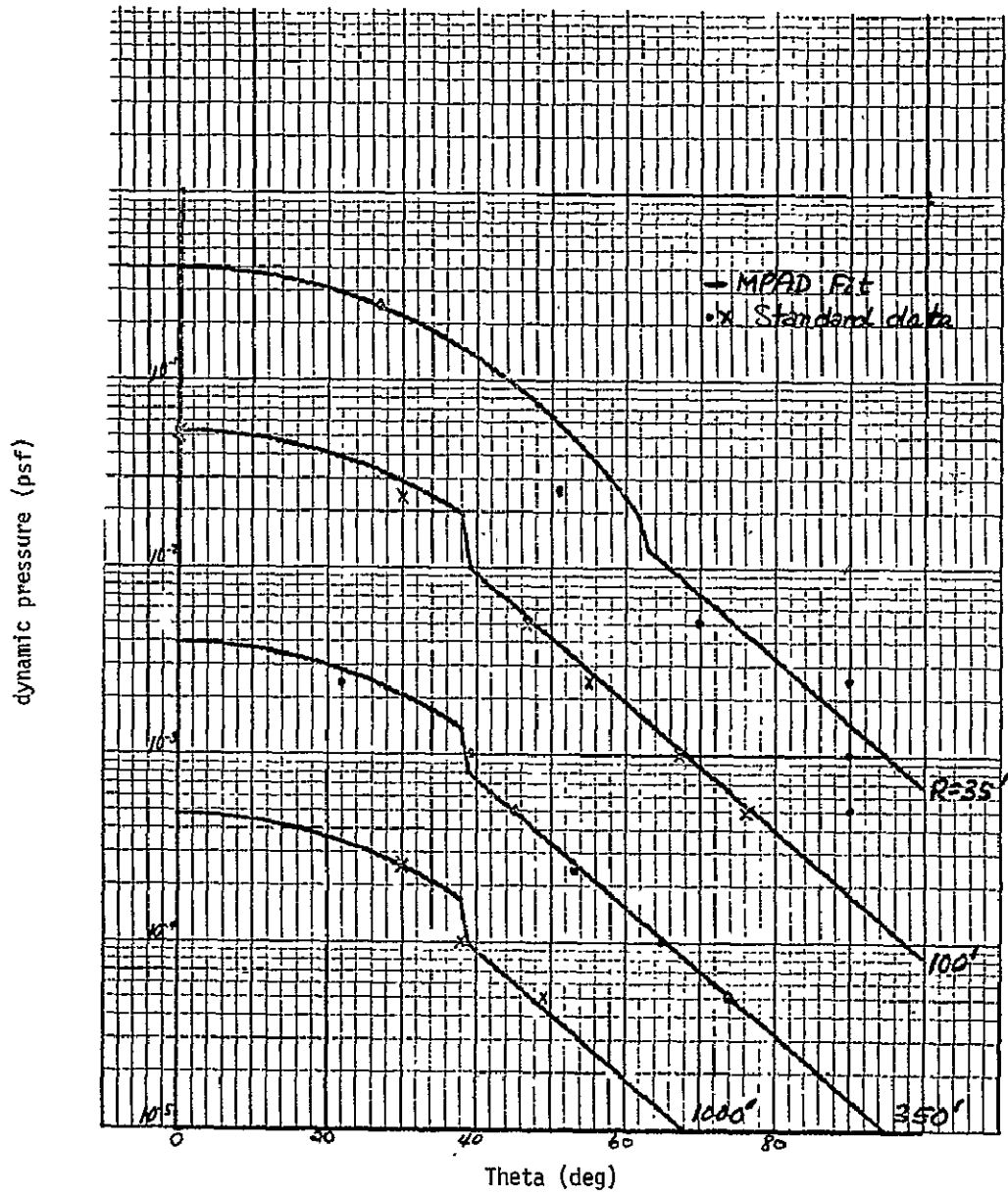
(b) Angular Slices

FIGURE 4.3.1-11 (continued)

dynamic pressure (psf)

Radial distance (ft)

Patched Source Flow
standard data

Region numbers are in circles.

θ=0°
θ=20°
θ=30°

(a) Radial Slices
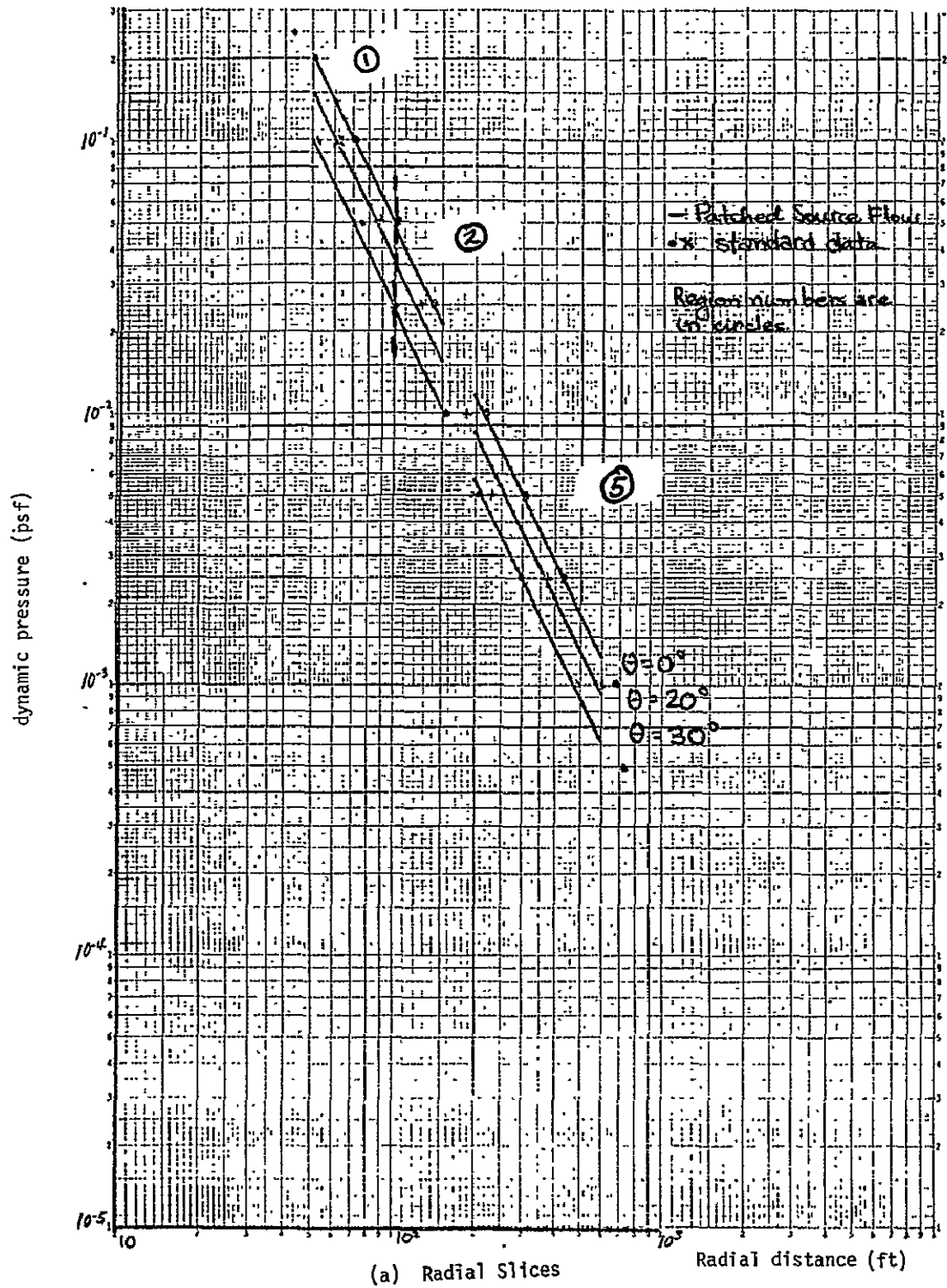
FIGURE 4.3.1-12 PATCHED SOURCE FLOW VS. STANDARD DATA

88
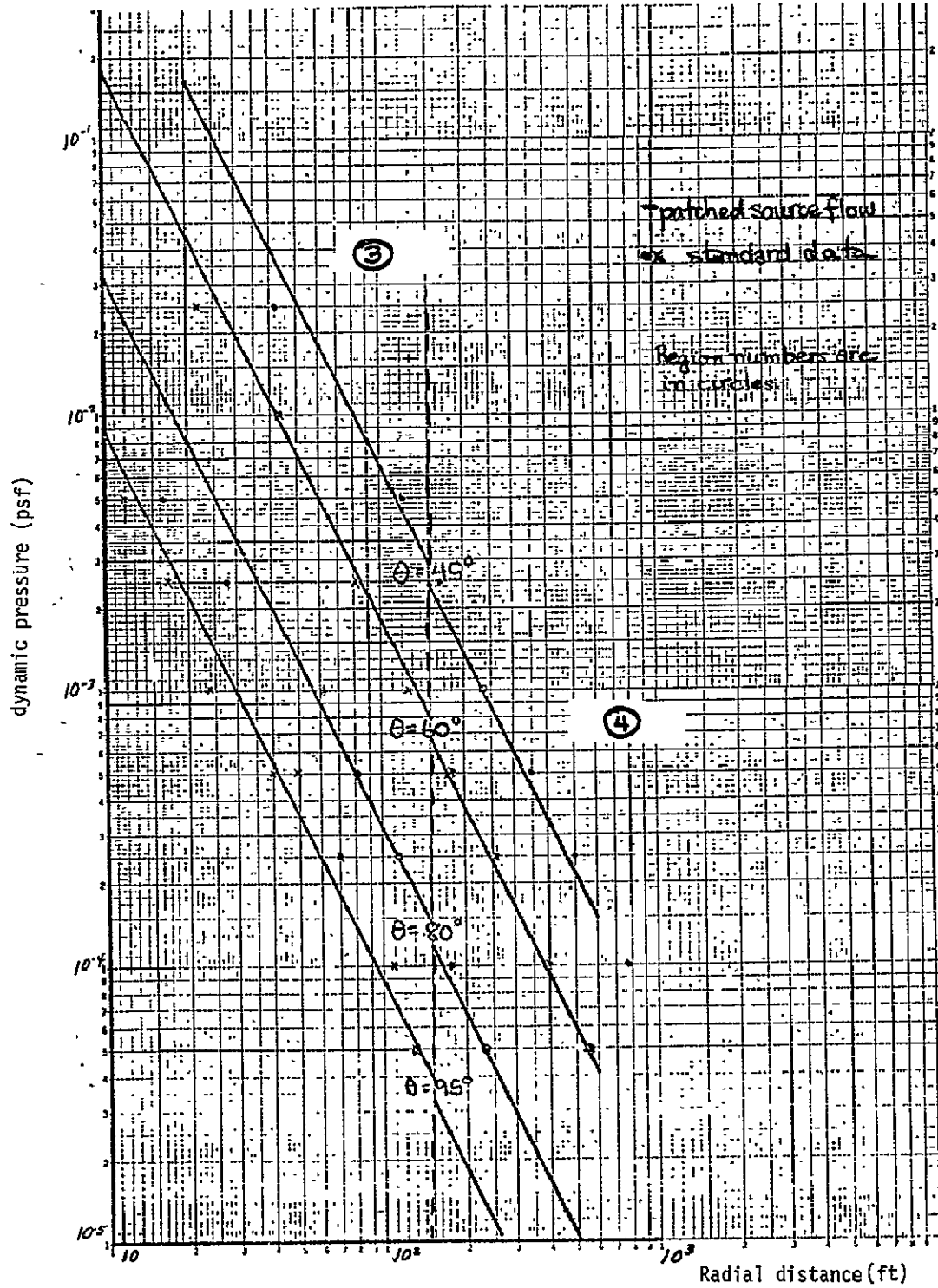
(a) continued

FIGURE 4.3.1-12 (continued)

(b) Angular Slices

FIGURE 4.3.1-12 (continued)

90
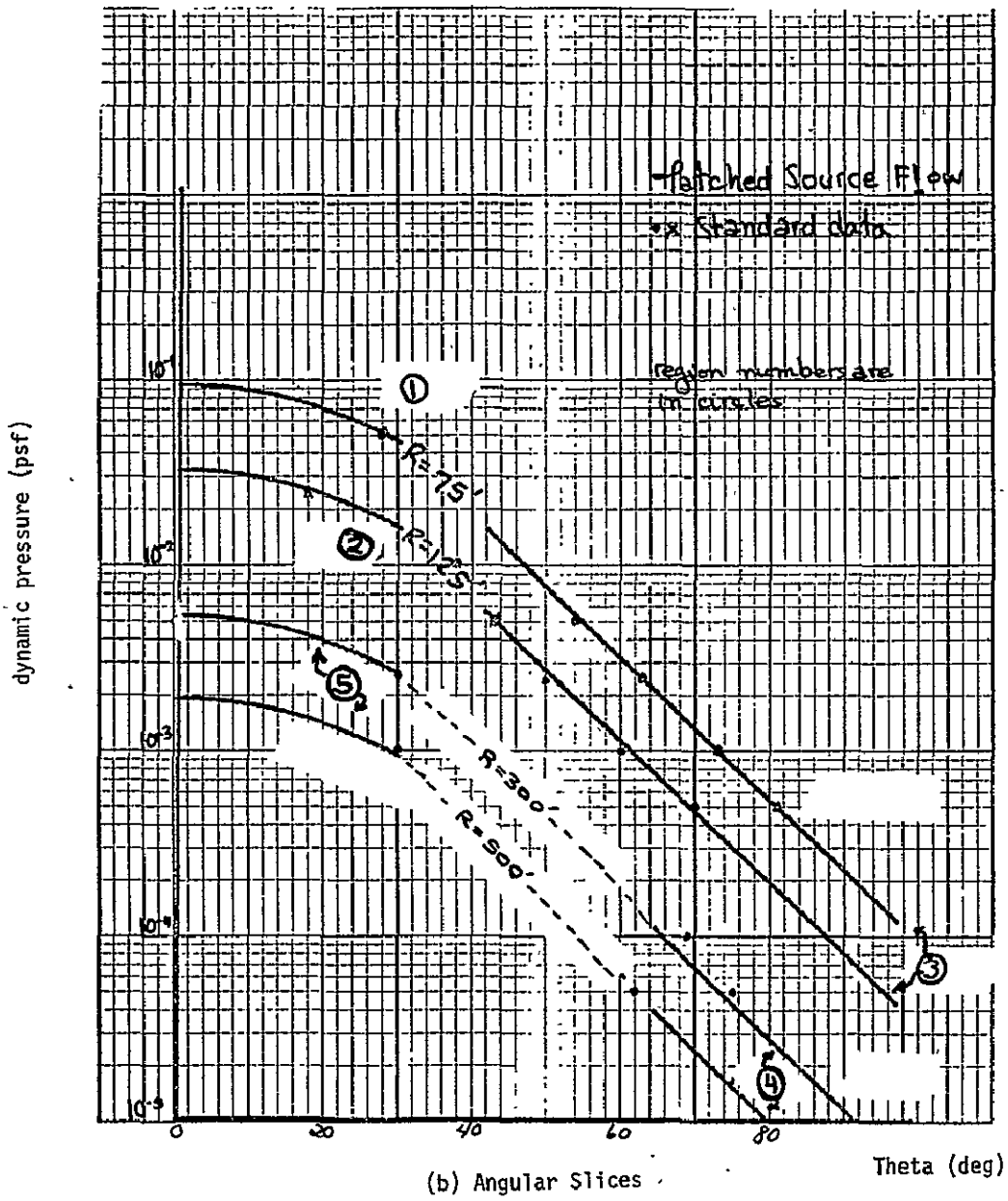
The source flow technique with curve-fit constants shows good agreement, with typical errors less than 10%. The MPAD model shows similar accuracy, with slightly larger core requirements. The MPAD model fails in the high angle, very close-in region, but this region is of little concern to Shuttle plume problems.

The technique which uses patched source-flow-like equations typically has errors around 5%, except for high angle close-in distances. It is interesting to note that only the scaling factor, A, changed in the different regions of the plume under consideration.

4.3.1.5 Preliminary Conclusions and Recommendations

Based upon the above analysis and results, techniques using theoretical values for source flow constants and boundary layer constants do not predict dynamic pressures to within 10% of the standard data for all regions of the plume, and dynamic pressures are seen to be highly sensitive to the chosen value of the constant γ. We also conclude that a boundary layer correction term is necessary.

The source flow technique with curve-fit constants and the MPAD fit both predict standard data to about 10% accuracy. Using patched source flow equations, errors are typically less than 10%.

It appears that the patched source flow technique is the most promising as far as minimizing complexity and maximizing accuracy. Therefore, this method is recommended for the flowfield model.

The assumption of radial streamlines is justified in the regions of the plume under consideration and is also recommended.

4.3.2 Thruster Scarfing (Short Side/Long Side)

4.3.2.1 The Question

Is it necessary to account for the scarfed nozzle effect on the plume definition? The engines which must be considered are the engines whose plumes (or partial plumes) may affect payload deployment and retrieval operation, i.e., the plumes which expand above the orbiter vehicle. These engines are:

Engine	Plume to be Considered*
Forward +Z	Entire plume
Forward -X	Only the portion of the plume which expands from the short side of the scarfed nozzle
Forward ±Y	Only the portion of the plume which expands above the orbiter
Aft ±Y	Only the portion of the plume which expands above the orbiter

*See Figure 4.3.2-1

The -X engine is the most severely scarfed of the engines of concern here; however, the region of the plume which will affect the payloads expands from the short side of the scarfed nozzle; see Figure 4.3.2-1. The scarfing of the short side of the -X engine nozzle is quite minor in comparison to the standard unscarfed nozzle; see Figure 4.3.2-2. The forward +Z engine nozzles are scarfed the most of the engines whose plumes or partial plumes are of concern here. However, the scarfing of these engines is also quite small; the extent of scarfing for these engines is also presented in Figure 4.3.2-2. An indication of the extent of nozzle scarfing for the forward +Z engines and the forward and aft ±Y engines can be realized by noting the thrust vector is altered no more than 1.52° for any of these engines. The thrust vector for the -X engines is altered about 5.6° due to nozzle scarfing; however, the majority of this is due to the long side of the scarfed nozzle which does not affect the plume of concern here.

Region of Concern

Plume From Forward +Z Engine

Region of Concern

Region of Concern

Plume From Forward ±Y Engines

Region of Concern

Plume From Short Side of -X Scarfed Nozzle

Region of Concern

Region of Concern

Plume From Aft ±Y Engines
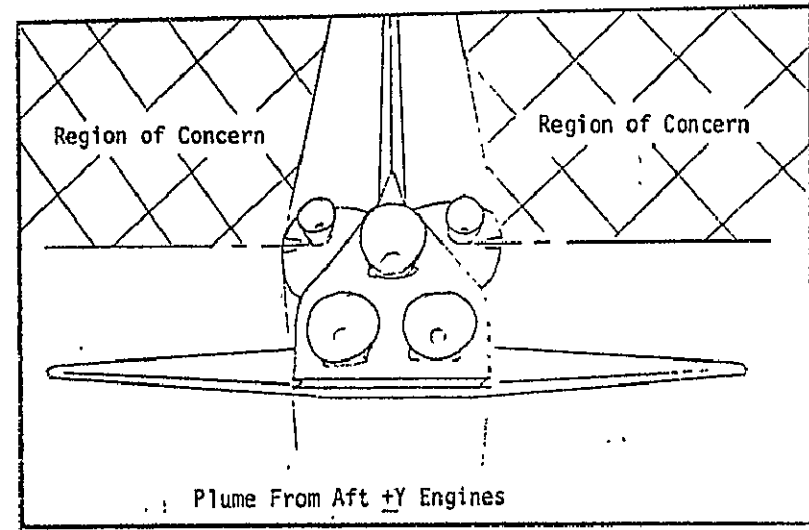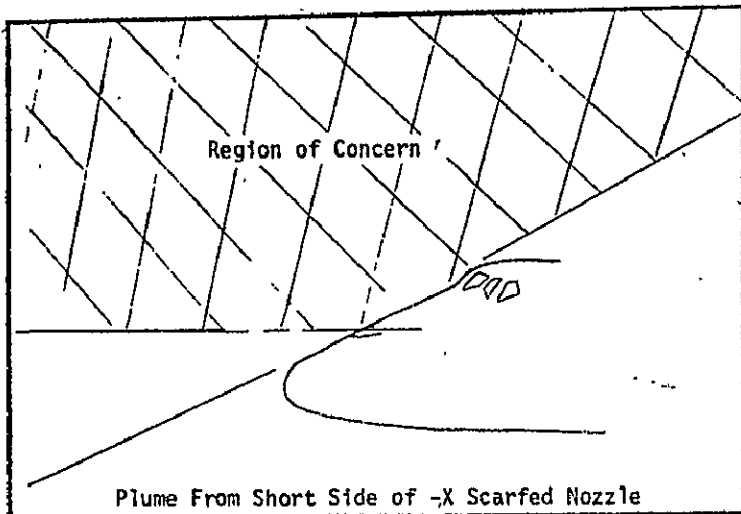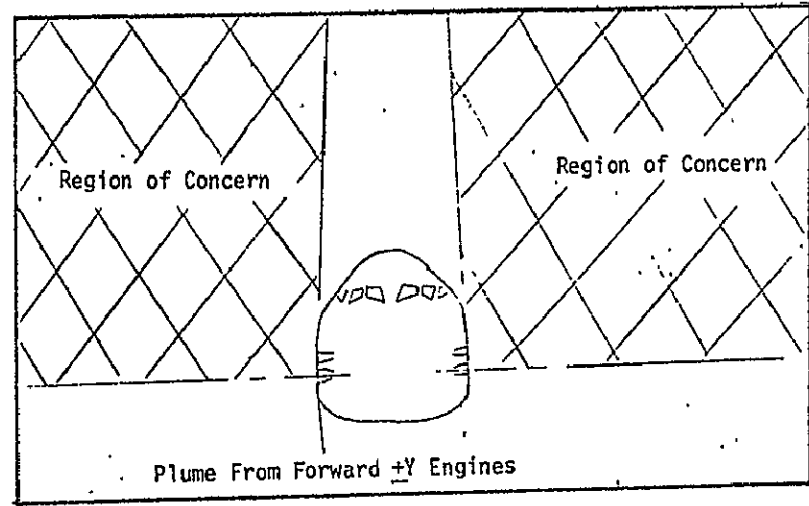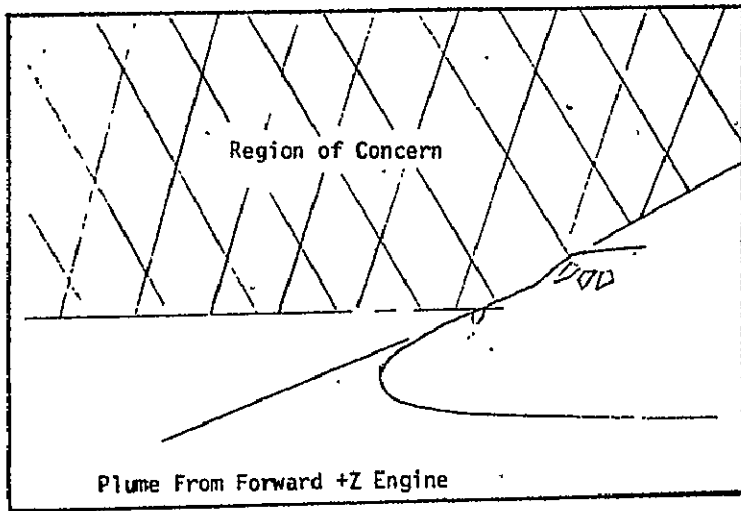
FIGURE 4.3.2-1   ENGINE PLUMES WHICH MAY AFFECT PAYLOAD DEPLOYMENT AND RETRIEVAL OPERATIONS. (Not to scale)

THROAT PLANE

A

NOT TO SCALE

STANDARD
RCS NOZZLE
EXIT

₵

8.8"   B
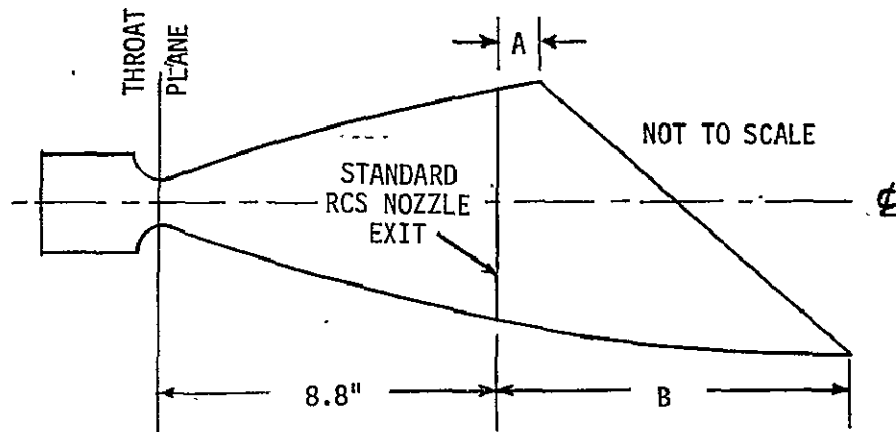
THRUSTER	SHORT SIDE SCARF ∿A IN.	LONG SIDE SCARF ∿B IN.
FWD +Z	0.71	10.00
FWD -X	1.05	22.62

FIGURE 4.3.2-2   FORWARD +Z AND -X RCS NOZZLE SCARF CONFIGURATIONS

94

Before this question can be answered, an understanding of the effect on the plume characterization due to nozzle scarfing is necessary. The scarfing of the nozzle alters the flow at the exit of the nozzle, and in turn the plume expansion at the nozzle lip. The flow will expand to a lower exit pressure at the long side of the scarf due to the increased expansion ratio, and in turn renders a smaller Prandtl-Meyer expansion at the nozzle lip. Also, the smaller lip angle on the long side renders a smaller total expansion. Therefore, the scarfing of these nozzles results in a reduced expansion at the nozzle lip. This reduced expansion at the nozzle lip affects only the outer regions of the plume; the internal regions of the plume are essentially unaffected by nozzle scarfing.

4.3.2.2 Tradeoff Factor/Considerations

To assess cost and performance factors, consideration of how the plume flow field from a scarfed nozzle would be implemented in the model is necessary.

Implementation: To implement the scarfed engine plumes in the model, a separate plume characterization for each scarfed engine must be generated and stored. This would require the storage of several plumes in addition to the unscarfed engine plume. Additional logic would be required to establish if the operational engine (or engines) are scarfed or unscarfed and then, since the scarfed engine plumes are not symmetrical, the orientation of the plume would need to be established.

"Cost" Factors: The cost of implementing the effects of the scarfed nozzles is the cost associated with storing, selecting, and accessing the scarfed engine plume flow field definitions, and establishing plume orientation.

Performance Factors: Since the effect on the plumes of interest here due to nozzle scarfing is minor, the increase in accuracy in defining the plume impingement effects utilizing the scarfed engine plume as opposed to utilizing the standard unscarfed engine plume is minimal.

4.3.2.3 Analysis Approach

The forward +Z engines have the most severely scarfed nozzles of the engines whose plumes are of concern here (the outside engines in this cluster being scarfed the most). Dynamic pressure contours were generated and compared

for the standard unscarfed .RCS engine plume and the outside forward +Z
engine plume, Figure 4.3.2-3.

4.3.2.4 Analysis Results

The upper half of Figure 4.3.2-3 presents the dynamic pressure contours in
the standard unscarfed RCS engine plume and the lower half of the plot
presents the same information for the long side of the outside forward +Z
scarfed engine. Comparison of these contours indicates .that the effect on
the plume definition due to nozzle scarfing for these engines is minor,
and in turn the effect on the plume impingement results due to nozzle scarfing
is negligible. Since the nozzle scarfing for the $\pm Y$ engines (both forward
and aft.) is less severe than the long side of the forward +Z engines, the
effect on those plumes would be less pronounced than that presented in
Figure 4.3.2-3.

4.3.2.5 Preliminary Conclusions and Recommendations

Based on the above analysis, our conclusions and recommendations are:
*The effects on the plume flow field definition due to nozzle scarfing
  for the plumes (or partial plumes) of concern for payload deployment
  and retrieval should be neglected. A single plume definition based on
  the standard unscarfed RCS engine should be used for all the RCS engine
  plumes (scarfed and unscarfed) of interest here.
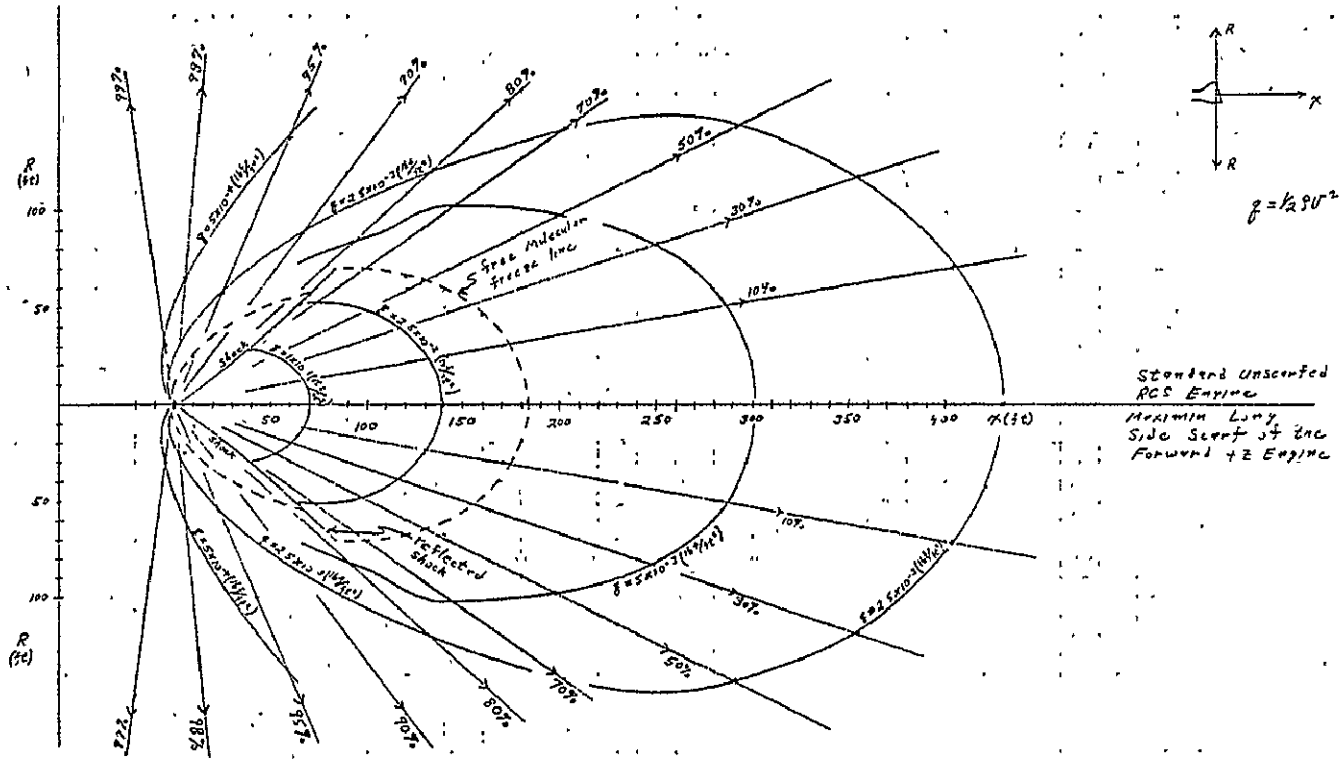
FIGURE 4.3.2-3 DYNAMIC PRESSURE (1bf/ft²) CONTOUR COMPARISONS FOR THE STANDARD RCS AND THE FORWARD SCARFED +Z ENGINE PLUMES.

4.3.3 Ambient Atmosphere Effects

4.3.3.1 The Question

Does the plume impingement model require a capability to account for high altitude ambient atmosphere effects? There are two topics related to this question: first, the interaction between an exhaust plume and the ambient atmosphere; second, the interaction between the ambient atmosphere and a payload.

Plume/atmosphere interaction: We are interested only in the orbital altitude range of 100 to 350 nautical miles (nm); 120 nm is considered "typical".

At these high altitudes the ambient air is streaming past the Orbiter and payload at an orbital speed of approximately 25 kfps; however, its density is so rarefied that its molecular mean free path, λ (which is inversely proportional to the air density, ρ) is very large. For example, at 120 nm, the air mean free path is greater than 1000 feet, as can be seen from Table 4.3.3-1, taken from Reference 20. Thus, the molecules of the air experience very few collisions (i.e., the atmosphere is in free-molecule flow) at this highly rarefied condition.

On the other hand, a rocket exhaust plume resulting from expanding into a vacuum environment may be considered as consisting of a continuum core, followed by a transition region and then by a large rarefied or free-molecule zone, as pictured in Figure 4.3.3-1. (Note that, in reality, the boundaries between these flowfield regimes are not sharp as shown; in fact, flowfield properties vary smoothly across these artificial boundaries.)

When the rarefied ambient atmosphere and the vacuum plume described above encounter each other at high speed, we would expect some kind of interaction

TABLE 4.3.3-1 ATMOSPHERE CHARACTERISTICS AND ORBITAL VELOCITY
FOR ALTITUDES OF INTEREST

ALTITUDE (h, nm)	AMBIENT ATMOSPHERE CHARACTERISTICS[a]		ORBITAL VELOCITY $(u_\infty,\ ft/sec)$
	MEAN FREE PATH $(\lambda,\ ft)$	DENSITY $(\rho,\ slug/ft^3)$	
100	475.1	9.77×10^{-13}	25043.0
120	1209.7	3.68×10^{-13}	24975.7
150	3875.0	1.07×10^{-13}	24875.5
200	18169.0	2.04×10^{-14}	24711.0
350	561680.0	5.24×10^{-16}	24236.5

[a] From Reference 20
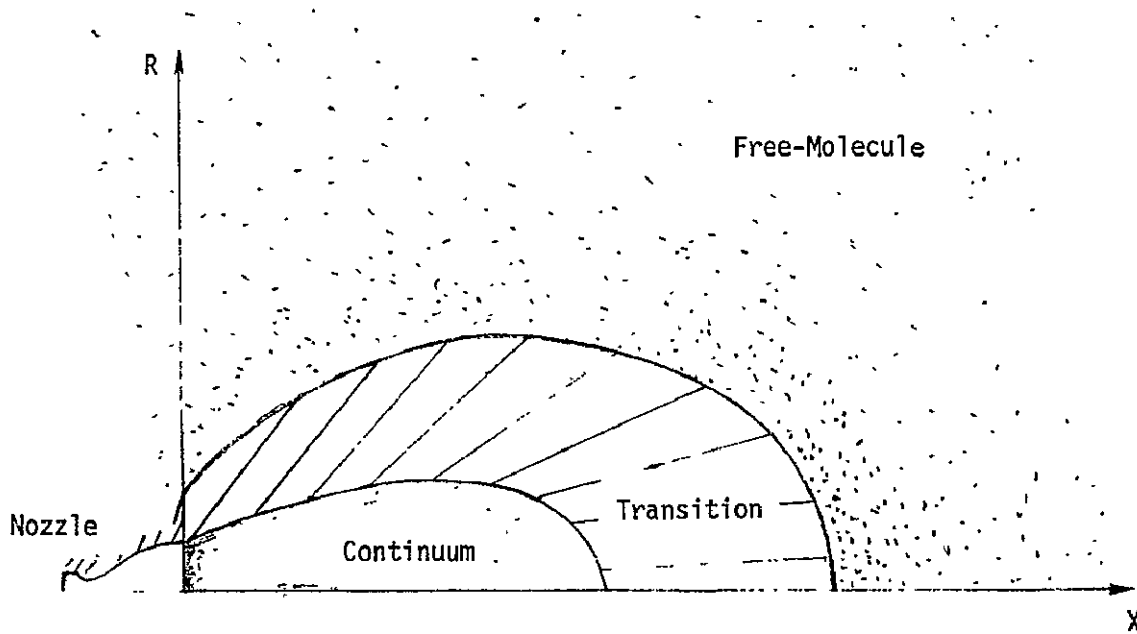
FIGURE 4.3.3-1 SKETCH OF FLOWFIELD REGIMES FOR
A ROCKET PLUME EXHAUSTING INTO
A VACUUM

to occur. We wish to determine whether this interaction distorts the plume flowfield as compared to the ".free-space" (vacuum expansion) form assumed in generation of the "standard" data of Section 4.3.

Atmosphere/payload interaction: When a payload is placed at close range to the vacuum plume, the dynamic pressure due to the plume is much greater than that of the ambient atmosphere. As the range is increased, the plume dynamic pressure falls off rapidly (roughly as $\frac{1}{r^2}$; see Section 4.3.1). Eventually the plume dynamic pressure will become "negligible" as compared to that of the ambient air.

Therefore, we could establish a criterion for a "practical boundary" of the plume: say, $q_{rcs} < 0.1\ q_{aero}$, where q_{rcs} and q_{aero} denote plume and air dynamic pressures, respectively. We wish to determine whether this "practical boundary" falls in the range of interest for the plume impingement model (35-1000 feet) or not.

4.3.3.2 Tradeoff Factors/Considerations

Implementation: If we establish that the plume distortion due to the ambient air is significant, modelling this effect will require offline computations of the plume distortion boundary, and then storing the boundary data in table/curve form, e.g., as functions of altitude, distance, and angle. Additional model inputs and logic would be required to establish the operational altitude and select the appropriate plume definition.

On the other hand, if we establish that the "practical boundary" from the dynamic pressure ratio falls in the range of interest, it can be implemented with a simple test, using parameters obtained from a fairly simple offline analysis.

"Cost" Factors: Even assuming that we could find or develop means for the required offline computation of plume distortion, the associated fixed cost would be difficult to estimate. In addition, the online modelling cost could be substantial.

On the other hand, implementing the "practical boundary" costs little in either offline or online modelling. It may actually save online computer time, since plume impingement computations are bypassed whenever the test fails.

Performance Factors: Plume distortion, if it exists, is only on the "windward" side of the plume. For most operations of current interest (e.g., nominal braking, R-bar, and V-bar approaches), the payload will usually be on the "leeward" side of the plume. Therefore, there seems to be little or no accuracy payoff from modelling plume distortion.

4.3.3.3 Analysis Approach

Based upon the above considerations and the fact that obtaining a quantitative assessment of the high altitude effects on the plume flowfield would require a substantial effort involving an analysis of two highly rarefied interacting gases, we decided that only a qualitative assessment of the interaction was warranted. To obtain such an assessment, we were led to conduct this part of study by consultation with experts in the field and a survey of the literature. At least a half dozen aerodynamicists were contacted, and a dozen related papers were identified and reviewed.

For the "practical boundary" we computed the ambient dynamic pressure, q_{aero}, at various altitudes, using the orbital speeds and atmospheric

densities shown in Table 4.3.3-1. Then we compared these dynamic pressures with the plume dynamic pressure generated by MDAC-West as reported in Section 4.3.

4.3.3.4 Analysis Results

Plume/atmosphere interaction: None of the plume experts we consulted had actually studied the problem in detail, but most of them were confident that the interaction is negligible (from the viewpoint of the plume being affected by the air). The same conclusion has also been reached from the literature survey.

The literature survey also uncovered an analysis of the effect of the plume upon the air at high altitudes. A rather complex technique available for computing this effect is reported in Reference 21; a physical picture of the interaction will be qualitatively described below.

With the vacuum plume sweeping at high orbital speed, the ambient air first encounters the outer portion of the plume. Since both the plume and air are highly rarefied, they pass through each other undergoing occasional collisions, without being disturbed much. As the ambient air penetrates further into the denser portion of the exhaust plume, the air stream is scattered by the exhaust gas, and some of the scattered air molecules will be deposited with and carried along by the gas. In the process the number density of the air is increased gradually as compared with the unscattered state, without affecting the plume.

Finally, as the air stream reaches the high density plume in the vicinity of the continuum core, the air molecules can no longer penetrate this region,

102

and are completely scattered by the denser gas. During the last stage of penetration the air number density peaks out and then drops off rapidly, while locally the plume density increases very slightly in the process.

In an example calculated for a plume at roughly 350 nm altitude, it was shown that the ambient air can penetrate deep into the plume, and that its density may increase by up to a factor of ten at high angles from the plume centerline, due to the plume scattering effect. However, even a ten-fold increase in the air density does not affect the plume at all in this case.

Atmosphere/payload interaction: Segments of the approximate dynamic pressure equivalence boundaries (dynamic pressure ratio $q_{rcs}/q_{aero} = 1$, using the MDAC-West dynamic pressure) for several altitudes are presented in Figure 4.3.3-2. Note that no plume effect on the air is accounted for in this plot. It seems clear that if a "practical boundary" is defined at a dynamic pressure ratio of 0.1, then this boundary will fall within the distance range of interest for altitudes of interest.

4.3.3.5 Preliminary Conclusions and Recommendations

From the above analysis, we conclude that: (a) plume distortion by the rarefied atmosphere is negligible, (b) the air dynamic pressure becomes comparable to the plume dynamic pressure for altitudes and distances of interest.

Therefore, we do not recommend implementation of a plume distortion computation, but do recommend implementation of the "practical boundary" test in the plume impingement model.

Ambient Air Dynamic Pressure : $q_{aero} = 1/2 \rho u_\infty^2$

ALTITUDE, h, (NM)	DYNAMIC PRESSURE, q, (lb/ft^2)
100	3.06×10^{-4}
120	1.15×10^{-4}
150	3.32×10^{-5}
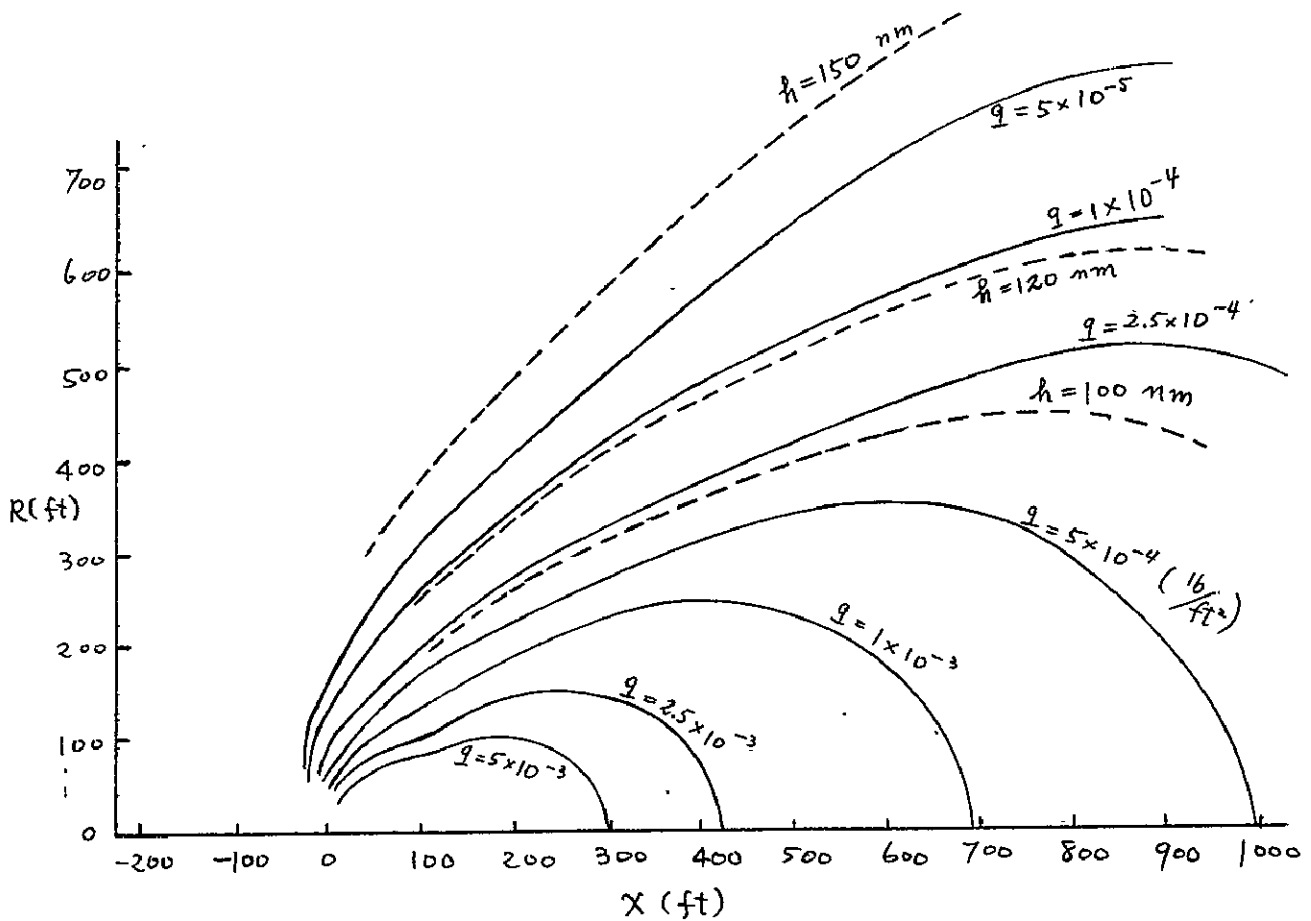
FIGURE 4.3.3-2   LINES OF APPROXIMATE DYNAMIC PRESSURE
EQUIVALENCE BETWEEN AMBIENT AIR AND RCS
PLUME (USING MDAC-WEST DATA)

104

4.3.4 Multiple Simultaneous Firings

4.3.4.1 The Question

What is the best method of handling multiple simultaneous engine operation? This question must be answered for: (1) simultaneous operation of adjacent engines (same cluster) and (2) simultaneous operation of separated engines (different clusters). The word "cluster" is used here to indicate engines in the same pod which fire in the same direction.

The alternatives are:

- Considering each engine independently of the other and simply summing their effects.
- Using a special technique to account for the interaction of the multiple plumes.

Before this question can be answered, an understanding of the plume interaction structure is necessary.

Simultaneous Operation of Adjacent Engines: Figure 4.3.4-1 depicts the flow structure created when two adjacent RCS engines are operated simultaneously. As the adjacent plumes intersect, a slip line (or plane) is formed midway between the engines. This plane acts as a solid boundary to the interacting plumes. Since the flow must turn to become parallel to the slip plane, an interaction shock wave is formed in each plume. This shock strength dissipates with increasing distance from the nozzle exit because the flow turns less, the greater the distance from the nozzle exit. In a relatively short distance (much less than the minimum distance from the engine exit to the affected body), the interaction shocks approach the respective plume centerlines and dissipate completely. After the shocks have dissipated, the plume structure from the two adjacent plumes is more accurately represented by a plume from a single "equivalent" engine located midway between the single engines. The "equivalent" engine is a scaled up version of the single engine to render the same mass flow as the two single engines operating simultaneously.

SKETCH NOT TO SCALE

INTERACTION SHOCK

SLIP PLANE

EQUIVALENT ENGINE PLUME BOUNDARY

SINGLE ENGINE PLUME BOUNDARY

SINGLE ENGINE

SINGLE ENGINE
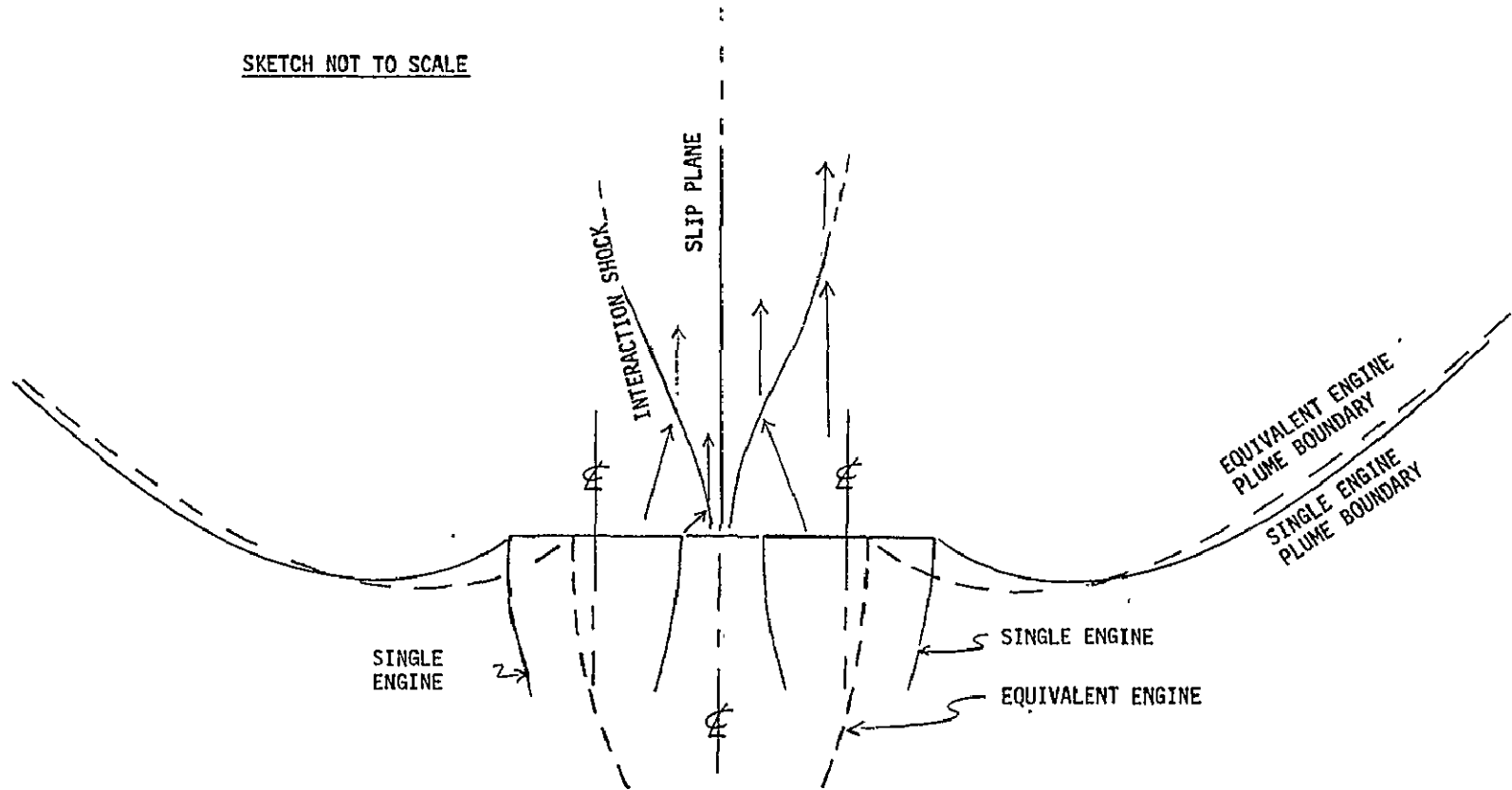
EQUIVALENT ENGINE

FIGURE 4.3.4-1   MULTIPLE ENGINE PLUME INTERACTION CHARACTERISTICS AND EQUIVALENT ENGINE PLUME

Simultaneous Operation of Separated Engines: For the separated engines two
potential plume interaction situations must be considered: (1) interaction
between the up firing (+Z) engine plumes in the forward and aft pods and
(2) interaction between the up firing (+Z) engine plumes in the left and
right aft pods. The plumes from the (+Z) engines in the left and right
·aft pods will not interact because of vehicle geometry. The tail effectively
blocks these plumes before they can interact. The plumes from the +Z engines
in the forward and aft pods will interact. The interaction takes place at
large enough distances from the engine exits that the plume flow fields are
free molecular in nature; therefore, the existence of one plume will not
affect the other.

4.3.4.2 Tradeoff Factors/Considerations

To assess tradeoff factors, the frequency of simultaneous engine operation
must be considered. The frequency of simultaneous engine operation depends
on the type and number of maneuvers requiring multiple engine operation,
and is difficult to evaluate at this time. Therefore, frequency of multiple
engine operation must be considered at a later date. To assess cost and
performance factors, consideration of how simultaneous engine operation would
be implemented in the model is necessary.

Implementation: Since the plumes resulting from simultaneous operation of
two adjacent engines can be represented by a single "equivalent" engine, only
a single plume flow field need be considered when calculating the multiple
plume effects. The "equivalent" engine operating and geometric characteristics
are identical to the single RCS engine except the "equivalent" engine is $\sqrt{2}$
larger to obtain the same mass flow as the two single engines operating simul-
taneously.* This eliminates the necessity of generating and storing an addi-
tional plume definition for simultaneous engine operation; a simple scaling
of the single engine plume is all that is required.

To implement the "equivalent" engine to simulate adjacent simultaneous oper-
ation, additional logic would be required to determine whether the operational
engines are adjacent or separated. If the engines are adjacent, then the
"equivalent" engine plumes would be used. If the engines are separated, then
each plume would be considered independently and their effects summed.

*The $\sqrt{2}$ renders the "equivalent" engine exit area equal to the sum of the two
single engine exit areas.

A second alternative in implementing simultaneous adjacent engine operation is to consider each plume independently and sum the results. This technique would eliminate the requirement of additional logic to test whether the engines operational are adjacent.

"Cost" Factors: If a single "equivalent" engine plume is used to represent the two adjacent engine plumes, the calculation time to establish the plume effects is of the order of half the time required to establish the plume effects from each adjacent engine. The additional logic necessary to implement the "equivalent" engine simulation is minimal in comparison to the total plume effects computation time; therefore, substantial savings may be realized if simultaneous firing of adjacent engines occurs frequently.

For the case of separated engines, no savings in computational time or storage costs can be realized since each plume and its effects must be considered separately.

Performance Factors: The plume flow field structure resulting from simultaneous operation of adjacent engines is represented quite accurately in the region of interest here by the "equivalent" engine plume (see Figure 4.3.4-1). However, since the spacing of the adjacent Space Shuttle RCS engines is only a few inches, the error induced in neglecting the multiple-plume interaction and simply summing the results from each is minimal.

4.3.4.3 Analysis Approach

Dynamic pressure contours and the free molecular freeze locations in a single engine plume and in an "equivalent" engine plume were generated and compared; see Figure 4.3.4-2. The dynamic pressure contours are typical; other plume flow field variables (Mach number, pressure, density, etc.) can be compared in a like manner.

4.3.4.4 Analysis Results

The $\sqrt{2}$ scale factor relating the single engine plume and the "equivalent" engine plume can be verified from the dynamic pressure contours in Figure 4.3.4-2.
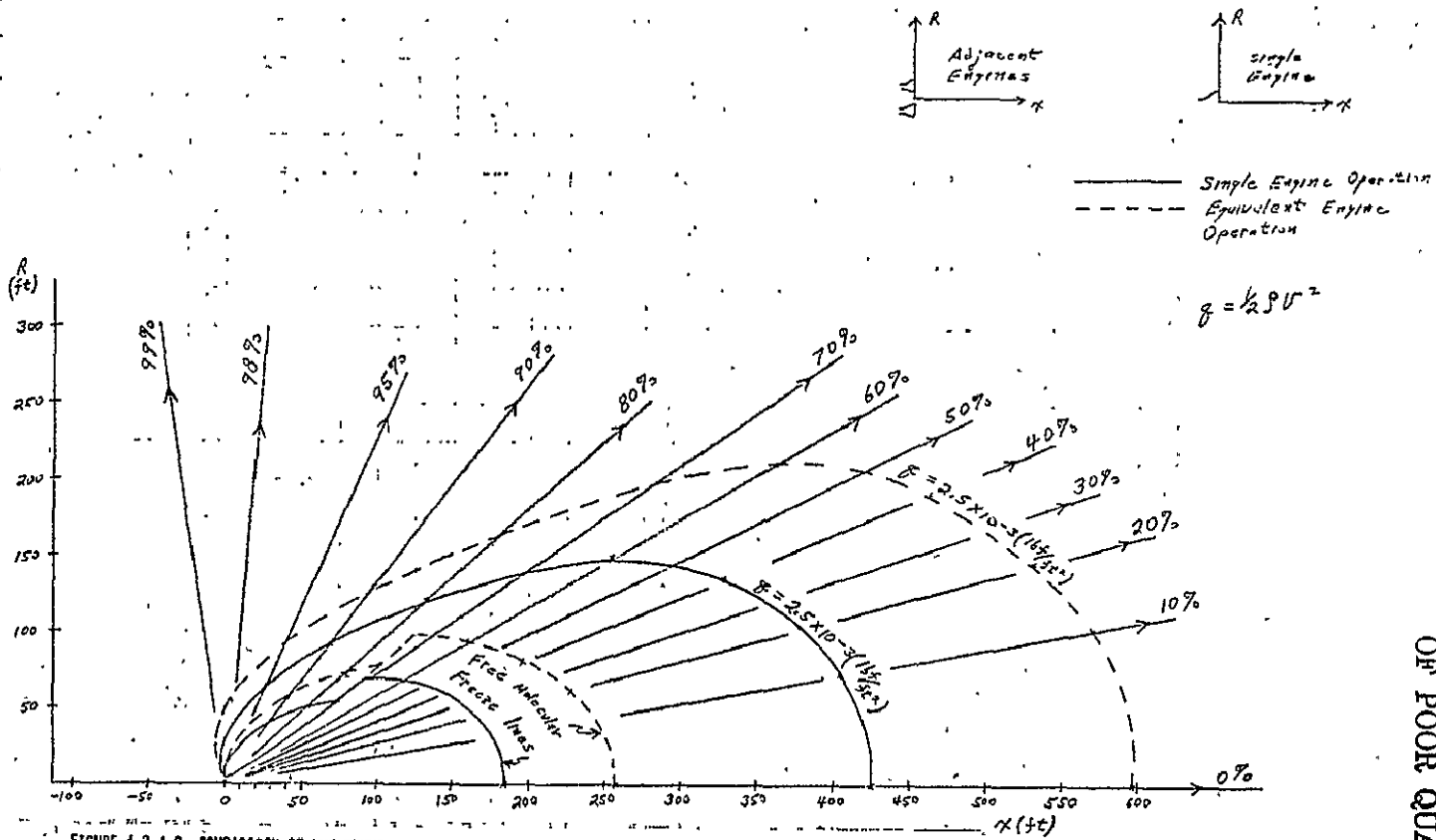
FIGURE 4.3.4-2 COMPARISON OF THE PLUMES RESULTING FROM SINGLE AND TWO ADJACENT ENGINE OPERATION

This scale factor is typical for all plume flow field variables (Mach number, pressure, density, etc.).

4.3.4.5 Preliminary Conclusions and Recommendations

Based on the above analysis, our conclusions and ·recommendations are:

- If simultaneous adjacent engine operation occurs frequently, the calculation of the plume effects utilizing an "equivalent" engine is recommended. If simultaneous adjacent engine operation occurs very infrequently, then calculation of the plume effects from each engine independently of the other and summing the results is recommended.

- During simultaneous operation of separated engines, the calculation of the plume effects from each· engine independently of the other and summing the results is recommended.

4.4 IMPINGEMENT PRESSURE MODELLING

This section deals with alternative formulations of the plume impingement pressure module, IMPRES. The IMPRES module calculates the local normal and tangential plume impingement pressure coefficients, which are used to define the plume-induced forces and moments on the payloads.

As described in Section 4.3, the exhaust plume at orbital altitudes will be highly expanded. In the far field of the plume, the flow will become highly rarefied; i.e., the fluid does not behave as a continuous fluid (continuum gas dynamics) but rather exhibits characteristics of its molecular structure (rarefied flow).

When the low density portion of the plume impinges the surface of a payload, consideration of the ratio of the molecular mean free path in the plume, λ_∞, to a characteristic dimension of the impinged surface, L_s, is necessary. This dimensionless ratio is the Knudsen number of the impinged surface, K_{ns}.

The Knudsen number in terms of familiar parameters of fluid mechanics is derived in Section 4.3 and will not be repeated here. The Knudsen number used to define the degree of rarefication of the plume impingement mechanism on the surface is:

$$K_{ns} = \frac{\lambda_\infty}{L_s} = \sqrt{\frac{\gamma_\infty \pi}{2}} \cdot \frac{M_\infty}{R_e} \qquad (4.4-1)$$

where

$$R_e = \frac{\rho_\infty U_\infty L_s}{\mu_\infty}$$

and $M_\infty = \frac{U_\infty}{a_\infty}$

111

Rarefied flow techniques must be employed when the impingement Knudsen number becomes larger than about 0.01. The mechanism by which the impingement pressures are calculated is divided into three impingement regimes depending on the degree of rarefaction (i.e. the impingement Knudsen number). The impingement regimes, in general, are defined as:

$$0 \leq K_{ns} < 0.01 \quad \text{continuum impingement}$$
$$0.01 \leq K_{ns} < 10.0 \quad \text{transitional impingement}$$
$$10.0 \leq K_{ns} < \infty \quad \text{free molecular impingement}$$

Figure 4.4-1 presents these impingement regimes for a 10 foot payload surface (i.e. L_s = 10 ft.) in the RCS plume. Impingement regimes for any size payload surface in the RCS plume can be obtained from Figure 4.4-1 utilizing the definition of the impingement Knudsen number and the impingement regimes defined above.

Each impingement mechanism is discussed separately in Sections 4.4.1, 4.4.3, and 4.4.2 respectively. Basically, in the continuum regime the impinging flow behaves as a continuous fluid; in the transitional regime the flow is only moderately rarefied, so that the molecules being reflected from the surface affect the oncoming molecules; and in the free molecular regime the flow is highly rarefied to the point that the molecules are so far apart that the reflected molecules do not affect the oncoming molecules to any appreciable degree.

113

R
(ft)

600 —
550 —
500 —
450 —
400 —
350 —
300 —
250 —
200 —
150 —
100 —
50 —

75°

50°

Free Molecular
Impingement for
Regime Kns ≳ 10.0

Continuum
Impingement
Regime for
Kns < 0.01

Transitional
Impingement for
Regime
0.01 ≲ Kns < 10.0

0°

-200 -150 -100 -50   0   50 100 150 200 250 300 350 400 450 500 550 600 650 700 750 800 850 900 950 1000 1050 1100 1150 1200 1250 1300

X(ft)
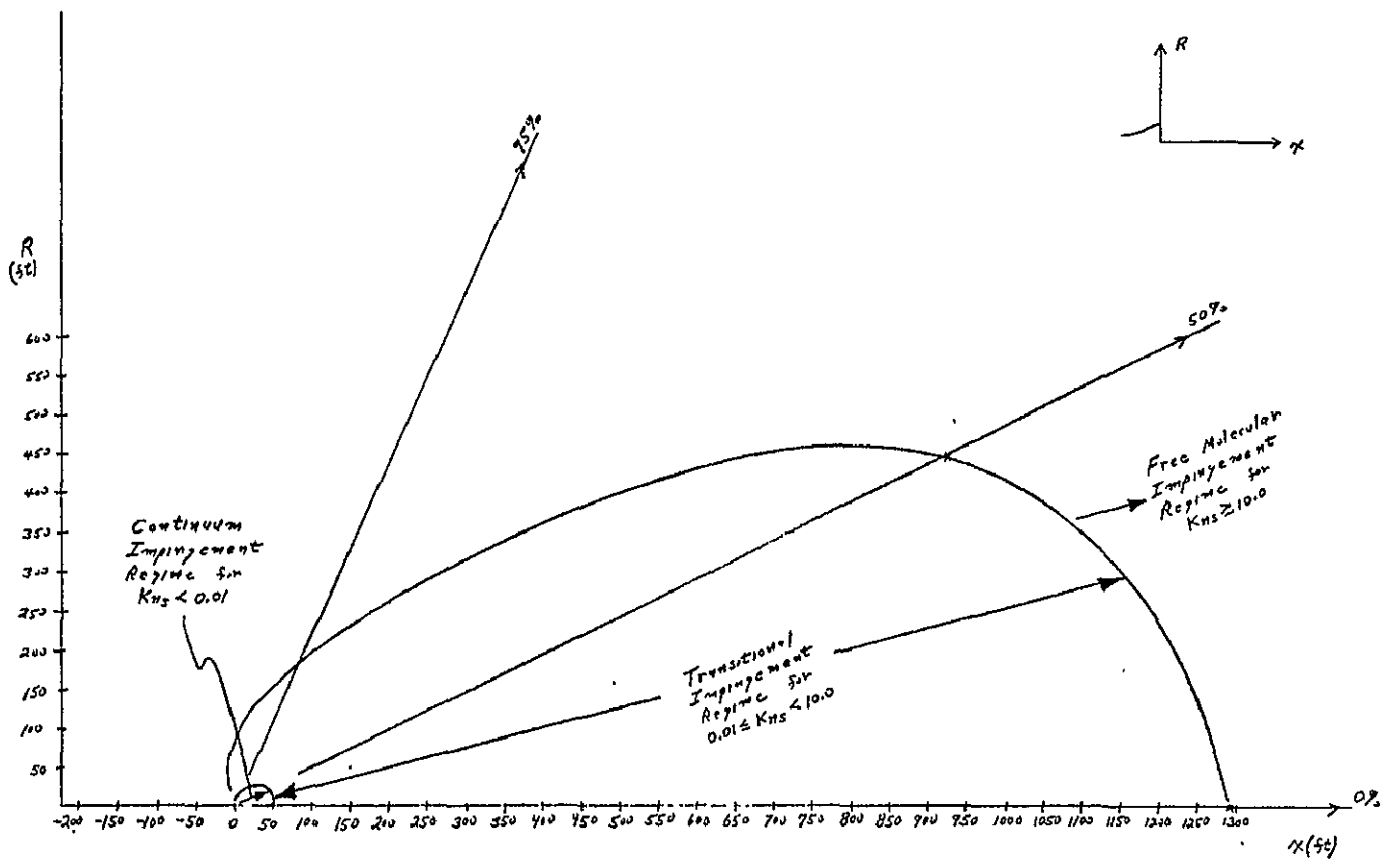
FIGURE 4.4-1   IMPINGEMENT REGIMES FOR A 10 FOOT PAYLOAD SURFACE IN THE RCS ENGINE PLUME.

4.4.1 Impingement Pressure: Continuum-Flow Regime

4.4.1.1 The Question

What impingement pressure formulations are required in continuum-flow regime? For an "elemental flat plate" (see Section 4.2.2), the most commonly used formulations of impingement pressure (normal force per unit area) in this regime are newtonian impact, modified newtonian and oblique shock/tangent wedge.

Newtonian Impact: For newtonian flow, it is assumed that the normal component of momentum is transferred to the plate, while the tangential component remains unchanged. The pressure coefficient is expressed simply as

$$C_p = 2 \sin^2\alpha \qquad\qquad (4.4.1-1)$$

where α is the impingement angle shown in Figure 4.4.1-1.

Modified Newtonian: Various empirical modifications to Equation 4.4.1-1 have been suggested, to account for the higher pressures noted experimentally at small local impingement angles. The pressure coefficient is expressed as

$$C_p = K \sin^2\alpha \qquad\qquad (4.4.1-2)$$

using a curve fit; e.g.,

$$K = C_{p_0} [0.814 + \frac{6.88}{\alpha^{0.8}}] \qquad\qquad (4.4.1-3)$$

where α is expressed in degrees, and C_{p_0} is the "stagnation pressure coefficient".

At least three variations of the modified newtonian formulation are in use, differing in their treatment of the stagnation pressure coefficient:

114
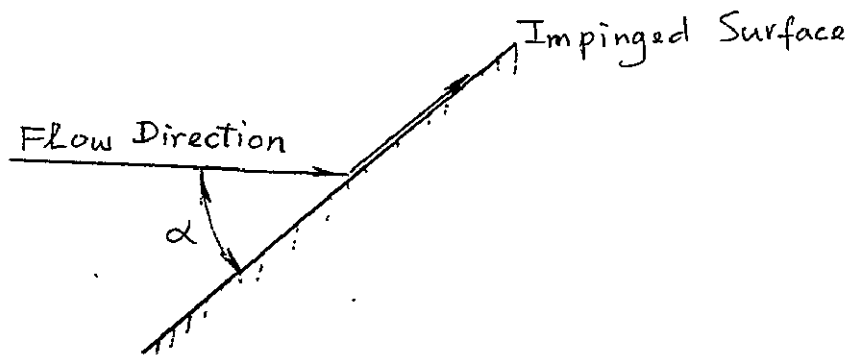
FIGURE 4.4.1-1   LOCAL IMPINGEMENT ANGLE AT SURFACE ELEMENT
AND CHANGE IN FLOW DIRECTION FOR NEWTONIAN FLOW

$$K = 1.83 \left(0.814 + \frac{6.88}{\alpha^{0.8}} \right) \quad \alpha \geq 3°$$

$$K = 6 \qquad\qquad\qquad \alpha < 3°$$
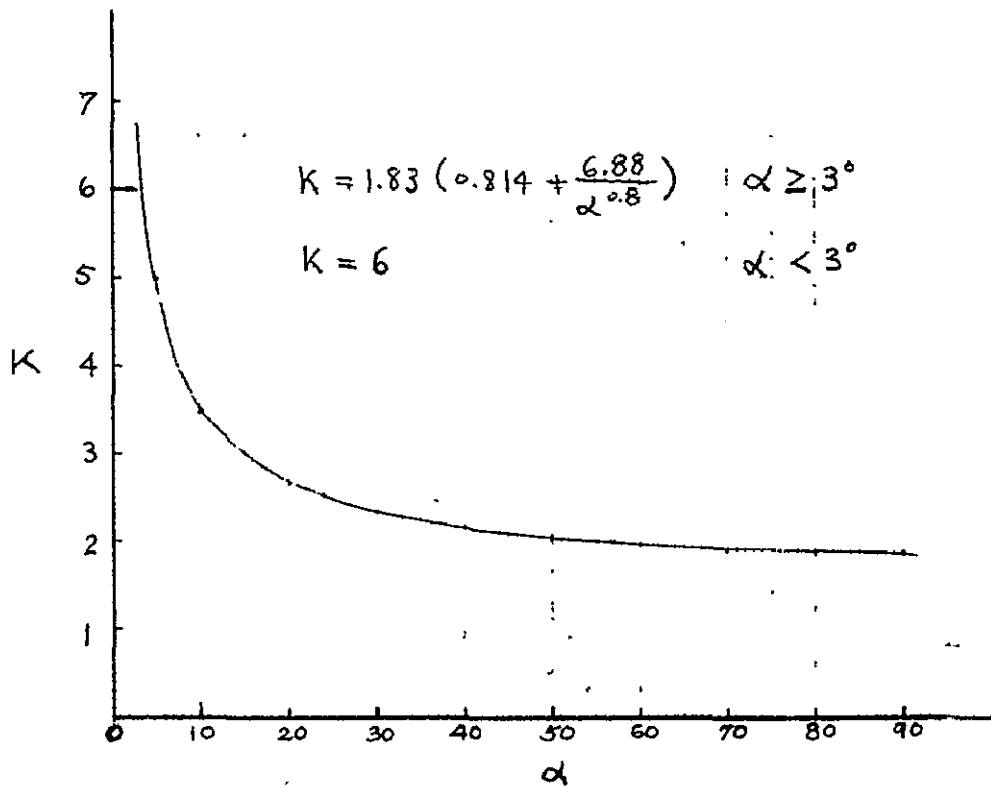
FIGURE 4.4.1-2   IMPINGEMENT CORRECTION FACTOR
VS LOCAL IMPINGEMENT ANGLE
IN MODIFIED NEWTONIAN FORMULATION
AS USED IN "PLIMP" (ASSUMING $C_{p_0} = 1.83$)

115

- Assume a constant (newtonian) value, $C_{p_0} = 2$.

- Assume a constant, empirically-determined value; e.g., $C_{p_0} = 1.83$.

- Compute C_{p_0} from the definition,

$$C_{p_0} = \frac{p_0 - p_\infty}{q_\infty} \qquad (4.4.1\text{-}4)$$

where p_0 is the stagnation pressure (behind a normal shock), p_∞ is the free-stream static pressure, and q_∞ is the free-. stream dynamic pressure.

Variation of the modified newtonian pressure coefficient with impingement angle is shown in Figure 4.4.1-2, assuming $C_{p_0} = 1.83$. This curve was taken from PLIMP (Section 3.2.4) documentation.

Oblique Shock/Tangent Wedge: In this method, the impingement pressure is assumed to be the same as that existing behind an attached oblique shock through which the oncoming flow turns parallel to the elemental area. The pressure coefficient is

$$C_p = \frac{4}{M_\infty^2(\gamma+1)} [M_\infty^2 \sin^2\beta - 1] \qquad (4.4.1\text{-}5)$$

where

$$\tan \alpha = 2\cot\beta \left[\frac{M_\infty^2 \sin^2\beta - 1}{M_\infty^2(\gamma+\cos2\beta)+2} \right] \qquad (4.4.1\text{-}6)$$

is solved by iteration. A sketch of the oblique shock wave with various parameters is shown in Figure 4.4.1-3.
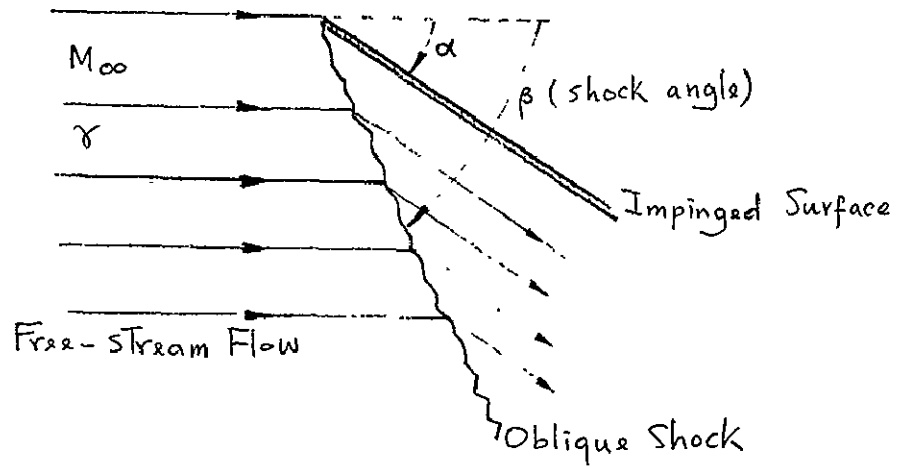
FIGURE 4.4.1-3   PARAMETERS IN THE OBLIQUE
                 SHOCK IMPINGEMENT FORMULATION

117

4.4.1.2 Tradeoff Factors/Considerations

Implementation: Implementation of the newtonian impact formulation is obvious and straightforward. Implementation of the modified newtonian formulation is also straightforward, if a constant C_{p_0} is assumed. To compute C_{p_0} from its definition (Equation 4.4.1-4) will require computation of p_0 as a function of γ and M_∞, using a small table lookup and standard equations which account for the entropy change across a normal shock. This is the approach used in PLIMP. Implementation of the oblique shock formulation requires tabular data for γ and M_∞ throughout the flowfield, as well as an iteration scheme to solve Equation 4.4.1-6.

"Cost" Factors: It is apparent that the newtonian impact theory gives the simplest pressure coefficient form, while the oblique shock method is the most complex. We would expect the computer storage and execution time requirements to be proportional to the complexity of each formulation; iterations may prove very time-consuming.

Performance Factors: Although the newtonian impact pressure is the simplest to implement, its accuracy is typically the worst of the three methods considered. The oblique shock and modified newtonian methods are comparable in accuracy; within their common domain; see Figure 4.4.1-4 for representative flat-plate data. However, the oblique shock method is applicable only to impingement angles less than (approximately) $45°$; the exact limiting angle depends upon the local flowfield properties. Beyond this limiting angle, the weak, attached oblique shock becomes a strong detached shock. Correspondingly, Equation 4.4.1-6 has no solution, so one of the newtonian formulations must be used. (The switchover to an alternate formulation must, of course, be automatically performed on a per-element basis, as it is in PLIMP.)

The only method which has the advantage of newtonian impact simplicity
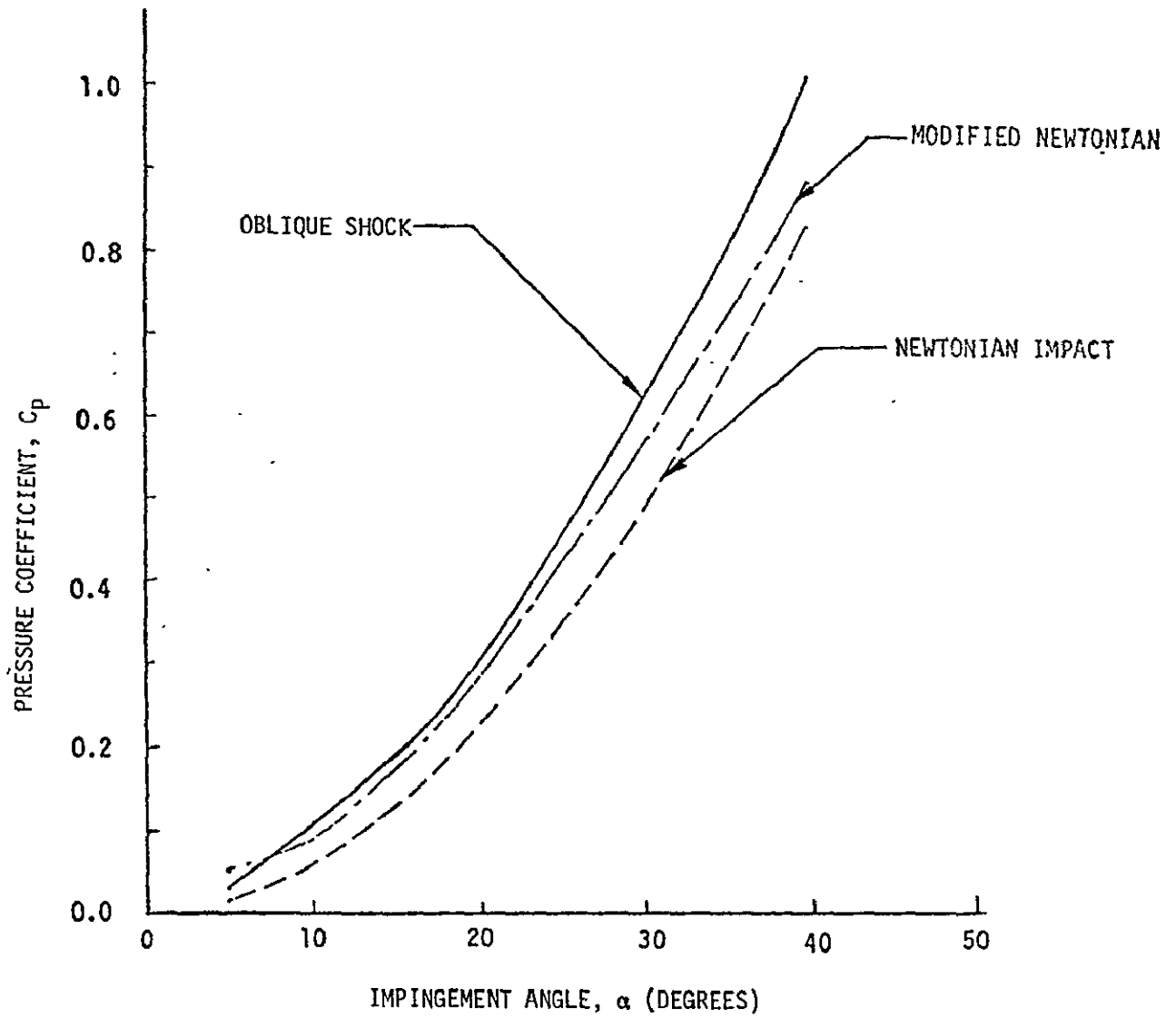
FIGURE 4.4.1-4   COMPARATIVE DATA FOR DIFFERENT IMPINGEMENT
FORMULATIONS (FLAT PLATE WITH ATTACHED
SHOCK: $M_\infty = 15, \Upsilon = 1.4$)

and an expected accuracy comparable to the oblique shock method is the modified newtonian formulation. Therefore this formulation is considered most suitable for the plume impingement model.

4.4.1.3 Analysis Approach

To evaluate the performance of various plume impingement pressure formulations, a number of runs of PLIMP were made for both MMS/SMM and LDEF payloads (Section 3.2.2), for various orientations at an on-centerline distance of 100 ft. For all data runs, a mesh size of 30 x 30 (Section 4.2.2) was used and object shadowing (Section 4.2.3) was modelled.

4.4.1.4 Analysis Results

Table 4.4.1-1 provides case-by-case cost and performance data. Note that significantly more computer time (roughly a factor of 4) is required for the oblique shock method. The computer time required by both newtonian formulations is comparable and much less than that of the oblique shock formulation.

In general, the oblique shock and the modified newtonian formulations are comparable in accuracy. An exception is case L2, where both newtonian methods deviate greatly from the oblique shock result in the moment calculation, although the forces are accurate. This is because at this orientation, most of the force is contributed by the circular end plate, while most of the moment comes from the cylinder body. Since the impingement angle on the end plate is roughly 70°, the oblique shock option defaults to modified newtonian. On the cylinder body, the impingement angle ranges from 20° to grazing incidence; the greatest deviations occur for those elements immediately neighboring the shadow line.

<div align="center">

TABLE 4.4.1-1 COST AND PERFORMANCE VARIABLES FOR VARIOUS IMPINGEMENT
PRESSURE FORMULATIONS IN THE CONTINUUM FLOW RÉGIME

</div>

TEST CASE			IMPINGEMENT PRESSURE[b]	COST DATA		RAW PERFORMANCE DATA			SENSITIVITY[c]		
									Force Errors		Moment Error (±%)
Number[a]	d (ft)	θ (deg)		Execution Time (Sec)	Time Ratio[c]	F_x (lb)	F_y (lb)	M_z (lb-ft)	Δ Mag (±%)	Δ Dir (± deg)	
M1	100	20	OS	277.0	-	16.71	5.52	-17.08	-	-	-
			MN	69.5	0.25	16.77	5.36	-16.81	0.04	0.56	1.58
M2	100	70	OS	314.6	-	5.35	0.14	-14.19	-	-	-
			MN	69.6	0.22	5.50	0.54	-16.34	3.23	4.04	16.2
L1	100	0	OS	131.3	-	21.37	0.0	0.0	-	-	-
			MN	48.7	0.37	21.37	0.0	0.0	0.00	0.00	-
			NI	46.8	0.36	21.76	0.0	0.0	1.82	0.00	-
L2	100	20	OS	206.9	-	18.47	3.76	4.18	-	-	-
			MN	56.4	0.27	18.81	2.84	6.08	0.93	2.92	45.5
			NI	42.8	0.21	17.74	3.94	2.80	3.59	1.02	33.0
L3	100	70	OS	252.4	-	27.53	-9.13	29.67	-	-	-
			MN	40.3	0.16	27.71	-8.80	29.44	0.24	0.73	0.78
			NI	26.5	0.11	25.52	-8.54	30.08	7.22	0.16	1.38
L4	100	90	OS	115.1	-	32.34	0.0	0.0	-	-	-
			MN	33.4	0.29	32.47	0.0	0.0	0.40	0.0	-
			NI	27.2	0.24	30.86	0.0	0.0	4.58	0.0	-

NOTES:

[a] M denotes MMS/SMM; L denotes LDEF

[b] OS denotes Oblique Shock
MN denotes Modified Newtonian
NI denotes Newtonian Impact

[c] With respect to the Oblique Shock result

Geometry:
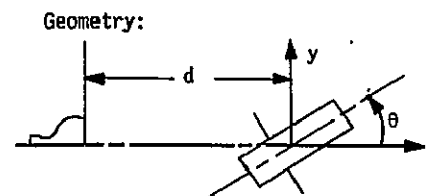
4.4.1.5 Preliminary Conclusions and Recommendations

Based upon the above analysis and results, the modified newtonian formulation exhibits the anticipated best compromise between cost and accuracy. Therefore this formulation is recommended for the plume impingement model in the continuum-flow regime.

4.4.2 Impingement Pressure: Free Molecule Flow Regime

4.4.2.1 The Question

What impingement pressure formulations are required in the free-molecule-flow regime? For an "elemental flat plate" (see Section 4.2.2), the formulations of impingement pressure which are usually recommended for the free molecule flow regime are newtonian impact, diffuse reflection, and thermal accommodation.

Newtonian Impact: For newtonian flow, it is assumed that the normal component of momentum is transferred to the plate, while the tangential component remains unchanged. The normal and tangential pressure coefficients are simply:

$$C_{PN} = 2 \sin^2 \theta \qquad (4.4.2\text{-}1)$$

$$C_{PT} = 0 \qquad (4.4.2\text{-}2)$$

where θ is the impingement angle shown in Figure 4.4.2-1 (a).

Diffuse Reflection: Given a stream of incident gas particles, all moving with a constant velocity, diffuse reflection occurs when each particle hits the plate and is reflected with unchanged energy in a random direction; see Figure 4.4.2-1 (b). The coefficients of pressure are calculated in Reference 22 as

$$C_{PN} = 2 \sin\theta \left[\sin\theta + \frac{2}{\pi} \right] \qquad (4.4.2\text{-}3)$$

$$C_{PT} = 2 \sin\theta \cos\theta \qquad (4.4.2\text{-}4)$$

Thermal Accommodation: A rarified gas travels with a stream velocity, $\bar{c}$, upon which is superimposed a Maxwellian velocity distribution (Reference 23) determined from the temperature of the incident gas, T_i. Since the motions of the incident gas and the gas reflected from the surface are assumed independent (i.e., no collisions), the momentum and energy of the reflected gas will not be affected by the presence of the incident particles (see Figure 4.4.2-1 (c)).
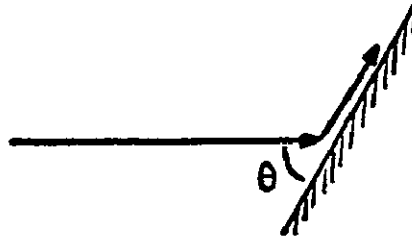
(a) NEWTONIAN IMPACT
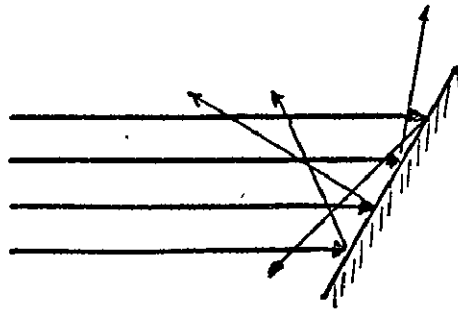
(b). DIFFUSE REFLECTION
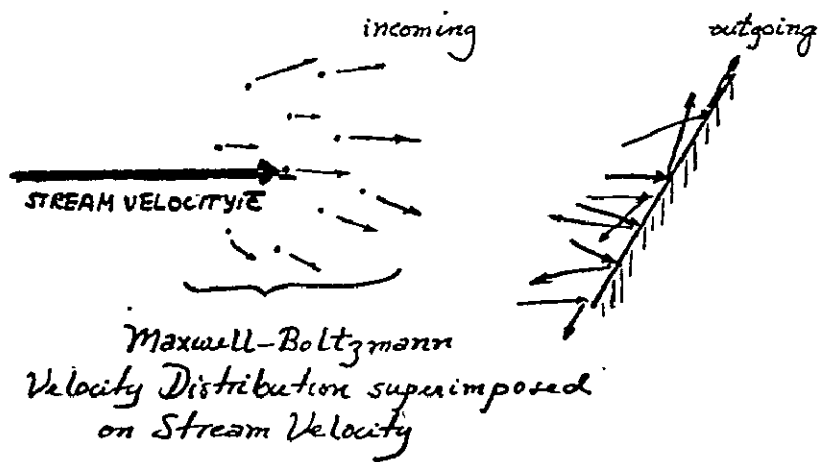
(c) THERMAL ACCOMMODATION

FIGURE 4.4.2-1   FREE MOLECULE FLOW IMPINGEMENT FORMULATIONS

At the payload surface, incident particles undergo collisions with the wall molecules. With each collision the particles are deflected by, and exchange energy with, the wall. The momentum and energy of the particles leaving the surface can then be defined in terms of two momentum coefficients (σ_s, σ_d) and one energy coefficient (α):

specular accommodation coefficient: $\sigma_s = \dfrac{P_i - P_r}{P_i - P_w}$

diffuse accommodation coefficient: $\sigma_D = \dfrac{\tau_i - \tau_r}{\tau_i - \tau_w}$

(4.4.2-5)

thermal accommodation coefficient: $\alpha = \dfrac{E_i - E_r}{E_i - E_w}$

where

τ_i, P_i = tangential and normal momenta of the incident molecules

τ_r, P_r = tangential and normal momenta of the reflected molecules

τ_w, P_w = tangential and normal momenta of the wall molecules

E_i, E_r, E_w = energy of the incident, reflected, and wall molecules.

At the wall, only a few collisions of each incident molecule while trapped within the interstices of the wall are necessary to produce completely random emission. However, a much larger number of such encounters is necessary to adjust the energy of the incident molecules so that they emerge at a temperature consistent with the thermal condition of the wall. Experimental data (Reference 11) suggests $\sigma_d = \sigma_s = 1$ and $0.8 < \alpha < 1.0$. In subsequent calculations, we assume $\sigma_d = \sigma_s = 1$; i.e., the reflected gas leaves randomly from the wall.

Given the molecule mass (m), the stream speed $(\bar{c})$, and Boltzmann's constant (k), one can find the molecular speed ratios (S and S_v):

$$S = \bar{c} / \left(\frac{2kT_i}{m} \right)^{1/2}$$

(4.4.2-6)

$$S_v = S \sin\theta$$

(4.4.2-7)

The reflected kinetic temperature (T_r) is then found to be:

$$T_r = \frac{T_i}{2} \left[\frac{S_v}{\sqrt{\pi}} e^{-S_v^2} + (2 + S^2)(1 + erf\, S_v) \right] (1 - \alpha) + \alpha T_w$$

(4.4.2-8)

125

and the pressure coefficients are:

$$C_{PN} = \sin^2\Theta \left\{ \frac{1}{S_V}\left(\frac{1}{\sqrt{\pi}} + \frac{1}{2S_V}\sqrt{\frac{T_r}{T_i}}\right)e^{-S_V^2} + \left(1 + \frac{1}{2S_V^2} + \frac{\sqrt{\pi}}{2S_V}\sqrt{\frac{T_r}{T_i}}\right)\left(1 + erf\{S_V\}\right) \right\}$$ (4.4.2-9)

$$C_{PT} = \sin\Theta\cos\Theta \left\{ \frac{e^{-S_V^2}}{\sqrt{\pi}S_V} + 1 + erf\{S_V\} \right\}$$ (4.4.2-10)

where "erf S_V" is the error function of S_V.

When the molecular speed ratio, S, is large, as it normally is in the free-molecule region of a rocket exhaust plume, the preceding equations can be greatly simplified for most impingement angles. In our situation, S will always be greater than ten; so, for angles greater than twelve degrees, S_V will be greater than two. It is then a good approximation to let the error function equal one (erf 2 = .995) and the exponential equal zero $(e^{-4} = .02)$. With these approximations, the simplified equations are:

$$T_r = T_i (2 + S^2)(1 - \alpha) + \alpha T_w$$ (4.4.2-8a)

$$C_{PN} = 2\sin^2\Theta \left(1 + \frac{1}{2S_V^2} + \frac{\sqrt{\pi}}{2S_V}\sqrt{\frac{T_r}{T_i}}\right)$$ (4.4.2-9a)

$$C_{PT} = 2\sin\Theta\cos\Theta$$ (4.4.2-10a)

Even further simplifications may be reasonable under certain conditions; in fact, for S_V large enough, Equation 4.4.2-9a reduces to simple newtonian impact (Equation 4.4.2-1).

4.4.2.2 Tradeoff Factors/Considerations

Implementation: Implementations of the newtonian impact and diffuse re-flection formulations are obvious and straightforward. Implementation of the full thermal accommodation formulation requires a subroutine to evaluate the error function, and tests for singularities in evaluating

126

the pressure coefficients.

"Cost" Factors: Newtonian impact theory and diffuse reflection analysis provide the simplest pressure coefficient forms, while the thermal accommodation technique requires somewhat larger computer storage and longer execution times. Using the thermal accommodation technique may require a table of incident gas temperatures in various regions of the plume (depending upon the temperature sensitivity of the pressure coefficients).

Performance Factors: The newtonian impact pressure coefficients are simple in form, but the normal force coefficient is not expected to be very accurate, and the tangential force coefficient is zero.

Classical elastic collisions (treating the gas molecules as hard spheres) causing specular and diffuse reflection are often suggested as a mechanism for imparting forces to a surface. However, the conditions for these elastic interactions are not satisfied for a fast moving plume gas and a typical payload surface (Reference 23).

The thermal accommodation pressure coefficients are complex but include much of the physics of the gas. Further, the thermal accommodation technique allows for a "pseudo-diffuse" case when the accommodation coefficient (α) is zero. In this case, the energy of the gas is constant throughout the interaction and particles leave in random directions from the surface. In the degenerate case where the molecular speed ratio (S) becomes infinite, the particles travelling to the surface all have a uniform speed. Unlike classical diffuse reflection, though, the reflected particles are distributed according to a Maxwell-Boltzmann distribution.

At the other extreme, $\alpha = 1$, the particles leave the wall with a velocity distribution characterized by the wall temperature. Again, experimental data suggests $0.8 < \alpha < 1.0$.

The thermal accommodation technique is expected to give the best performance, in terms of accuracy and generality.

4.4.2.3 Analysis Approach

. The various free-molecule flow impingement pressure formulations were coded on the HP-9825 desk calculator, and a number of plot runs were made to compare the pressure coefficients as functions of impingement angle.

Sensitivities of these coefficients to the input parameters were also analyzed.

4.4.2.4 Analysis Results

Figure 4.4.2-2 shows the normal pressure coefficient as a function of impingement angle for various accommodation coefficient inputs using the thermal accommodation formulation. At almost normal incidence, the pressure coefficient is rather sensitive to the value of the accommodation coefficient, varying by almost a factor of 2 over the input accommodation coefficient range of 0 to 1.

Figure 4.4.2-3 shows the variation of the normal pressure coefficient as a function of impingement angle for various incident gas temperatures. The pressure coefficient is not very sensitive to the incident gas temperature even at very low impingement angles, where a factor of 4 increase in temperature only increases the normal pressure coefficient by 10%.

Figure 4.4.2-4 depicts the variation of the normal pressure coefficient as a function of impingement angle for various wall temperatures. Over the range of payload surface temperatures expected in space, the pressure coefficient varies by 2-5%.

Figure 4.4.2-5 shows the variation of the tangential pressure coefficient as a function of impingement angle for various incident gas temperatures (note from Equation 4.4.2-10 that the accommodation coefficient and wall temperature do not affect the value of the tangential pressure coefficient). Only at small impingement angles does the pressure coefficient differ from
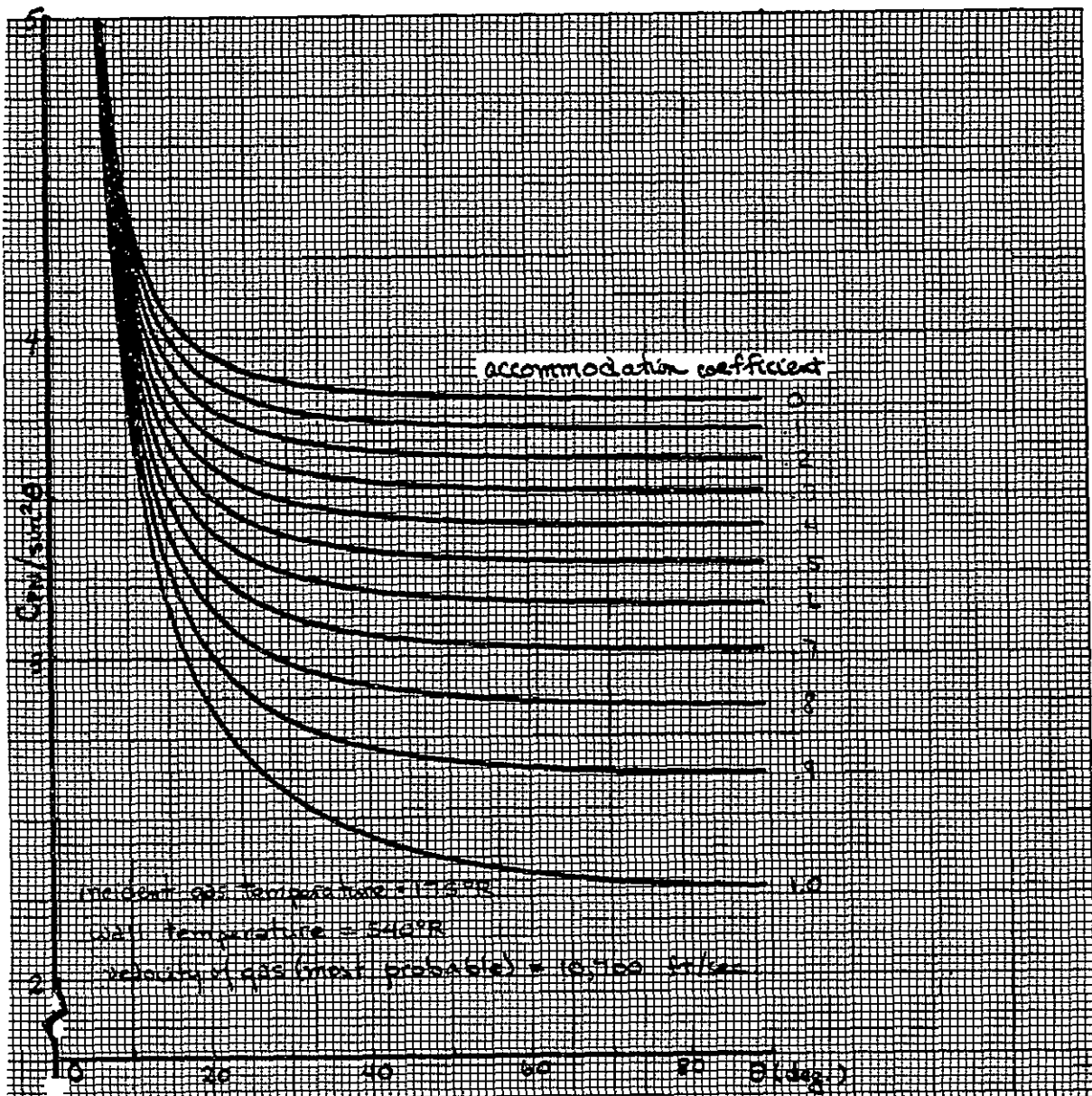
FIGURE 4.4.2-2   VARIATION OF $C_{PN}/SIN^2\theta$ AS A FUNCTION OF θ
FOR VARIOUS ACCOMMODATION COEFFICIENTS
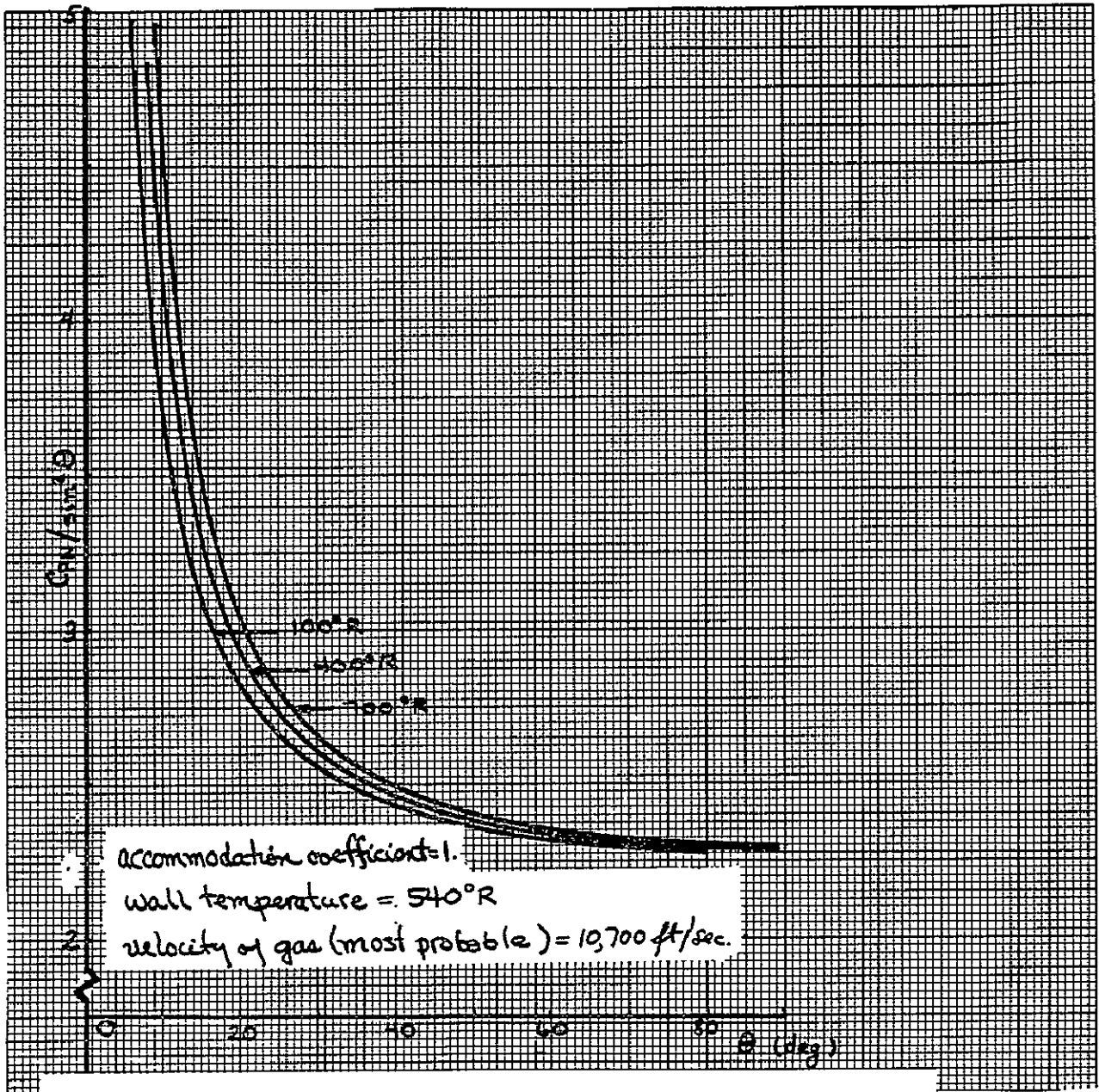
FIGURE 4.4.2-3   VARIATION OF $C_{PN}/SIN^2\theta$ AS A FUNCTION OF θ
FOR VARIOUS INCIDENT GAS TEMPERATURES

130
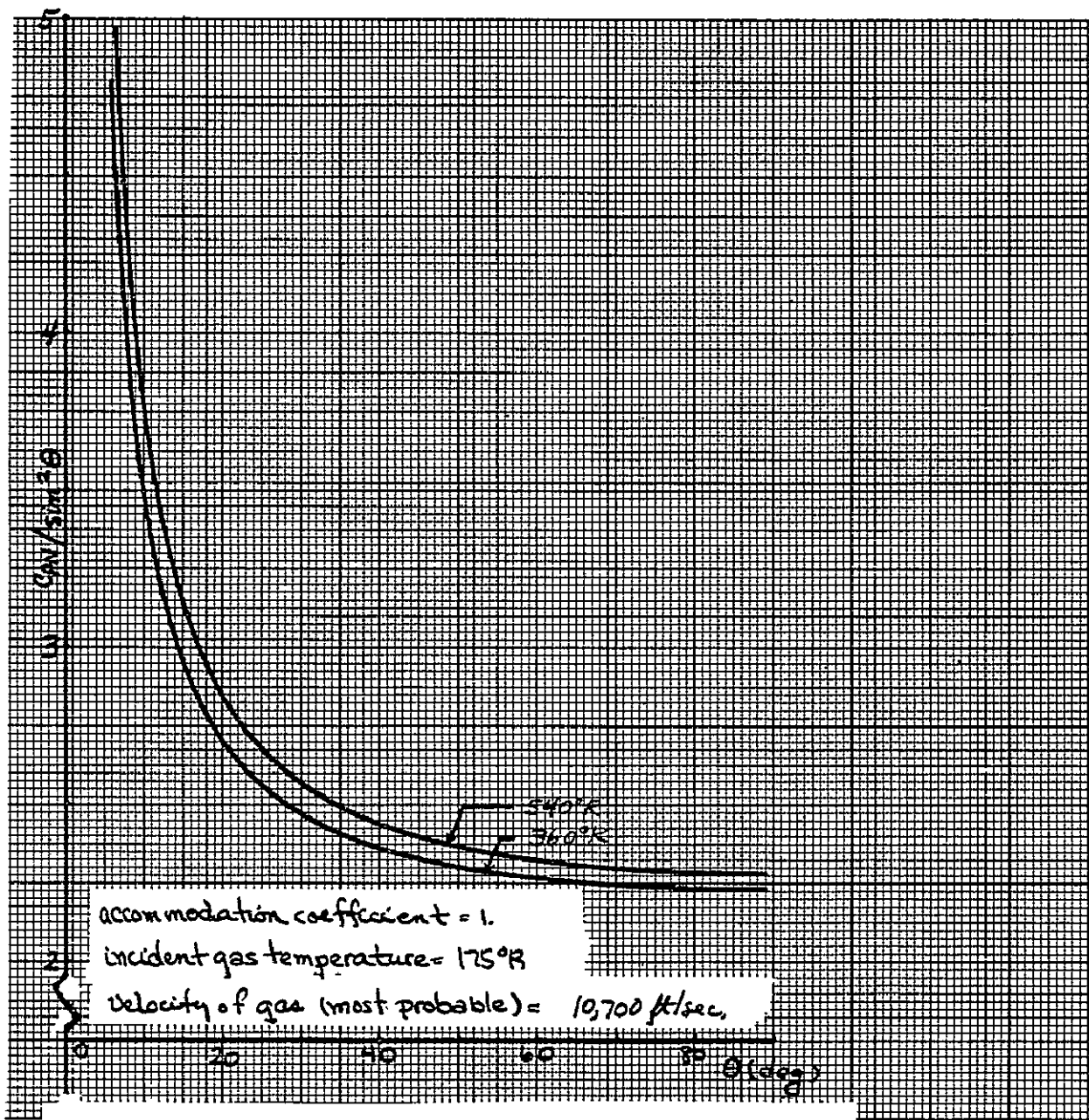
FIGURE 4.4.2-4 VARIATION OF $C_{PN}/SIN^2\theta$ AS A FUNCTION OF θ
FOR VARIOUS WALL TEMPERATURES

131
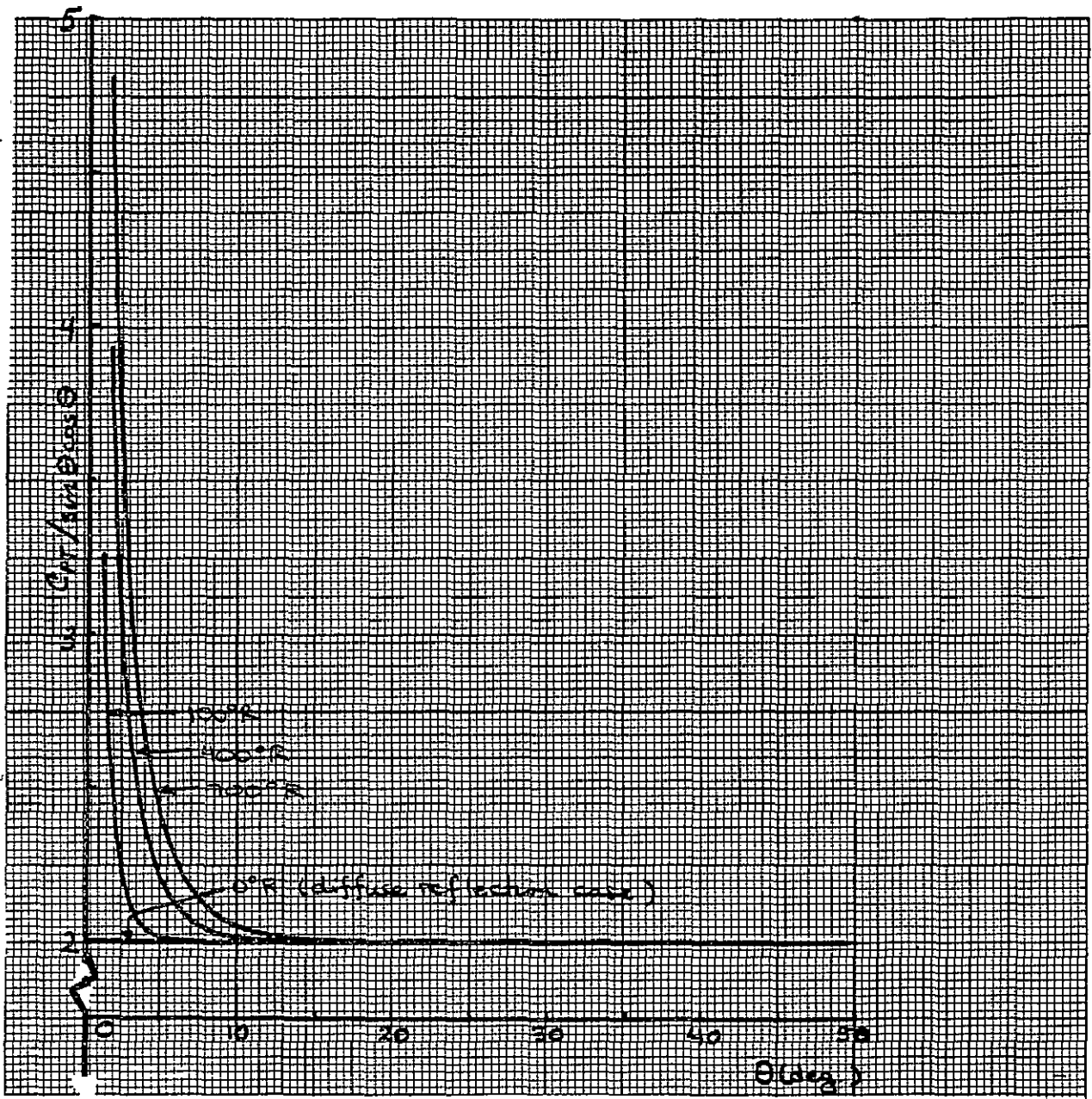
FIGURE 4.4.2-5   VARIATION OF $C_{PT}/SIN^2\theta$ COS θ AS A FUNCTION
OF θ FOR VARIOUS INCIDENT GAS TEMPERATURES

the value of 2.0 predicted by diffuse reflection. (In newtonian flow, the tangential pressure coefficient is always zero.)

A comparison of various impingement recipes considered for free-molecule flow is given in Figure 4.4.2-6. Here, the normal pressure coefficient is plotted as a function of impingement angle using the newtonian impact, diffuse reflection, and thermal accommodation formulations (α = 0, 0.8, 0.9, 1.0). Also plotted, for comparison only, is the recommended impingement formulation in the continuum regime: modified newtonian impact (see Section 4.4.1).

A comparison of storage and execution times among the free-molecule impingement formulations using the HP-9825 showed that the thermal accommodation formulation took an average of 95 msec to execute and about 500 storage registers. The other simpler formulations were executed in about 18 msec using 80 storage registers.

From plume information documented in Reference 24, the value of the molecular speed ratio (S) in Equation 4.4.2-6 is about 11.5. For all impingement angles larger than seven degrees, an error of less than 1% is incurred by using the approximations erf S_v = 1 and $e^{-S_v^2}$ = 0 (Equations 4.4.2-8a, 9a, and 10a). These approximations may speed up execution time by a factor of two.

4.4.2.5 Preliminary Conclusions and Recommendations

There is a large variation in the values of the normal and tangential pressure coefficients in the free molecule regime, depending on which formulation is used; further, none of these formulations agrees very closely with the modified newtonian impact formulation used in the continuum regime. From our present understanding of the physics of the gas/surface interaction, we believe the thermal accommodation formulation to be the most accurate.

Newtonian impact theory has been seen to give at best a 10% underprediction in the normal pressure coefficient, and does not predict any tangential forces. The diffuse reflection formulation overpredicts the normal
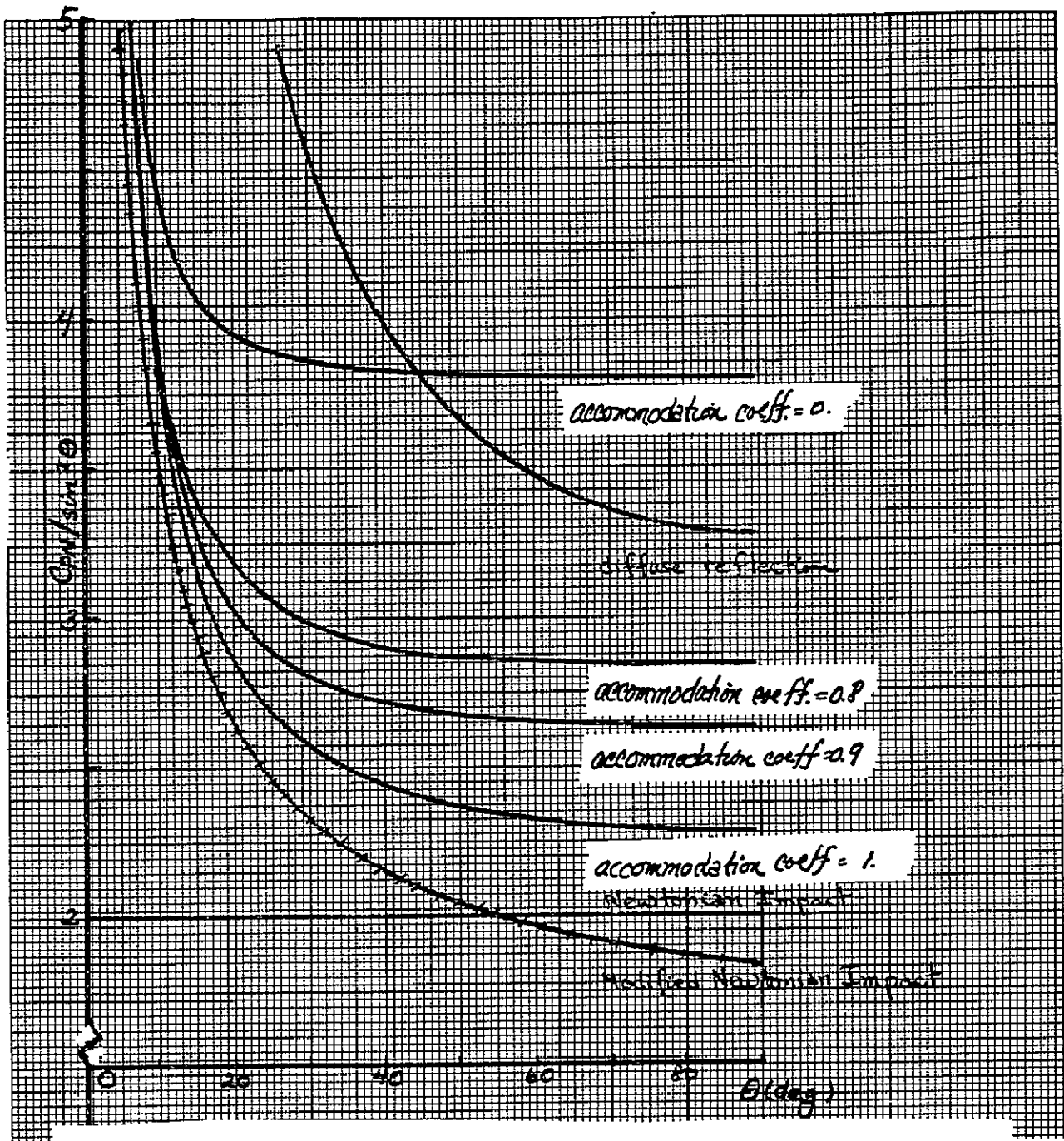
FIGURE 4.4.2-6   COMPARISON OF C_{PN} FOR VARIOUS IMPINGEMENT FORMULATIONS

134

forces by 30%, but accurately predicts tangential forces, except at shallow impingement angles.

The thermal accommodation formulation generates pressure coefficients which are very sensitive to the value used for the accommodation coefficient, with conservative force calculations using smaller values of the accommodation coefficient. These coefficients are fairly insensitive to input values of gas temperature and wall temperature. To within 1% error, the error function can be set to unity and the exponential to zero in these pressure coefficients for impingement angles greater than seven degrees, when considering RCS plumes.

At small impingement angles, tangential pressure coefficients are not small; in fact, at angles as large as 30 degrees, tangential forces are larger than normal forces.

We therefore recommend:
- Use of the thermal accommodation pressure coefficient formulation
- Use of a constant incident gas temperature
- Use of the approximations $\text{erf} \cdot S_v = 1$ and $\exp\left(-S_v^2\right) = 0$ for impingement angles greater than seven degrees.

4.4.3 Impingement Pressure: Transitional-Flow Regime

4.4.3.1 The Question

What impingement pressure formulation is required in the transitional flow regime? This regime is defined in terms of the local knudsen number, Kn: 0.01 < Kn < 10 for transitional flow. In this regime, direct computation of impingement pressure by analysis of flow mechanisms is extremely complex (see Section 4.4). Therefore, the established practice is to use a "weighting function" to transfer from continuum to free molecule impingement formulations. This weighting function, f(Kn), varies from 0 to 1 as the knudsen number varies from .01 to 10. Then the normal and tangential pressure coefficients in the transitional regime are computed as:

$$C_{P_{tf}} = C_{P_{fmf}} \cdot f(k_n) + C_{P_{cf}} \cdot \left(1 - f(k_n)\right)$$

(4.4.3-1)

where "tf" denotes transitional flow

    "fmf" denotes free-molecule flow,

    "cf" denotes continuum flow

Both "hard" and "soft" transitions between flow regimes will be considered in this study.

Hard Transition: The simplest weighting function is a step function. Letting the step transition occur at the "logarithmic midpoint" of the knudsen number interval ,

$$f(k_n) = \begin{cases} 0 & k_n < 0.316 \\ 1 & k_n \geq 0.316 \end{cases}$$

(4.4.3-2)

Soft Transitions: These transitions use weighting functions which are continuous over the knudsen number interval. As a first approximation, let f(Kn) vary linearly with Log Kn. Then, as can be seen in Figure 4.4.3-1,

$$f(k_n) = \frac{2 + \log k_n}{3}$$

(4.4.3-3)

136
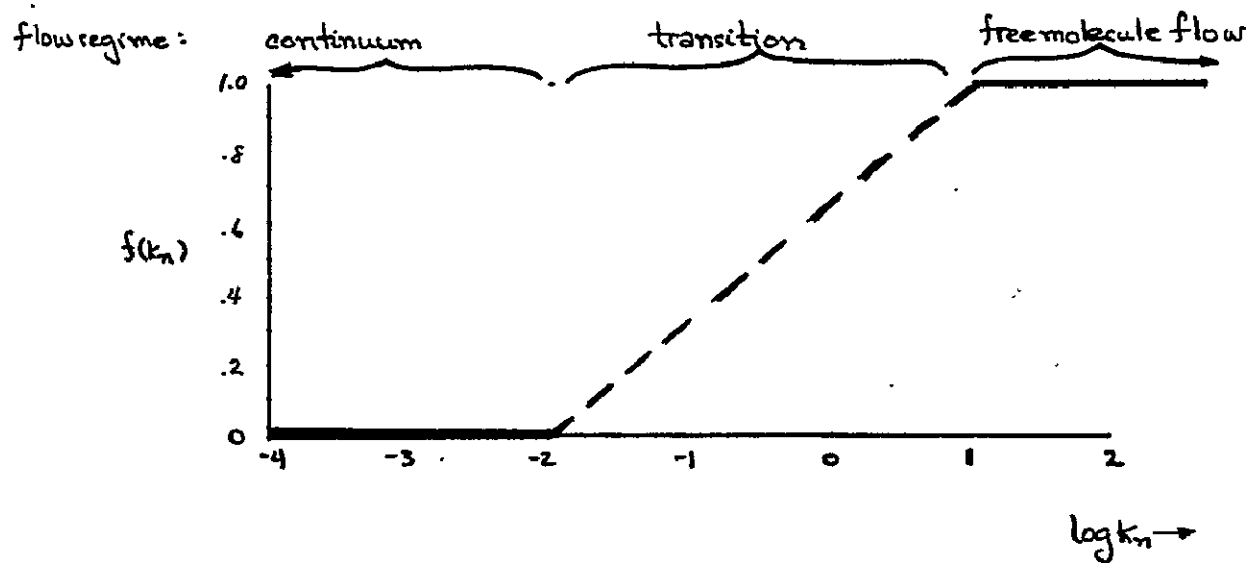
FIGURE 4.4.3-1 A FIRST-APPROXIMATION SOFT-TRANSITION WEIGHTING FUNCTION

The PLIMP program (Section 3.2.4) uses a smooth "s-curve" weighting function, which also has a continuous first derivative. This weighting function varies as the square of a sine function:

$$f(K_n) = \sin^2\left[\frac{\pi}{2}\left(\frac{2+\log k_n}{3}\right)\right]$$

(4.4.3-4)

Finally, in order to reduce execution time, Equation 4.4.3-3 can be replaced by a more accurate linear weighting function based on a simple expansion (slope match) of Equation 4.4.3-4:

$$f(K_n) = \left(\frac{1}{2}+\frac{\pi}{12}\right) + \frac{\pi}{6}\log k_n$$

(4.4.3-5)

In effect, the transition flow limits, $10^{-2} \leq Kn \leq 10$, are changed to the function breakpoints, $.035 \leq Kn \leq 2.85$. The weighting functions listed above are shown in Figure 4.4.3-2.

4.4.3.2 Tradeoff Factors/Considerations

Implementation: Implementation of a transition regime impingement formulation will require the ability to compute both continuum and free-molecule flow pressure coefficients, a routine and appropriate flowfield data to calculate the local mean-free-path, and specification of a characteristic payload subshape dimension to calculate the knudsen number. With these data, any of the previous weighting functions will give pressure coefficients for the transitional regime.

"Cost" Factors: The knudsen number calculation has the largest impact on storage requirements, but a minor impact on execution time, because it is only done once for each subshape, while the impingement pressure is computed for each element (see Section 4.2.2).

The hard transition obviously requires the minimum storage and execution time, since the weighting function computation reduces to a

138

139
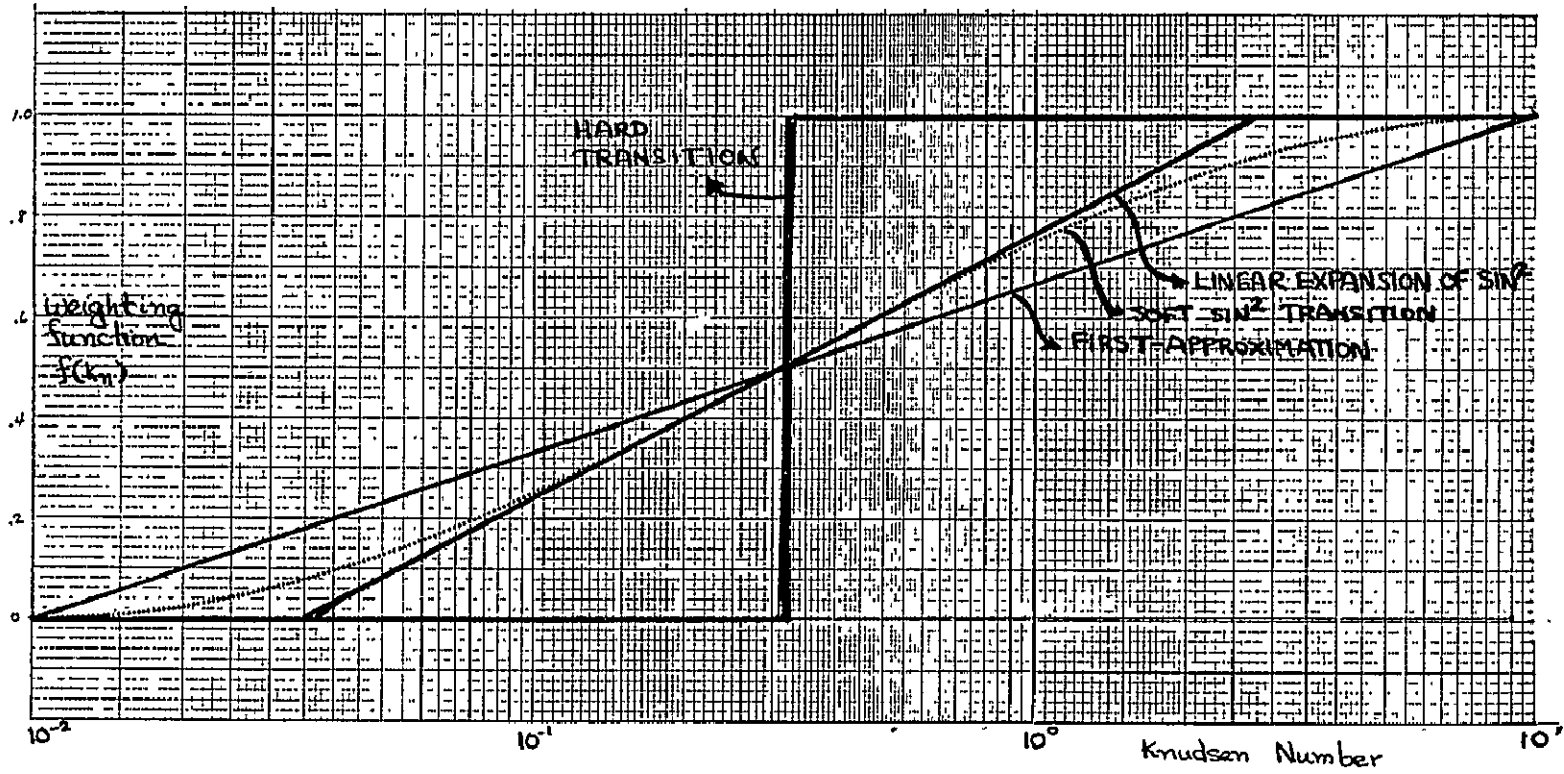
FIGURE 4.4.3-2   WEIGHTING FUNCTIONS CONSIDERED IN THE STUDY

single test, and only one set of pressure coefficients is computed.

The slope-match linear fit of the $\sin^2$ function is the fastest of the soft transitions, since it "shrinks" the region for which dual pressure coefficients need be computed. The $\sin^2$ transition is the only case where the time for computation of the weighting function itself is comparable to the time to compute the two sets of pressure coefficients.

Performance Factors: The soft $\sin^2$ transition is considered the most accurate form, and has a continuous first derivative. The hard transition obviously has the largest error, which occurs in the middle of the transitional region. However, if the continuum and free molecule pressure coefficients are close in value, then the transitional coefficients will be relatively insensitive to the weighting function. The slope-match linear fit is not expected to vary much from the $\sin^2$ form, and may be preferred when execution time is critical.

4.4.3.3 Analysis Approach

The performance of the hard transition and the soft $\sin^2$ weighting function, used with Equation 4.4.3-1, were evaluated by a series of plot runs on a desk calculator. The recommended continuum and free molecule pressure coefficients (modified newtonian and thermal accomodation, respectively; see Sections 4.4.1 and 4.4.2), were used in Equation 4.4.3-1 and transitional pressure coefficients were calculated as a function of the knudsen number for various impingement angles. A value of 0.9 was used for the accommodation coefficient.

4.4.3-4 Analysis Results

Figures 4.4.3-3 through 4.4.3-7 show the transition from continuum pressure coefficients (normal and tangential) to free molecule pressure coefficients using hard and soft ($\sin^2$) weighting functions. Assuming the $\sin^2$ transition to be the most realistic, the maximum error incurred by using the hard transition occurs at $Kn = 0.316$ as expected.
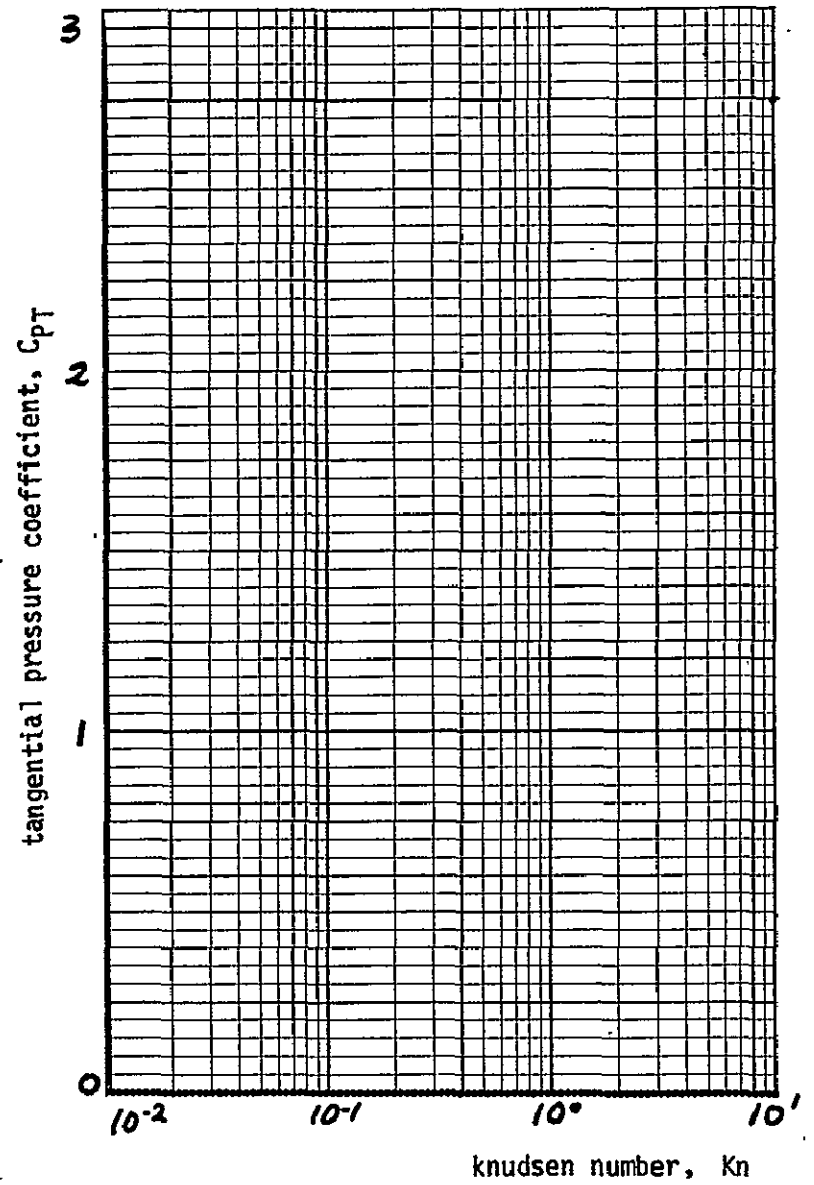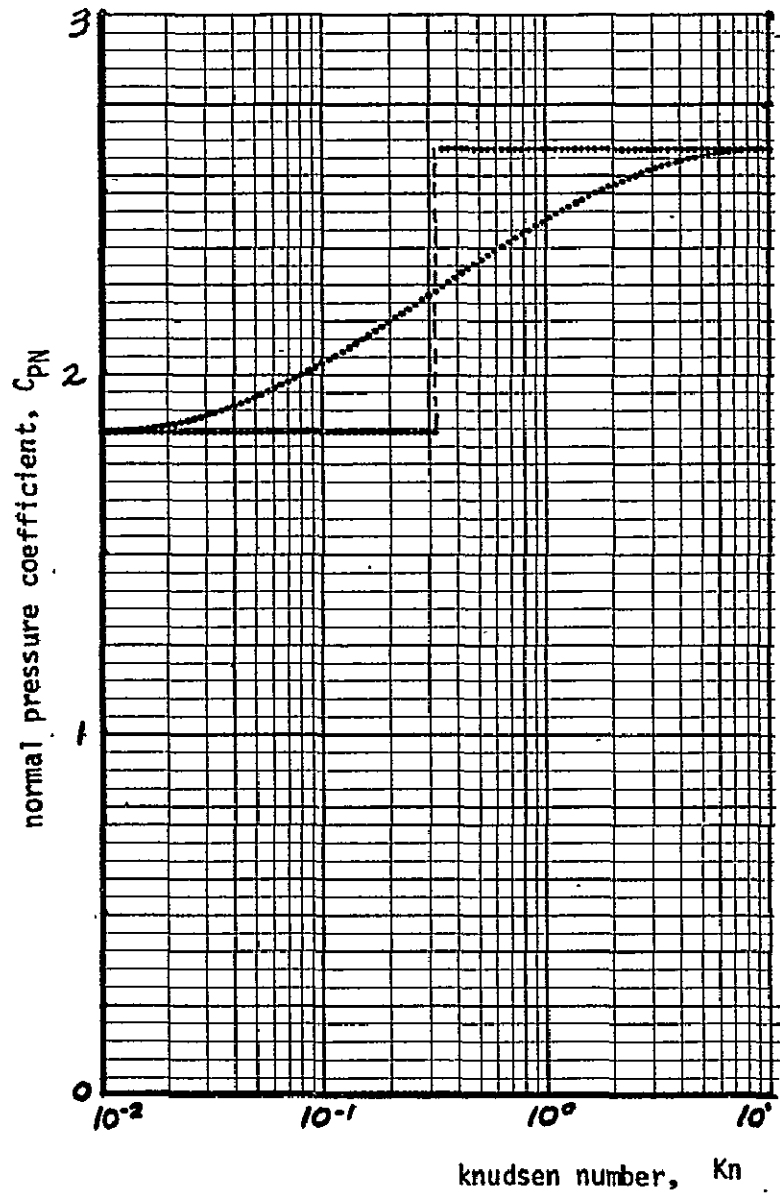
FIGURE 4.4.3-3 HARD VS. SOFT TRANSITION (SIN^2 FORM): $\theta = 90^0$ (NORMAL INCIDENCE)
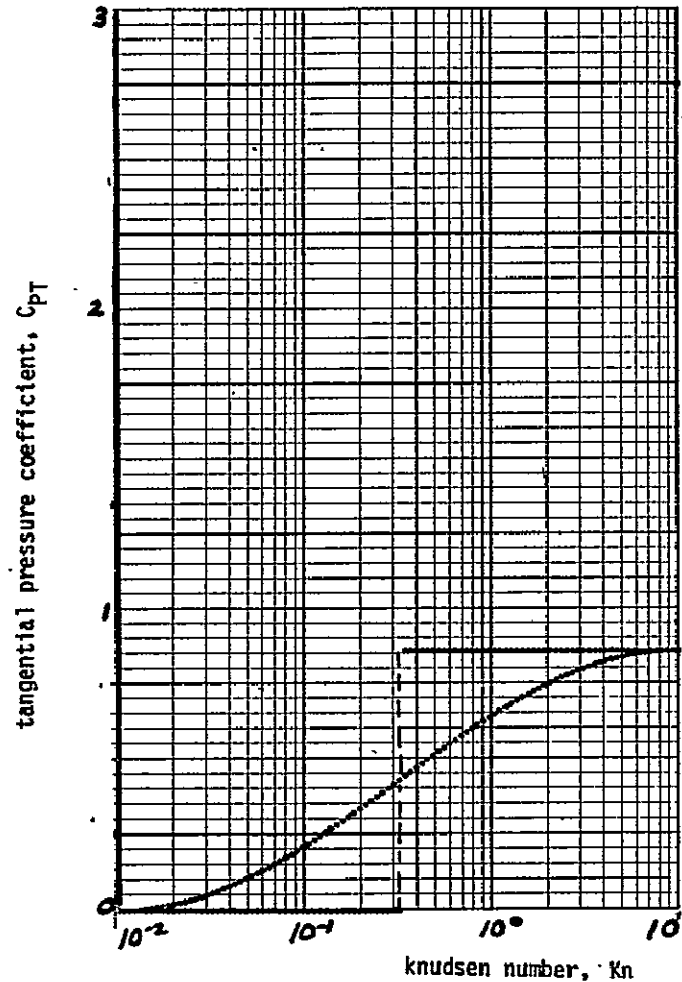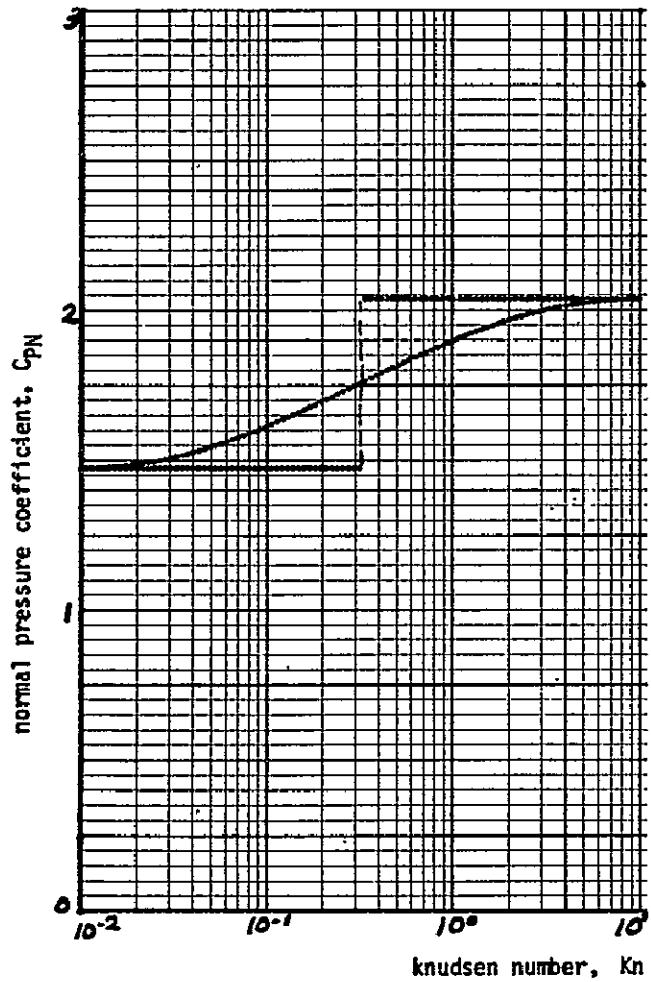
FIGURE 4.4.3-4 HARD VS. SOFT TRANSITION (SIN^2 FORM): $\theta = 60^0$

142
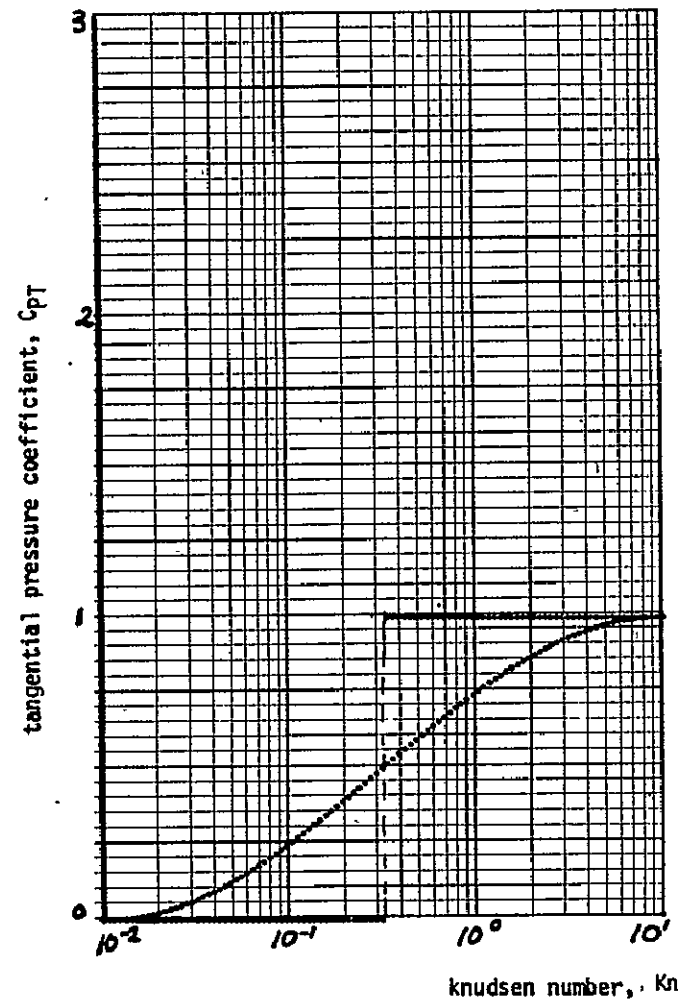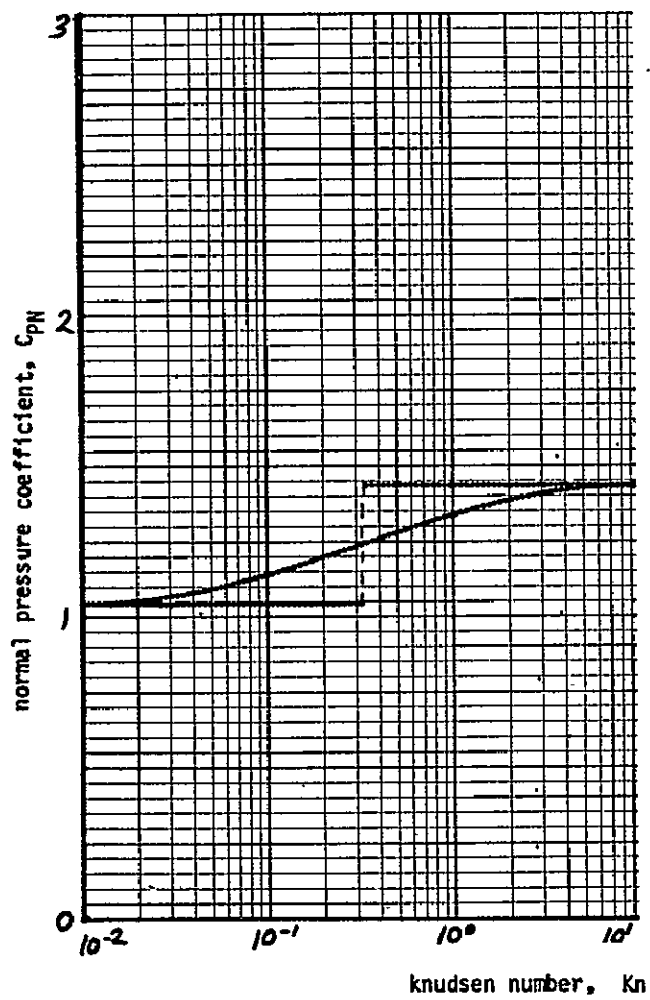
FIGURE 4.4.3-5 HARD VS. SOFT TRANSITION (SIN^2 FORM): $\theta = 45^0$
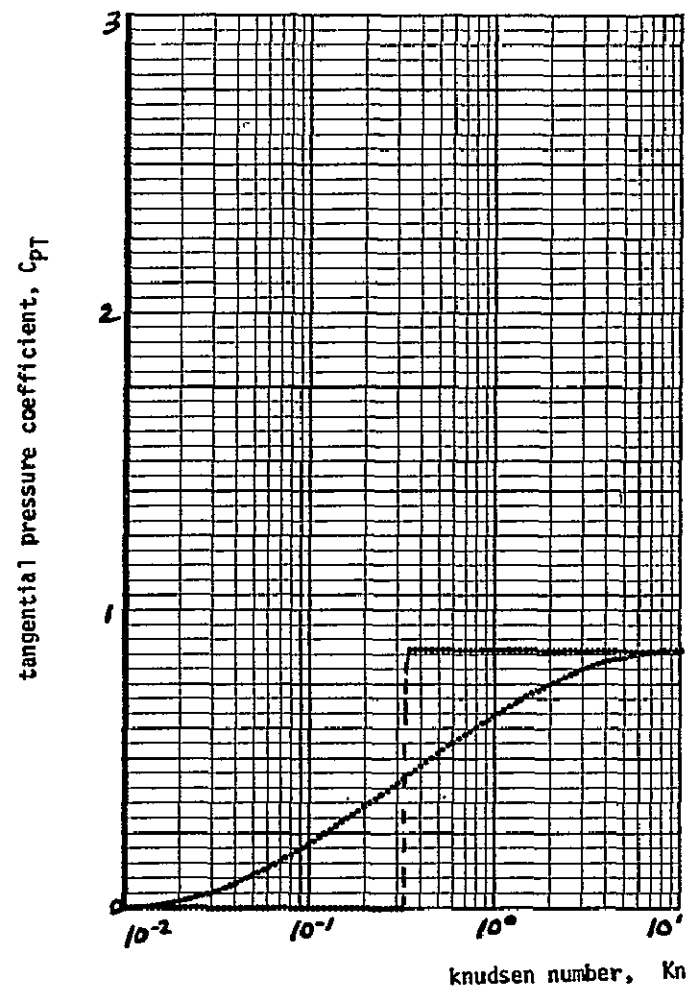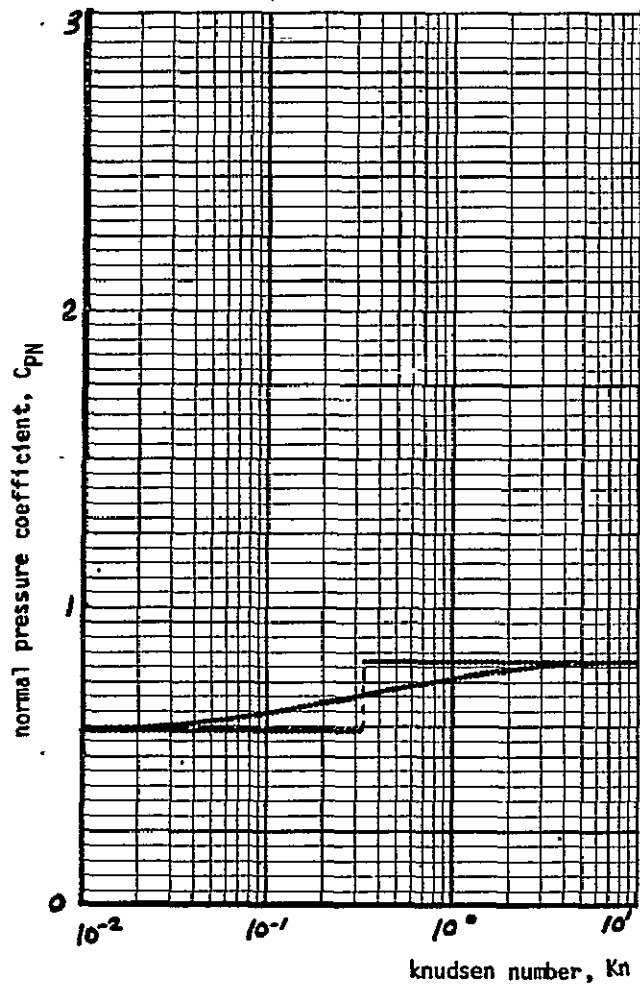
FIGURE 4.4.3-6 HARD VS. SOFT TRANSITION (SIN^2 FORM): $\theta = 30^0$

normal pressure coefficient, C_{PN}

tangential pressure coefficient, C_{PT}

knudsen number, Kn

knudsen number, Kn
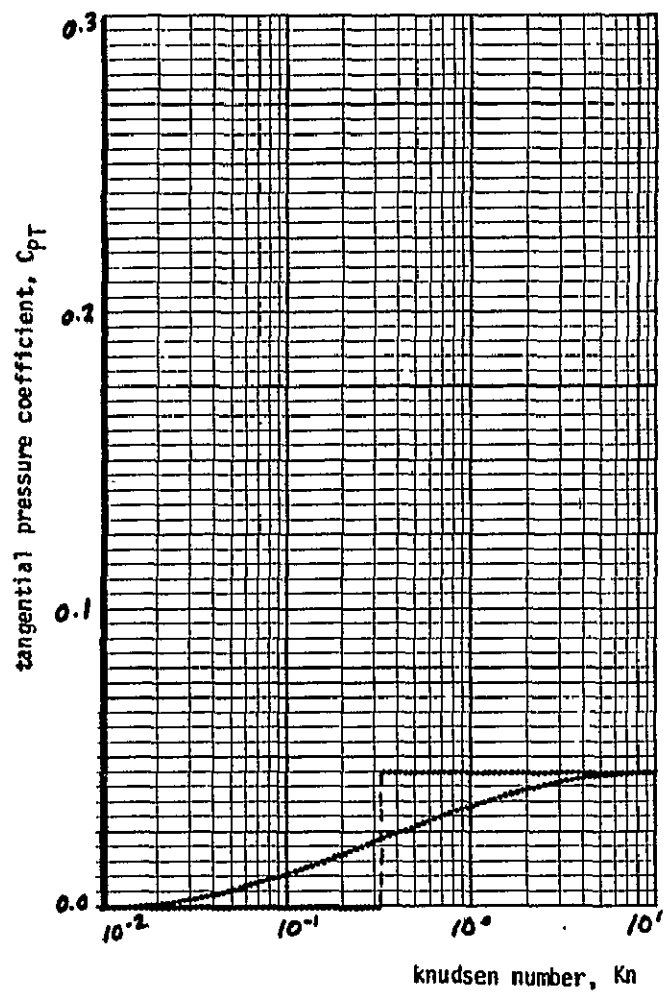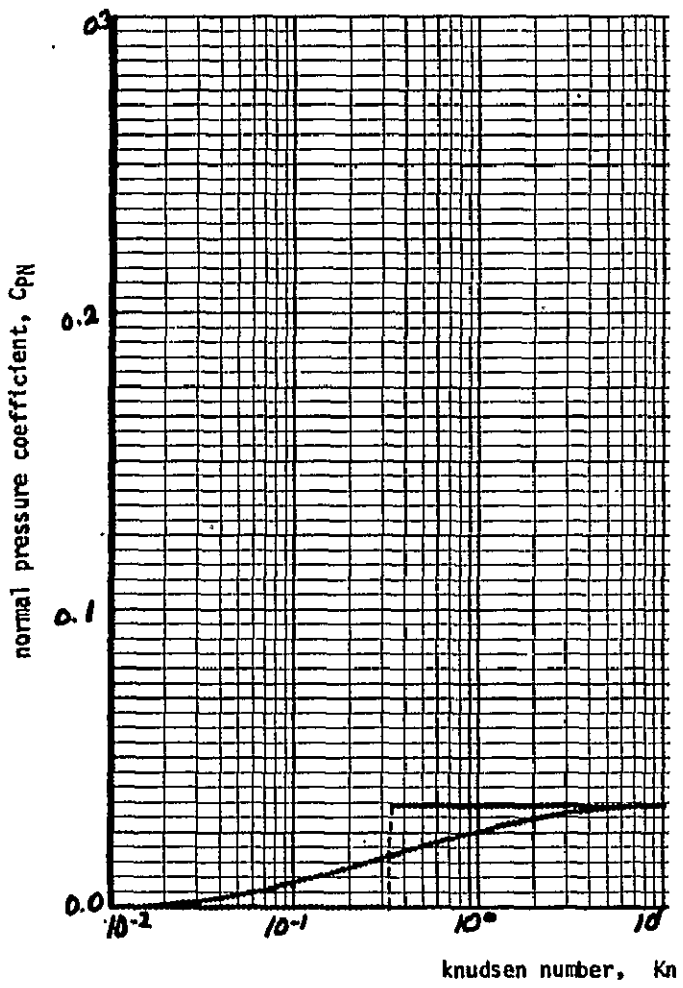
FIGURE 4.4.3-7 HARD VS. SOFT TRANSITION (SIN^2 FORM): $\theta = 0^\circ$ (GRAZING INCIDENCE)

For the normal pressure coefficient, the maximum error is about 15%. The error is fairly insensitive to impingement angle, but does increase somewhat at shallow impingement angles. Since the tangential pressure coefficient in the continuum regime is always zero, the hard-transition value of C_{p_T} is exactly twice the soft-transition value at $Kn = 0.316$, and the maximum error is always 100%.

To consider the linear expansion of the soft sin^2 transition (Eqn 4.4.3-5), the midpoint tangent to the soft transition curves in Figures 4.4.3-3 through 4.4.3-7 can be drawn. The error is largest at the breakpoints, $Kn = .035$ and $Kn = 2.85$, and is typically on the order of 2 or 3 percent.

4.4.3-5 Preliminary Conclusions and Recommendations

Based on the above analysis, the hard transition formulation is not recommended for determining impingement pressure coefficients in the transitional regime. The soft sin^2 formulation is simple and accurate, but the linear expansion of the sin^2 formulation is quicker with comparable accuracy. Therefore, this linear weighting function is recommended.

4.5 Dynamical Effects of Modelling Alternatives

In an on-orbit simulation incorporating a plume impingement model, each thruster firing induces forces and moments on an object (payload or RMS arm) immersed in the plume, thus exciting the dynamics of the object and perturbing its state. In general, these objects are also subjected to non-impingement forces and moments, which also perturb the object state.

The presence of substantial non-impingement disturbances tends to reduce the importance of plume-modelling accuracy for accurate determination of the object state (which is, of course, the ultimate goal of the simulation). The nature of the object dynamics may either "amplify" or "attenuate" state errors due to plume-modelling inaccuracies.

The studies documented in the following subsections were conducted to explore relationships between plume-impingement disturbances, non-impingement disturbances, and object dynamics, to assess the overall importance of plume modelling in computing an accurate object state. Specifically:

- Section 4.5.1 considers plume impingement on the RMS, a situation for which impingement disturbances may be small relative to other disturbances.

- Section 4.5.2 considers propagation of plume disturbances through the dynamics of a free-flying payload, to determine whether plume-modelling errors are amplified by the vehicle dynamics.

4.5.1 RMS Arm: Impingement Moments vs. Inertial-Reaction Moments

4.5.1.1 The Question

Are plume impingement forces and moments on an RMS arm significant in comparison to other forces and moments acting on the RMS? One non-impingement effect acting on the RMS, even when empty, is the "inertial reaction" experienced whenever a thruster firing imparts linear and angular accelerations to the Orbiter.

If a thruster fires while the RMS bears an attached payload, the RMS will experience even greater inertial-reaction effects. In addition, there may be plume impingement on the payload, which will also induce forces and moments on the RMS.

If it becomes obvious that impingement effects are insignificant compared to these other effects, then impingement calculations for the RMS itself need not be incorporated in the new plume model.

As a "by-product" of this sensitivity analysis, we hope to determine whether either impingement or inertial moments (or both) will approach RMS design limits for the maximum moment allowed at the shoulder.

4.5.1.2 Tradeoff Factors/Considerations

Implementation: In order to provide for RMS plume impingement analysis in the plume model, the RMS simulation must provide the position and orientation of each segment of the arm. The plume model must then calculate forces on each segment and moments about each joint. The RMS simulation must then accept these force/moment data for use in dynamical calculations on actuator responses, etc.

Cost: The cost will be large. The plume model itself will require RMS geometry parameters as well as "multiple object" storage and logic, to be able to calculate impingement effects on a payload and an RMS arm simultaneously. An impingement force on a single RMS segment will create moments about all RMS joints. Execution time will increase substantially

148

as impingement is determined for each segment of the RMS. A large increase in execution time is also expected in the RMS dynamics model, which must accept the force/moment data and compute updated RMS positions.

Performance: Incorporation of RCS impingement calculations on the RMS will require greater accuracy in the continuum flowfield regime, and precise modelling of Orbiter surface shadowing. The improvement in overall RMS modelling accuracy is expected to be small, for two reasons:

- With an attached payload, the forces and moments due to inertial reactions and impingement on the payload will be vastly greater than those due to impingement on the RMS itself.

- Even for an empty arm, RMS dynamics, being nonlinear, will be affected perceptibly only when net moments are comparable to the "saturation" limits of RMS mechanical components - actuators, brakes, and clutches.

4.5.1.3 Analysis Approach

Theory: The relationship between "fictitious forces"(e.g., centrifugal and coriolis forces) as seen in a non-inertial reference frame, and forces seen in a fixed inertial frame, is found in many elementary physics books. Using the position vectors in Figure 4.5.1-1, the torque about the RMS shoulder as measured in the non-inertial Orbiter frame, due to thruster forces, is:

$$\vec{\tau}_{RMS} = \vec{R}_F \times \left(\sum_i m_i \vec{Z}_i \right) - \left(\sum_i m_i \vec{Z}_i \right) \times \left(\vec{\omega} \times \vec{r}_o \right) - \vec{\omega} \left(\sum_i m_i \vec{Z}_i^2 \right) + \sum_i m_i \vec{Z}_i \left(\vec{Z}_i \cdot \vec{\omega} \right) \quad (4.5.1\text{-}1)$$

where parameters are as defined in the figure.

Computations: In this analysis, only the forward +Z RCS thruster was considered. Impingement effects on the RMS are expected to be largest for this thruster. Plume impingement moments were estimated by using PLIMP (Section 3.2.4), including Orbiter shadowing, and using a modified newtonian impingement formulation.

149
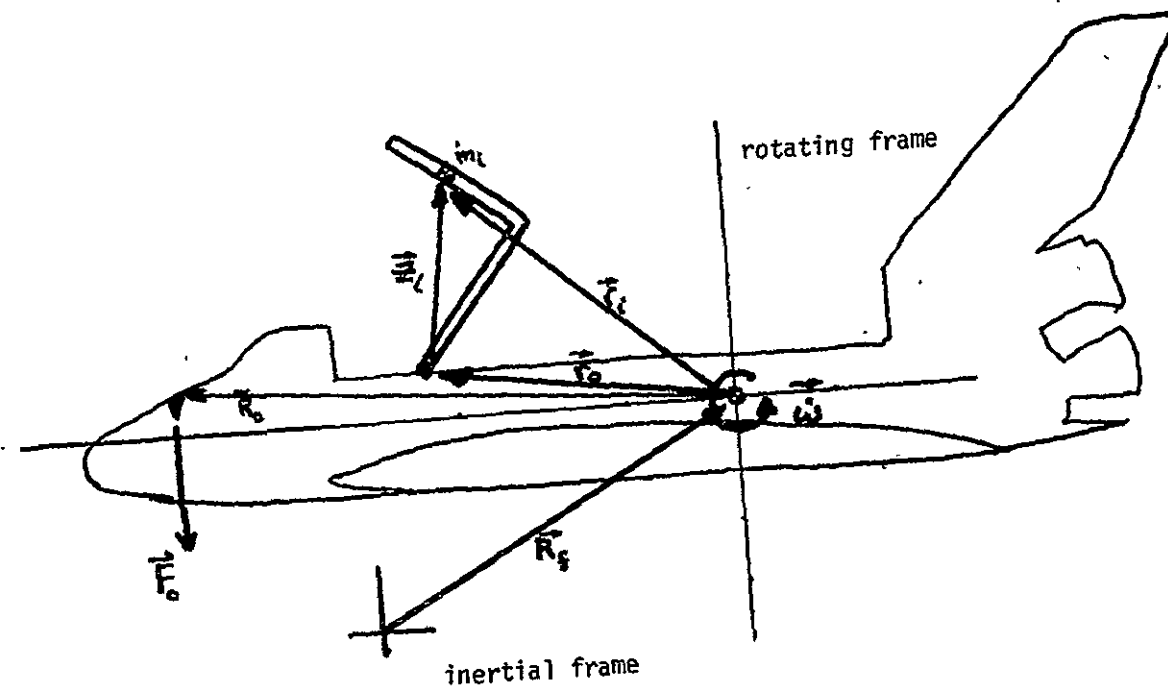
Parameters

    F $\sim$ force

    $\vec{R}$, $\vec{r}$, $\vec{Z}$ $\sim$ position vectors

    m $\sim$ mass

    I $\sim$ moment of inertia

    $\dot{\omega}$ $\sim$ angular acceleration of rotating frame

    τ $\sim$ moment

Subscripts

    o $\sim$ Orbiter

    f $\sim$ Fixed (Inertial)

    i $\sim$ ith element of RMS

$$\ddot{\vec{R}}_f = \frac{\vec{F}_o}{m_o}$$

$$\dot{\vec{\omega}} = \frac{\vec{R}_o \times \vec{F}_o}{I_o}$$

FIGURE 4.5.1-1   VARIABLES INVOLVED IN CALCULATION OF INERTIAL-REACTION MOMENTS ABOUT RMS SHOULDER

Inertial and impingement moments were determined for two basic orientations of the RMS. For the first orientation, the arm was considered to be a straight uniform rod with a mass of about 26 slugs (830 lb.), fifty feet in length, at an angle θ to the longeron, as depicted in Figure 4.5.1-2. This case (with θ = 90°) was chosen since it is expected to have large inertial and impingement forces. As the arm is folded, impingement forces are expected to decrease faster than inertial forces, although a bent arm is operationally more typical. For the second orientation (the "maximum impingement" orientation), the arm is bent forward over the cabin, and passes above the center forward +Z RCS thruster; see Figure 4.5.1-3.

Equation 4.5.1-1 assumes that the initial angular velocity was zero; the Orbiter was considered to be initially inertially stabilized. The RMS was assumed to be rigidly attached to the Orbiter, and only the moment about the shoulder was computed.

4.5.1.4 Analysis Results

The inertial moment for the straight arm case was found to be

$$\vec{\tau}_j = 306\cos\theta + 35\sin\theta + 200 \, lb\text{-}ft \tag{4.5.1-2}$$

For the case depicted in Figure 4.5.1-2, where θ = 90°, the moment is 235 lb-ft, compared to an impingement moment of about 55 lb-ft found with PLIMP. The three dimensional moment results are given in Table 4.5.1-1.

Moments found in the maximum impingement orientation exceed the RMS specification of a guaranteed 772 lb-ft stall torque.
The RMS will slip, and may possibly be damaged. This orientation is not considered typical of normal operations, but shows that impingement forces may place operational constraints on the RMS.

151

AFT VIEW
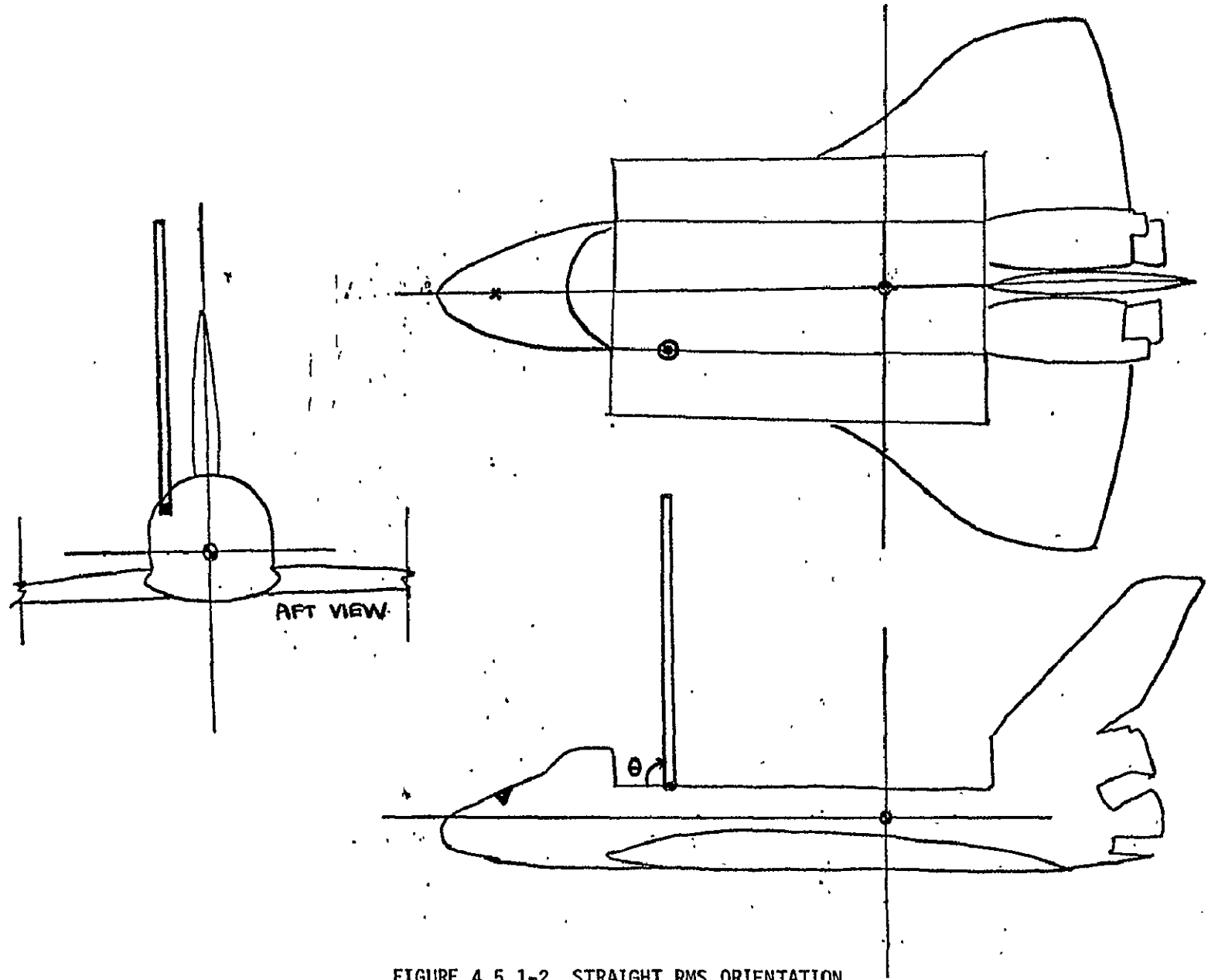
FIGURE 4.5.1-2 STRAIGHT RMS ORIENTATION

AFT VIEW
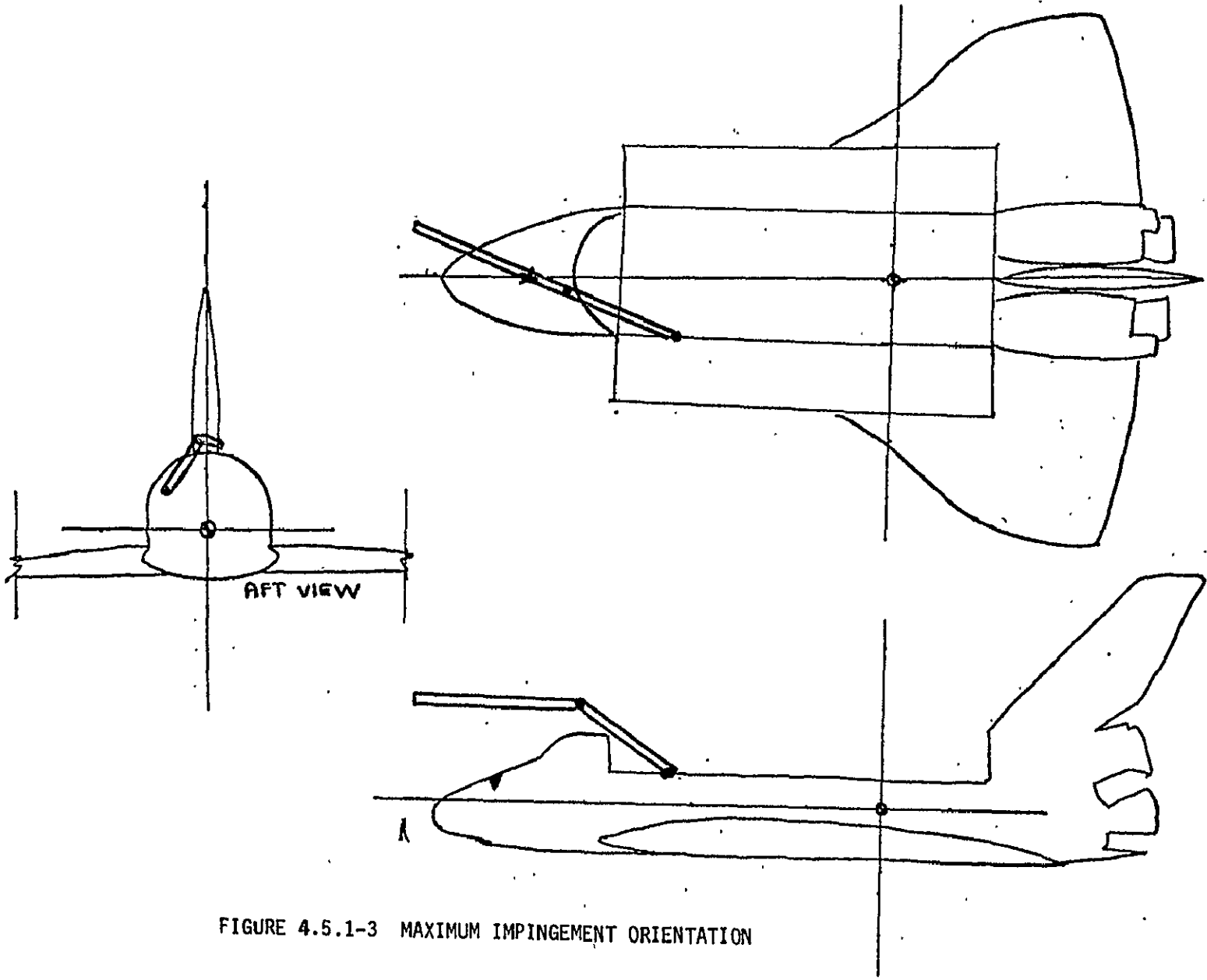
FIGURE 4.5.1-3 MAXIMUM IMPINGEMENT ORIENTATION

TABLE 4.5.1-1 INERTIAL VS. IMPINGEMENT MOMENTS

RMS ORIENTATION		MOMENTS (FT-LB)	
		INERTIAL REACTION	IMPINGEMENT
Straight Arm Perpendicular to Longeron	M_x	0	17
	M_y	235	52
	M_z	0	0
Maximum Impingement	M_x	-81	-635
	M_y	413	1932
	M_z	17	-6

Axis set:

154
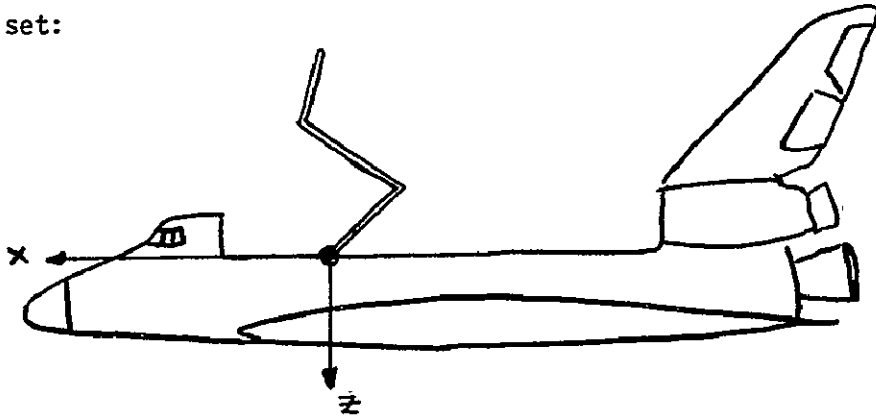
4.5.1.5 Preliminary Conclusions and Recommendations

Based upon the above analysis, we have reached the following conclusions;

● Simulation of plume impingement on the RMS will make little or no
  contribution to the accuracy of RMS dynamical analyses, for normal
  operations.

● Plume impingement considerations can be used to define gross opera-
  tional constraints on the RMS (such as keeping the arm away from the
  vicinity of RCS thrusters).

We therefore make the following recommendations:

● Impingement calculations on the RMS arm should not be incorporated
  in the plume model used in integrated simulations.

● Offline "stand-alone" analysis programs should be used to define
  plume-related constraints on the RMS.

4.5.2 Free Flyers: Propagation Effects

4.5.2.1 The Question

Do propagation effects "amplify" plume modelling errors? Errors in geometric representation, flowfields, pressure coefficients, etc. all contribute to errors in the force and moment computations. These errors in turn cause errors in the angular and linear motion computed in an integrated simulation. Although these errors may initially be small, they tend to grow with time for two reasons:

● Initial errors are propagated through the vehicle dynamics.

● At any later time, forces and moments will be computed using a state which is in error (relative to the true state; see Figure 4.5.2-1), thus "compounding" the error.

There was some concern that under some circumstances, these effects might cause state errors much larger, percentagewise, than the underlying plume modelling error--say, a 20% error in the plume model causing a factor-of-two error in the state perturbations.

4.5.2.2 Tradeoff Factors/Considerations

If we find significant amplification in the errors, the plume modelling errors will have to be kept low to have reliable results in the integrated simulation. This will require higher fidelity and more complex modelling.

Implementation: To reduce plume modelling errors, the flowfield and impingement recipes must be computed from complex equations and logic. Finer mesh sizes and more accurate payload geometry representation must be included in the program.

Cost: The cost will be -high in terms of complexity, storage, and execution time if plume modelling errors are to be held to a very low level.

Performance: By knowing whether propagation effects amplify plume modelling errors, accuracy requirements for the new model can be derived. Long time duration approaches, and approaches allowing intense plume impingement, may require more accurate plume modelling, since the propagation

156
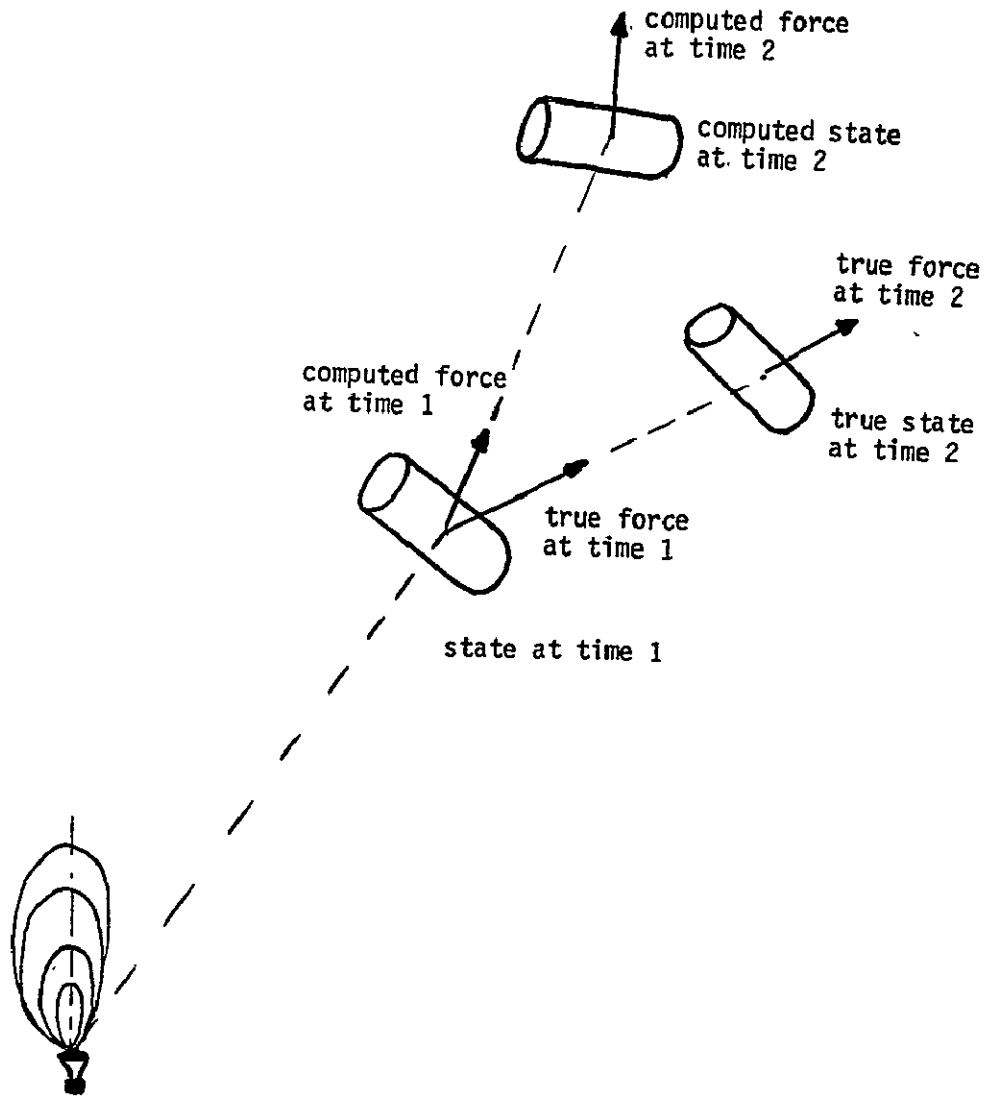
FIGURE 4.5.2-1 PROPAGATION EFFECTS ON PLUME MODELLING ERRORS.

effect will become more visible in these cases.

4.5.2.3 Analysis Approach

Theory: In this sensitivity study, we will only be concerned with plume modelling errors which scale the force on an elemental area by a constant, α. The elemental force $d\vec{F}$ is formed from the elemental area $d\vec{S}$, the dynamic pressure q, and the pressure coefficient c_p:

$$d\vec{F} = C_p \, q \, d\vec{S}$$

(4.5.2-1)

For a plume model where the dynamic pressure or the pressure coefficient has such a constant error, then

$$d\vec{F} = \alpha \, C_p \, q \, d\vec{S}$$

(4.5.2-2)

The force and moment calculations on a payload become scaled by α, causing instantaneous translational and rotational acceleration errors which depend linearly on α. These acceleration errors in turn cause payload state vector errors.

Computation: The Quick Look Disturbance Program, QLDP, (Section 3.2.4) was modified to determine propagation effects due to a constant plume modelling error. Linearized equations of motion (sometimes called the Clohessy-Wiltshire equations) were added for realistic propagation of the payload state. Various approaches to the gravity-gradient stabilized LDEF (Section 3.2.2) were selected from Shuttle Engineering Simulator (SES) data: a nominal braking approach (Reference 25), a V-bar approach using X and Z jets, a V-bar approach using only X jets, and an R-bar approach (Reference 26). For each approach, the payload state was determined using constant scaling factors of 0.50, 0.90, 0.95, 1.00, 1.05, 1.10, and 2.00. The $\pm$ 10% variation ($.90 \leq \alpha \leq 1.10$) is considered typical of the accuracy sought in the new model. Factor-of-two variations are considered typical of simplified models (e.g., see Reference 10).

158

4.5.2.4 Analysis Results

The final payload states (position, pitch, and velocities) at the end of the various approaches are given in Tables 4.5.2-1 through 4.5.2-4 for various scale factors. Also shown in these tables are the ratios of the payload state variables to the payload states in the nominal case (constant $\alpha=1$). These ratios show that in most cases, constant errors in the plume model translate directly into errors in the final payload state with no "amplification" at least for LDEF.

To indicate the significance of such state errors for man-in-loop simulation, Figures 4.5.2-2 through 4.5.2-5 show how the LDEF position and orientation in the local vertical coordinate system would look at the end of each approach. For the approaches using +Z thrusters, the translational displacement is noticeably affected by the scale factor α, although the pitch is not significantly different. Shuttle approaches with the +Z thrusters inhibited show that "a small error in a small perturbation is very small".

4.5.2.5 Preliminary Conclusions

Based on the above analysis, constant errors in the force determination in a plume model translate directly into errors in our knowledge of the final payload state. Propagation effects do not in general amplify plume modelling errors.

TABLE 4.5.2-1 FINAL LDEF STATE VS. SCALE FACTOR
FOR A NOMINAL BRAKING APPROACH

SCALE FACTOR α	STATE PERTURBATIONS						RATIOS OF PERTURBATIONS			
	$\Delta\Theta$ (deg)	ΔX (ft)	ΔZ (ft)	$\Delta\dot{\Theta}$ (deg/sec)	Δv_X (ft/sec)	Δv_Z (ft/sec)	$\dfrac{\Delta\Theta}{\Delta\Theta_{nom.}}$	$\dfrac{\Delta r}{\Delta r_{nom.}}$	$\dfrac{\Delta\dot{\Theta}}{\Delta\dot{\Theta}_{nom.}}$	$\dfrac{\Delta v}{\Delta v_{nom.}}$
0.50	-4.468	-16.23	-6.23	-.0244	-.1408	-.0175	.51	.51	.50	.53
0.90	-7.960	-28.46	-11.29	-.0441	-.2406	-.0353	.90	.90	.90	.95
0.95	-8.388	-29.95	-11.93	-.0465	-.2524	-.0377	.95	.95	.95	.95
1.00 (nominal)	-8.815	-31.43	-12.56	-.0489	-.2642	-.0401	1.00	1.00	1.00	1.00
1.05	-9.239	-32.91	-13.19	-.0513	-.2757	-.0425	1.05	1.05	1.05	1.04
1.10	-9.661	-34.37	-13.83	-.0536	-.2872	-.0450	1.10	1.09	1.10	1.09
2.00	-16.963	-59.72	-25.04	-.0935	-.4745	-.0909	1.92	1.91	1.91	1.81
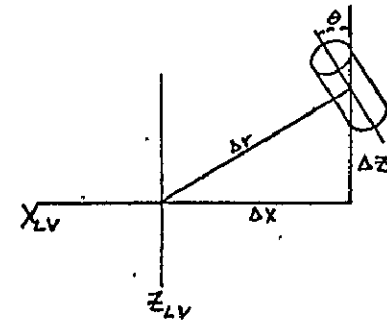
TABLE 4.5.2-2 FINAL LDEF STATE VS. SCALE FACTOR FOR A
V-BAR APPROACH USING +Z THRUSTERS

SCALE FACTOR α	STATE PERTURBATIONS						RATIOS OF PERTURBATIONS			
	$\Delta\Theta$ (deg)	ΔX (ft)	ΔZ (ft)	$\Delta\dot{\Theta}$ (deg/sec)	Δv_X (ft/sec)	Δv_Z (ft/sec)	$\dfrac{\Delta\Theta}{\Delta\Theta_{nom.}}$	$\dfrac{\Delta r}{\Delta r_{nom.}}$	$\dfrac{\Delta\dot{\Theta}}{\Delta\dot{\Theta}_{nom.}}$	$\dfrac{\Delta v}{\Delta v_{nom.}}$
0.50	0.1718	-18.46	18.81	.0060	-.0181	.0616	.82	.52	.77	.52
0.90	0.1916	-31.86	33.37	.0076	-.0275	.1077	.91	.90	.97	.91
0.95	0.1996	-33.46	35.17	.0077	-.0285	.1133	.95	.95	.99	.95
1.00 (nominal)	0.2096	-35.05	36.96	.0078	-.0294	.1189	1.00	1.00	1.00	1.00
1.05	0.2216	-36.63	38.74	.0078	-.0303	.1244	1.06	1.05	1.01	1.05
1.10	0.2360	-38.19	40.52	.0081	-.0312	.1299	1.13	1.10	1.04	1.09
2.00	0.8920	-64.29	71.68	.0101	-.0412	.2242	4.26	1.89	1.29	1.86

SCALE FACTOR α	STATE PERTURBATIONS						RATIOS OF PERTURBATIONS			
	$\Delta\Theta$ (deg)	ΔX (ft)	ΔZ (ft)	$\Delta\dot\Theta$ (deg/sec)	Δv_X (ft/sec)	Δv_Z (ft/sec)	$\dfrac{\Delta\Theta}{\Delta\Theta_{nom.}}$	$\dfrac{\Delta r}{\Delta r_{nom.}}$	$\dfrac{\Delta\dot\Theta}{\Delta\dot\Theta_{nom.}}$	$\dfrac{\Delta v}{\Delta v_{nom.}}$
0.50	0.00816	-.046	.056	-.00003	.00001	.00016	.54	.50	.50	.50
0.90	0.01466	-.084	.101	-.00005	.00002	.00028	.97	.90	.83	.88
0.95	0.01438	-.089	.106	-.00005	.00002	.00030	.95	.85	.83	.94
1.00 (nominal)	0.01513	-.094	.112	-.00006	.00002	.00032	1.00	1.00	1.00	1.00
1.05	0.01588	-.099	.118	-.00006	.00002	.00033	1.05	1.05	1.00	1.05
1.10	0.01663	-.103	.123	-.00006	.00002	.00035	1.10	1.10	1.00	1.11
2.00	0.03014	-.188	.224	-.00011	.00004	.00063	1.99	2.00	1.83	1.97
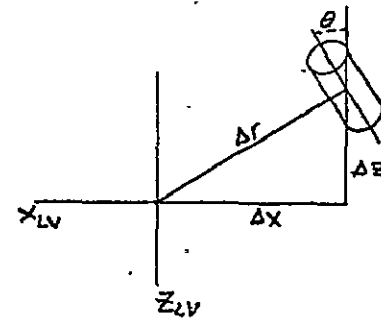
TABLE 4.5.2-4 FINAL LDEF STATE VS. SCALE FACTOR
FOR AN R-BAR APPROACH

SCALE FACTOR α	STATE PERTURBATIONS						RATIOS OF PERTURBATIONS			
	$\Delta\Theta$ (deg)	ΔX (ft)	ΔZ (ft)	$\Delta\dot\Theta$ (deg/sec)	Δv_X (ft/sec)	Δv_Z (ft/sec)	$\dfrac{\Delta\Theta}{\Delta\Theta_{nom.}}$	$\dfrac{\Delta r}{\Delta r_{nom.}}$	$\dfrac{\Delta\dot\Theta}{\Delta\dot\Theta_{nom.}}$	$\dfrac{\Delta v}{\Delta v_{nom.}}$
0.50	.00062	-.050	-.025	$<10^{-5}$	~.00005	-.00001	.50	.50	———	.46
0.90	.00111	-.089	-.046	$<10^{-5}$	-.00010	~.00001	.90	.89	———	.91
0.95	.00117	-.094	-.048	$<10^{-5}$	-.00010	-.00001	.95	.94	———	.91
1.00 (nominal)	.00123	-.100	-.051	$<10^{-5}$	-.00011	-.00001	1.00	1.00	1.00	1.00
1.05	.00129	-.105	-.054	$<10^{-5}$	-.00011	-.00001	1.05	1.05	———	1.00
1.10	.00136	-.110	-.056	$<10^{-5}$	-.00011	-.00002	1.10	1.10	———	1.01
2.00	.00246	-.199	-.102	$<10^{-5}$	-.00021	-.00002	2.00	2.00	———	1.91
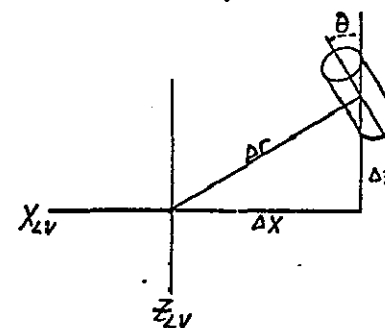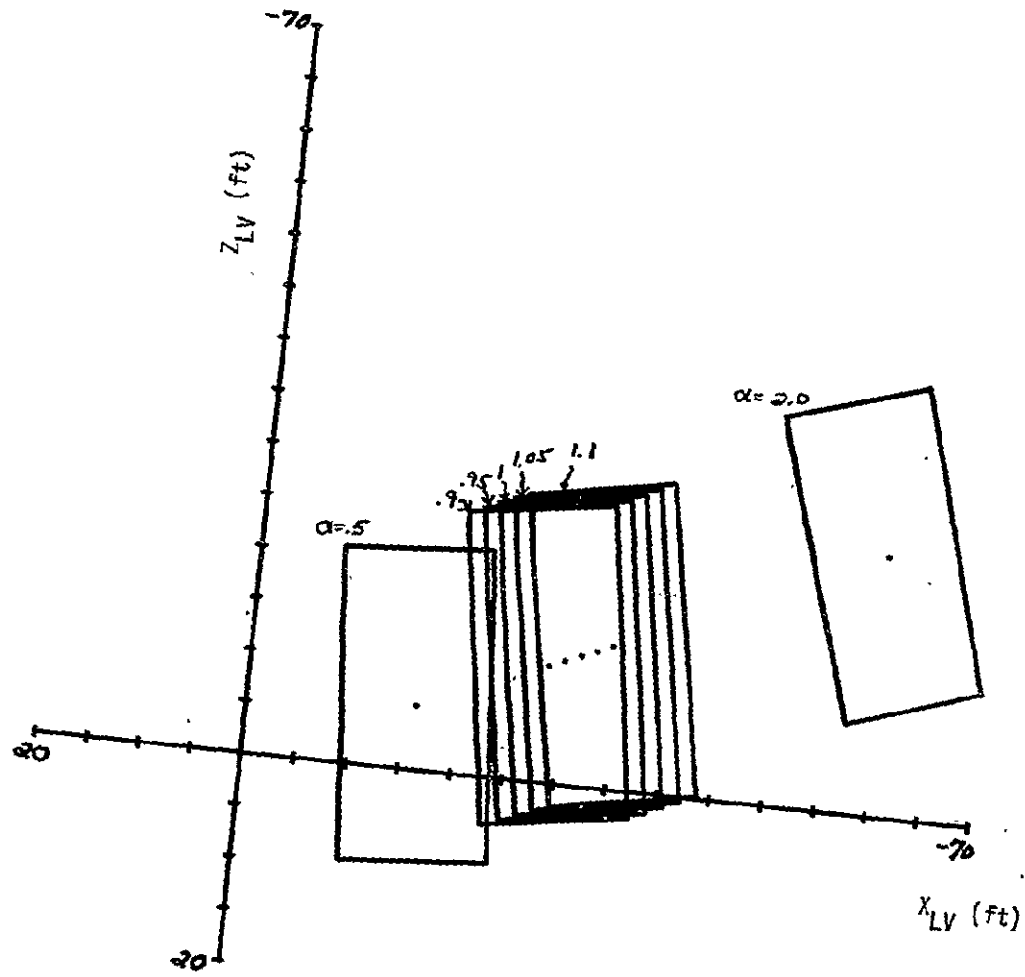
FIGURE 4.5.2-2 FINAL LDEF STATE AS A FUNCTION OF SCALE FACTOR
FOR A NOMINAL BRAKING APPROACH
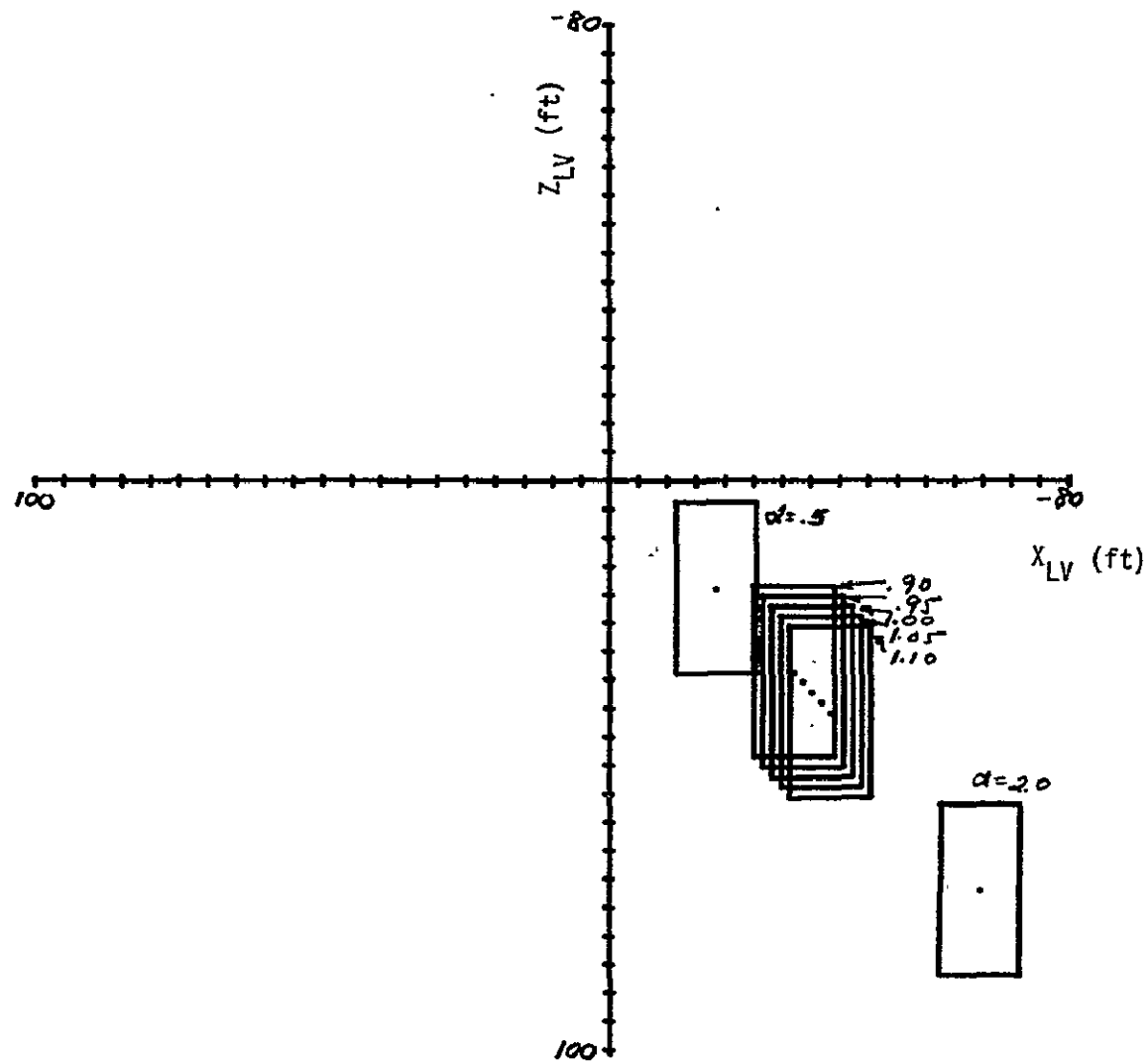
FIGURE 4.5.2-3   FINAL LDEF STATE AS A FUNCTION OF SCALE FACTOR
FOR A V-BAR APPROACH USING +Z THRUSTERS

165
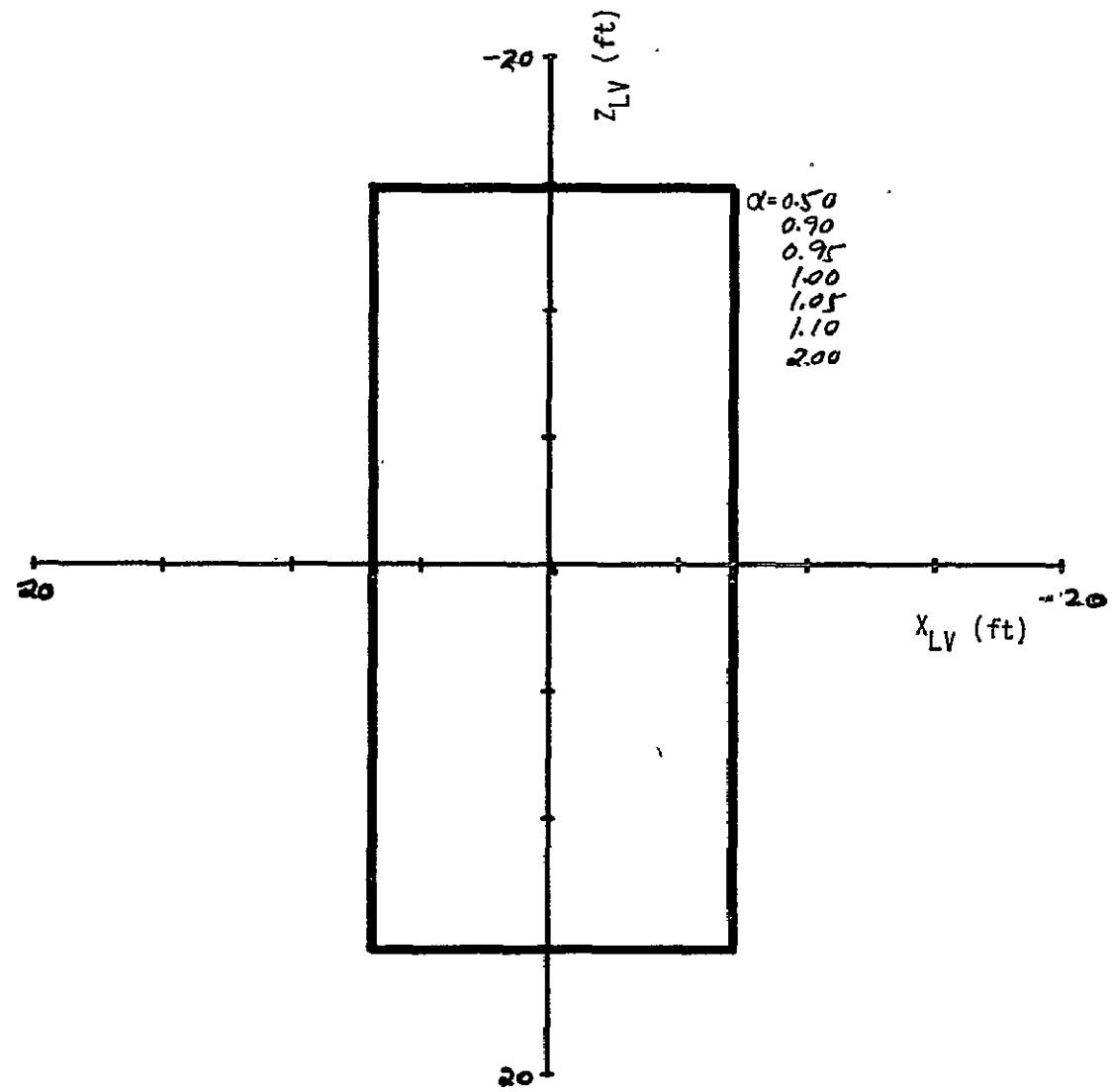
FIGURE 4.5.2-4   FINAL LDEF STATE AS A FUNCTION OF SCALE FACTOR
FOR A V-BAR APPROACH WITH +Z THRUSTERS INHIBITED
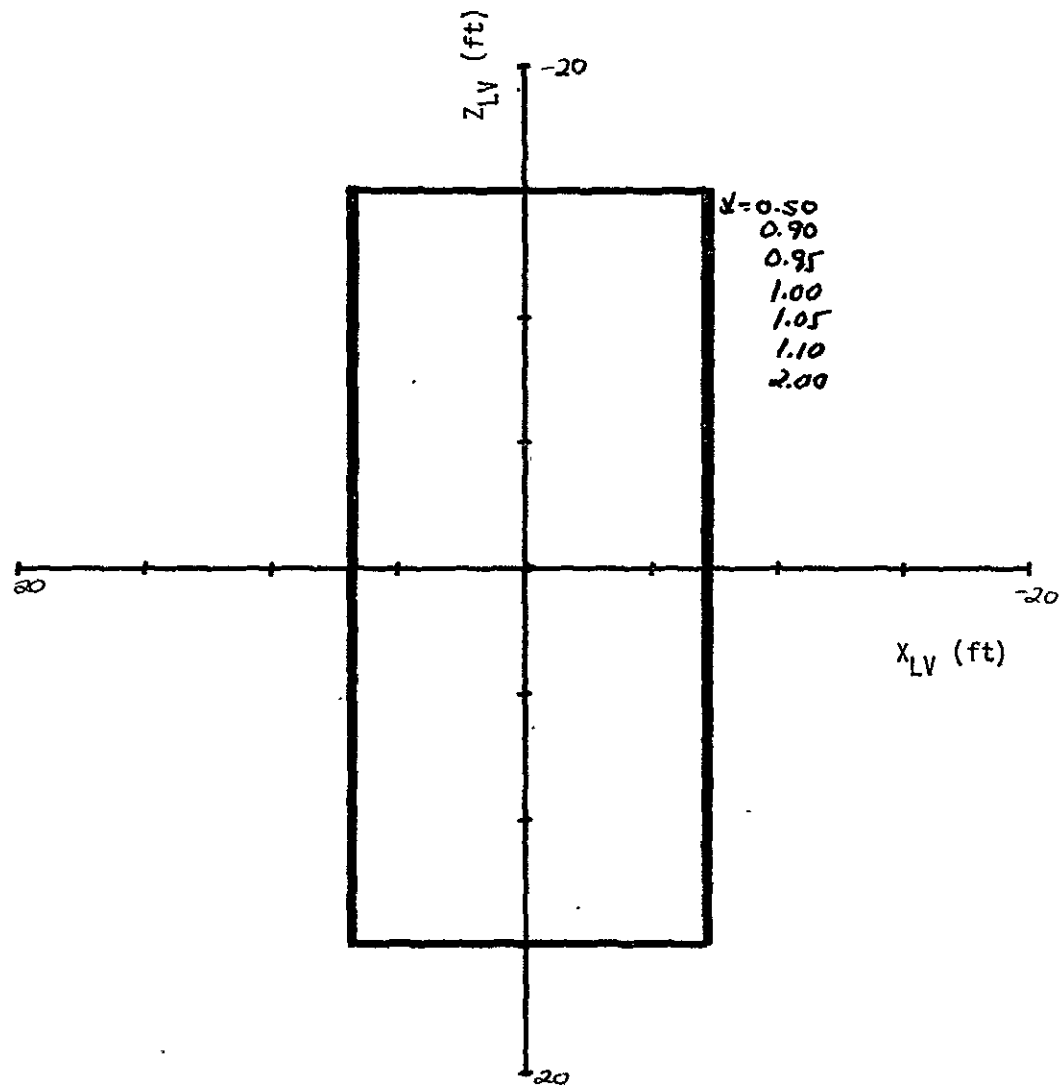
FIGURE 4.5.2-5   FINAL LDEF STATE AS A FUNCTION OF SCALE FACTOR
FOR AN R-BAR APPROACH

4.6 Contaminant Flux Modelling Approaches

(This section to be provided at a later date).

5. CONCLUSIONS AND RECOMMENDATIONS

In this section, the preliminary conclusions from the individual
sensitivity studies are integrated. These preliminary con-
clusions are compared, and potential interactions are considered.
Based on these interactions and intended model uses, a final set
of conclusions and recommendations is determined.

5.1 Integration of Individual Study Results

Results obtained in the individual sensitivity studies of Section 4
were based in part on assumptions concerning the outcome of other
individual studies (e.g., the shadowing studies assumed radial
streamlines). In general, though, "optimum" conditions were estab-
lished for all factors except the factor under study; therefore
few, if any, of the preliminary conclusions were expected to change.

5.1.1 Orbiter/Jet Geometry Studies

Analysis of Orbiter shadowing of RCS plumes (Section 4.1.1) was
done assuming radial flow streamlines and axisymmetric nozzles.
The results indicated that Orbiter shadowing should be included
in the model. Actually, many Orbiter thrusters have some scarfing;
further, the flow streamlines are not precisely radial in the imme-
diate vicinity of the thrusters. However, there is no reason to
believe that either of these effects would change the preliminary
conclusion of this study.

The analysis of Orbiter reflection (Section 4.1.2) was based upon
the flow of an aft +Z engine interacting with the Orbiter tail.
The conclusion of this study was that no reflection away from
Orbiter surfaces toward a payload occurs. Although the details of
flow interaction might be different for other engines and other
Orbiter surfaces, the basic conclusion is expected to hold in all
cases.

5.1.2 Object Geometry Studies

The study of object geometry representation indicated that a drastic simplification of object geometry yields unacceptable accuracy, but a "first-order" simplification (e.g., treating a twelve-sided polygonal prism as a circular cylinder) is desirable. The latter conclusion obviously depends on the element subdivision mesh size used in the analysis. The mesh size analysis (Section 4.2.2) showed that a 10 x 10 mesh gave almost the same results as a 50 x 50. Hence, one would expect a 12 x 12 cylinder (which in fact is analyzed as a twelve-sided polygonal prism) to have essentially the same impingement as a circular cylinder. Therefore, mesh size considerations do not change the preliminary conclusion, but in fact add support.

Assumptions made in the mesh size analysis are justified since various geometries were studied in various regions of the plume using a sophisticated flowfield.

A recommendation was also made to include payload shadowing (Section 4.2.3). This recommendation was based on the results of PLIMP analyses of both LDEF and MMS-SMM, using fine mesh sizes. Again, the preliminary conclusions are not changed.

5.1.3 Flowfield Studies

Conclusions reached in the flowfield analyses are: (1) both scarfed and unscarfed RCS thrusters (Section 4.3.2) can be identically modelled in terms of a patched source flow and radial streamlines (Section 4.3.1); (2) the ambient atmosphere has no apparent effect on the plume (Section 4.3.3); and (3) implementation of a "practical boundary" test will save computer time without meaningful sacrifice of accuracy for operations of interest (Section 4.3.3). These results are independent of any assumptions concerning the payload or Orbiter; consequently the conclusions remain unchanged.

One conditional conclusion was also reached in the flowfield studies:

170

an "equivalent engine" formulation should be implemented, if simultaneous firings of adjacent engines occur frequently in operations· of interest (Section 4.3.4). Additional input from NASA will be required to arrive at a final decision on implementing this feature.

5.1.4 Impingement-Pressure Studies

Analysis of impingement in the continuum regime (Section 4.4.1) suggested that a modified newtonian formulation be used. This conclu-· sion is based upon a PLIMP analysis of LDEF and MMS-SMM payloads at various orientations. Payload shadowing and a fine mesh size (30 x 30) were assumed to be important and were, therefore, included.

The free-molecule impingement analysis (Section 4.4.2) was performed· analytically without assumptions regarding payload, mesh size, etc. Results of other studies cannot, therefore, affect the free-molecule impingement conclusion--to use a thermal-accommodation formulation.

The transitional impingement analysis (Section 4.4.3) was also analytic and based upon impingement results in the continuum and free-molecule regimes. Use of a "soft" linear weighting function matching the midpoint slope of the sin^2 "S-curve"·was recommended.

Since these impingement results are based on valid assumptions, no change is recommended in the preliminary conclusions.

5.1.5 Dynamical Effects Studies

In considering dynamical effects of modelling alternatives, the preliminary conclusions in Section 4.5.1 were that impingement on the RMS arm should not be modelled; rather, an offline "stand-alone" program should be used to define gross operating constraints on the RMS. These conclusions were based on PLIMP analysis of the RMS, modelled as a set of cylindrical segments, impinged upon by an axisymmetric thruster, with Orbiter shadowing included. Inertial reactions of the RMS to RCS firings were analytically determined.

Since all the PLIMP assumptions have been determined to be good, no change to the preliminary conclusions is suggested.

For free-flying payloads (Section 4.5.2), constant "scale factor" errors in the plume pressure model translated directly into errors in knowledge of the payload position and orientation (i.e., no "amplification" effects), in most cases. This result, however, was based upon an analysis where the LDEF payload was modelled as four plates (not a first-order simplification) and the impingement was simple newtonian. Since these have been seen not to be good assumptions, and a scale factor is not the most general form of modelling error, the conclusion of this study must be relaxed. Still, we expect no significant amplification effects from vehicle dynamics.

5.1.6 Contamination Studies

(This section will be supplied at a later date.)

5.2 Summary of Modelling Recommendations

Based on the results obtained in the Plume Impingement Model Sensitivity Analysis Study, the recommendations of Table 5-1 are suggested for implementation in the Level B requirements for the plume model.

TABLE 5-1 SUMMARY OF MODELLING RECOMMENDATIONS

MODELLING AREA	RECOMMENDED IMPLEMENTATIONS
4.1 Orbiter/Jet Geometry	• Include shadowing caused by the Orbiter moldline, cabin, OMS-pod bulkhead, and tail. • Do not consider reflections of the plume.
4.2 Object Geometry	• Include some "first order" simplification in the object modelling. • The mesh size should be variable, and on the order of 10x10 in the near field. • Include back-side shadowing, and shadowing of one payload element by another payload subshape.
4.3 Flowfield	• Model the flowfield as patched source flow with radial streamlines. • Neglect effects on the flowfield due to nozzle scarfing and ambient atmosphere effects. • Include a "practical boundary" test. • If simultaneous firings of adjacent engines occur frequently, implement an "equivalent engine" formulation.[a]
4.4 Impingement	• Calculate impingement pressure in the continuum regime using a modified newtonian formulation. • Calculate impingement pressure in the free-molecule regime using thermal accommodation analysis; use approximations for large impingement angles. • In the transitional regime, use a linear weighting function, based on the $\sin^2$ function, to combine continuum and free-molecule results.
4.5 Dynamical Effects	• Neglect plume impingement on the RMS for integrated simulations. Use off-line "stand-alone" analysis to identify gross RMS operating constraints.
4.6 Contamination	To be supplied.

[a]Additional NASA input required for final decision.

173

6. REFERENCES

1. P. B. Schoonmaker, "Final Level A Requirements for Plume Model," TM 1.4-MAB-123, 25 March 1977.

2. E. K. Huckins et al, "Passive Three-axis Stabilization of the Long Duration Exposure Facility," AAS Paper #75-030, 28 July 1975.

3. R. A. Mattson, Goddard Space Flight Center; private communication.

4. S. Gordon and B. J. McBride, "Computer Program for Calculation of Complex Chemical Equilibrium Compositions, Rocket Performance, Incident and Reflected Shocks, and Chapman-Jouguet Detonations," NASA/Lewis, 1971.

5. S. D. Smith and A. W. Ratliff, "User's Manual, Variable O/F Ratio Method of Characteristics Program for Nozzle and Plume Analysis," Volume I - Final Report, LMSC-HREC D162220-E, Lockheed Missiles & Space Company, Huntsville, Alabama, June 1971.

6. C. J. Wojciechowski and M. M. Penny, "Development of High Altitude Plume Impingement Analysis for Calculating Heating Rates, Forces, and Moments," Volume I - Final Report, LMSC-HREC D162867-I, Lockheed Missiles & Space Company, Huntsville, Alabama, March 1971.

7. D. J. Pearson, "QLDP User's Guide," TM 1.4-MAB-102, January 1977.

8. "Shuttle Operational Data Book (SODB)," JSC-08934, October 1976.

9. D. J. Pearson, "Quick Look Disturbance Study for Skylab Revisit," TM 1.2-MAB-128, April 1977.

10. P. B. Chiu, "A Comparison of QLDP and PLIMP in Disturbance Performance Data Calculations on Skylab," TM 1.4-MAB-133, 22 April 1977.

11. Schaaf, S. A. and P. L. Chambre, "Flow of Rarefied Gases," Princeton Aeronautical Paperbacks No. 8, Princeton University Press, 1961.

12. Loeb, L. B., "The Kinetic Theory of Gases," Third Edition, Dover Publications, Inc., 1961.

13. Richards, J. A. et al, "Modern University Physics," Addison-Wesley Publishing Co., 1960.

14. Dorrance, W. H., "Viscous Hypersonic Flow," McGraw-Hill Book Co., Inc., 1962.

15. Snehla, R. A. and B. J. McBride, "Fortran IV Computer Program for Calculation of Thermodynamic and Transport Properties of Complex Chemical System," NASA TN D-7056, 1973.

16. D. B. Kanipe, "Description of a Computer Program, Written for the HP Model 9830 Calculator, to Calculate Plume Impingement Forces and Moments on Surfaces Immersed in a Rocket Exhaust Plume," JSC-10891, 17 November 1975.

17. G. A. Simons, "Effect of Nozzle Boundary Layers on Rocker Exhaust Plumes," AIAA Journal Vol. II, No. 10, P. 1534.

18. H. L. Jones, "Postsimulation Analysis of the Onorbit-2 and RMS-1 Close-in Stationkeeping Simulation," JSC IN 77-FM21 (JSC-12597), 23 March 1977.

19. R. J. Hoffman, "Free-Space RCS Plume Patterns," TM 1.4-MAB-55, 28 May 1976.

20. "U.S. Standard Atmosphere, 1962," prepared by NASA, USAF, and USWB.

21. H. R. Baum and A. E. Germeles, "Atmospheric Penetration of Exhaust Plumes Under Rarefied Flow Conditions," Quarterly of Appl. Math, January 1976.

22. D. J. Pearson, "Quick Look Disturbance Program Validation: Pressure Coefficients," TM 1.4-MAB-90, 26 November 1976.

23. C. V. Heer, "Statistical Mechanics, Kinetic Theory and Stochastic Processes," Academic Press, 1972, (Chapter 4).

24. R. J. Rader, "Refined Plume Flowfield for Scarfed Engine," TM 1.4-MAB-105 Rev. A, 26 January 1977.

25. D. J. Pearson, "Feasibility of Nominal Braking Approach for Sensitive Payloads," TM 1.4-MAB-79, 7 October 1976.

26. D. J. Pearson, "Plume Impingement on R-bar and V-bar Approaches," TM 1.4-MAB-97, 27 December 1976.

JM2/Center Data Management (3)
JM6/Technical Library (2)
CB/W. Lenoir
CG5/T. Guillory
EX3/B. Roberts
FA/H. Tindall
    R. Rose
    M. Cassetti
FM/R. Berry
    E. Davis
FM2/E. Lineberry
    K. Young
    J. Bell
    R. Becker (2)
FM4/R. McAdams (3)
FM6/E. McHenry
    H. Sullivan
MP/J. Bostick
PA/C. Charlesworth
Hdqtrs/MOE
      L. Edwards
GSFC/A. Rudmann
LaRC/M. Hall
  E. Huckins
MDAC/R. West (5)
    Authors
TRW/S. Wilson
FM14/Report Control Files (25)